E. S. Gevorkyan, V. P. Nerubatskyi, M. V. Kislitsa

COMPOSITE MATERIALS BASED ON ALUMINA AND SILICON CARBIDE

Monograph

MINISTRY OF SCIENCE AND EDUCATION OF UKRAINE

UKRAINIAN STATE UNIVERSITY OF RAILWAY TRANSPORT

E. S. Gevorkyan, V. P. Nerubatskyi, M. V. Kislitsa

COMPOSITE MATERIALS BASED ON ALUMINA AND SILICON CARBIDE

Monograph

Recommended by the Academic Council of Ukrainian State University of Railway Transport

Kharkiv – 2022

UDC 621.763
G27

***Reviewers*:**

Pitak Yaroslav Mykolaiovych, Doctor of Engineering Sciences, Professor, Head of the Department of Ceramic, Firebrick, Glass and Enamel Technologies of National Technical University "Kharkiv Polytechnic Institute";

Logvinkov Serhii Mykhailovych, Doctor of Engineering Science, Professor, Head of the Department of Technology and Life Safety of the Semyon Kuznets Kharkiv National University of Economics.

Recommended by the Academic Council of Ukrainian State University of Railway Transport for publishing as monograph of March 24, 2022, report no. 2

G27 Gevorkyan E. S., Nerubatskyi V. P., Kislitsa M. V. Composite materials based on alumina and silicon carbide: Monograph. – Kharkiv: LLC "Voskhod-Print", 2022. – 92 p.
ISBN 978-617-8195-14-4

The monograph deals with the modern state and prospects for application of new composite materials based on alumina and silicon carbide, the special features of fabricating alumina and silicon carbide composites with vacuum hot pressing by applying high current to the graphite matrix. It is also concerned with microstructure, physical and mechanical properties, optimal compositions, and research into cutting properties of the composite materials with different primary compositions. The monograph describes the optimal modes of hot pressing for fabricating composites with good physical and mechanical properties, and also the optimal cutting modes for processing highly rigid alloys.

55 figures, 13 tables, 146 references

UDC 621.763

ISBN 978-617-8195-14-4

CONTENTS

ABBREVIATIONS AND NOMENCLATURE

FAST – Field Activated Sintering Technique
HP – Hot Pressing
PAS – Plasma Activated Sintering
PECS – Pulse Electric Current Sintering
SCF – Supercritical Fluid
SPS – Spark Plasma Sintering
TEC – Thermal Expansion Coefficient

INTRODUCTION

Continuous technological development requires new materials with better physical, mechanical and tribological properties, and ceramic materials can substantially meet these requirements. Ceramics are widely used in different industries, such as electronics, metalworking and structural part production. Nevertheless, due to an effective combination of mechanical properties (such as hardness, thermal expansion coefficient, etc.), their application as instrumental materials is the most effective approach. Alumina powders in micro- and nano-scale state are characterized by relatively low cost, which advantageously distinguishes them from other similar materials, particularly, zirconium oxide.

The analysis of literature has demonstrated that it is possible and important to develop oxide-carbide composite materials with better mechanical properties by regulating their microstructure.

And application of nano-scale powder materials is rather promising. As known nano materials considerably differ, in terms of their properties and behavior, from coarse particles of the same material, and some research has been conducted into application of these materials for production of ceramic composites and development of a system to predict the properties of nanocomposites.

A high activity of nono-scale powders can be explained by their developed surface and, consequently, an excess surface energy, which requires intensified production modes. A higher consolidation speed can be achieved by means of intensive consolidation methods, e.g., electro-consolidation (electro-agglomeration), i.e., agglomeration in the electrical field. It would decrease compaction time, increase homogeneity, and, consequently, lead to fabricating a high-density composite with fine-grained structure. The right combination of micropowder and nanopowder components can considerably improve the mechanical properties, particularly, crack resistance.

Nowadays, there exists a wide nomenclature of refractory allows, and the right selection of instrumental materials for their treatment is very important, as it can improve the surface quality and slow down the tool wear. It should also be noted that a lot of material production technologies are rather costly and simplification of their production is very urgent.

Development of materials for cutting plates used in mechanized processing includes, apart from studying the mechanical properties (strength, crack resistance), studying the thermal physical properties (thermal and temperature conductivity) due to the complex thermal conditions under which the tools are used. Heat removal from the

cutting zone is an urgent problem, especially for dry cutting at high speeds. Therefore, higher thermal conductivity of the cutting material is of primary importance.

The monograph presents the results of research into the thermal and temperature conductivity of the composite materials obtained. A potential rise of the wear resistance during cutting can be explained, particularly, by the effect of thermal conductivity of a cutting material. A further development of new competitive materials requires a complex solution of many problems regarding optimization of a raw material composition, improvement of technologies used for production of composite materials, and use of modern technologies for compaction of ultra-disperse powders.

The monograph is part of the scientific project “The Use of Non-traditional Methods of Obtaining Nanopowders and Sintering in the Development of Modified Mullite-ZrO_2 Ceramics Resistant to Heat Shock” (State Registration No. 0121U109441). The monograph was prepared at the Department of Wagon Engineering and Product Quality of Ukrainian State University of Railway Transport (Kharkiv). The project is being implemented according to the competition held by the Ministry of Education and Science of Ukraine for projects on fundamental and applied scientific investigations, scientific and technical developments presented by higher educational establishments and academic institutions belonging to the Ministry of Education and Science of Ukraine as the budget program “Scientific and Research-and-Engineering Activity of Higher Educational Establishments and Academic Institutions”.

CHAPTER 1

FABRICATION OF INSTRUMENTAL COMPOSITE MATERIALS BY THE USE OF NANOPOWDERS

1.1. Materials in the nano- and micro-disperse states

1.1.1. Special features of the structure and properties of a nanomaterial

Nanomaterials can be divided into two groups: compact (nanostructural) and nanodisperse [1]. The first group includes periodically repetitive elements that contact with each other (their sizes < 100 nm) [2]; the second group includes elements in the dispersive medium (gas, fluid, etc.) that are separated from each other. If the distance between them reaches tens of nanometers, it is a nanopowder in which particles are divided with light atoms preventing agglomeration. The powders, that contain nano-objects, aggregates or agglomerates of nano-objects or their mixtures, are also considered as nanopowders [3–5]. It should also be noted that all the particles must be of this size, because a small proportion of nanoparticles is evidently included in any submicron (< 1 mkm) powder, however this is not the reason to consider them as nanopowders. Even though nanopowders could include conglomerates and agglomerates that behave as bigger particles, they are still nano, because, in fact, they consist of nanoparticles and can fall apart under a physical impact.

The earlier studies on nano-crystal materials published in 1980s by Herbert Gleiter and his colleagues showed that grain boundaries of these materials can have some features, regarding their atomic structure, that differ them from grain boundaries in conventional polycrystalline materials [6]. And further research has confirmed the fact, that a grain size is not the single main parameter. The characteristic grain boundaries have been found in ultra-fine grain materials obtained with severe plastic deformation methods [7].

A lot of properties of ultra-fine materials depend upon the properties of fine particles they are composed of. Changes in the properties of such materials begin when some particles decrease up to a size of about 100 nm. When the particles reach a certain critical size L_{cr} their energy rises (fig. 1.1). It is explained by a misbalance of the links between the atoms in a particle and those in the near-surface zone, an area limited by several atomic layers. The volume part of these atoms increases while the particle size decreases. At a size of ~ 5 nm it becomes equal to the volume part of the inner atoms, and the contribution of the surface considerably grows, as it becomes more active. When particles decrease up to 2 nm, the volume part of the surface can

be 5…10 time more than the internal part, i.e. 80…90 % out of the total volume [8]. At this size particles have an excess energy and higher chemical activity; they can aggregate at very low activation energies [9].

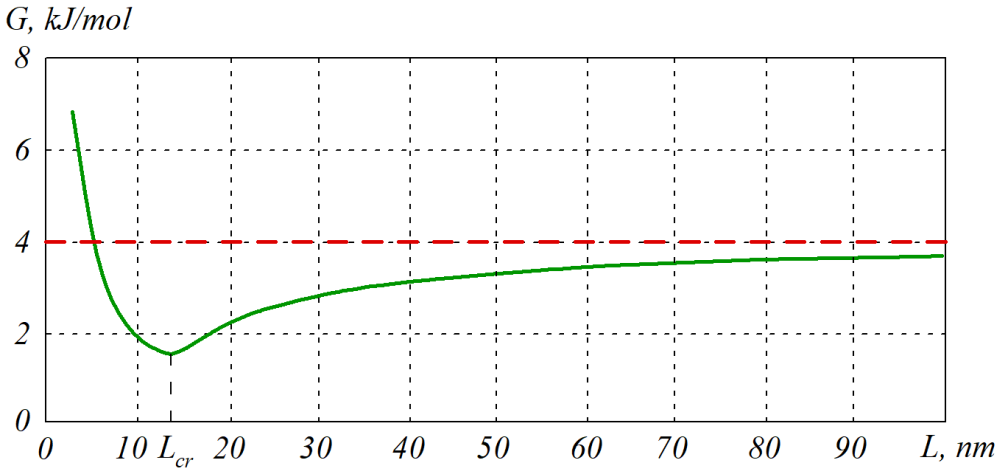

Figure 1.1 – Change in the Gibbs free energy of a binary nano-structural alloy according to the crystallite size (for a standard crystal G = 4 kJ/mol [14])

The size of a particle can affect the properties of the material at a certain value that is comparable with the critical length for various processes, such as the free run length of an electron during electric resistance [6].

One of the size-dependent properties is the melting temperature; for gold, e.g., it decreases by 1000 K when the particle size reaches 2 nm (fig. 1.2). It is typical for metals and binary compounds [10].

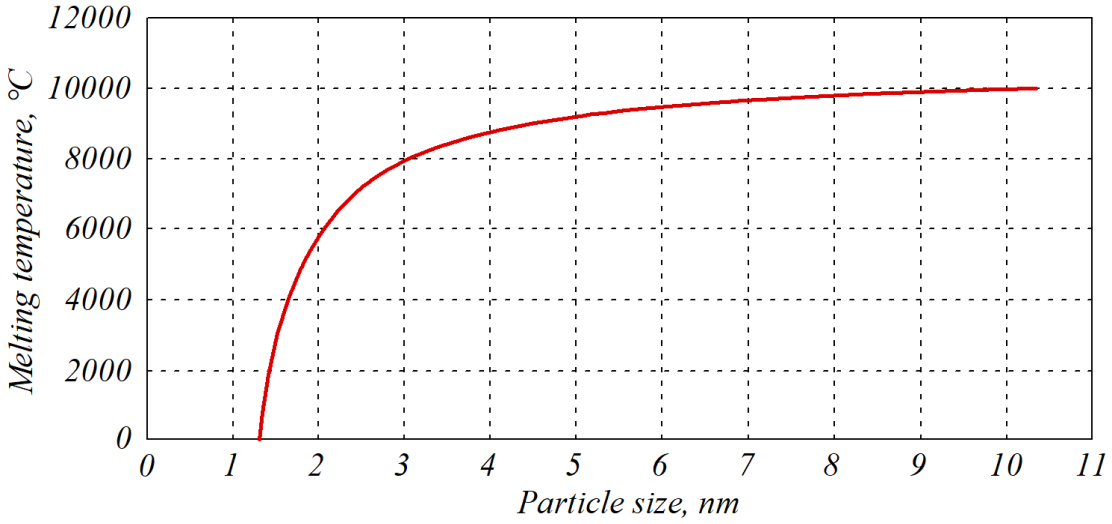

Figure 1.2 – Dependency between the particle size for gold and their melting temperature [15]

Apart from the melting temperature another important aspect is an impact of the particle size on the mechanical properties of the material, which is of primary importance when used as construction or instrumental material. Studies [11–13] reveal that for most materials the mechanical properties such as strength limit and hardness considerably increase with a decrease in the grain size.

According to the Hall-Petch relation [8, 16], if the particle size decreases the hardness and strength of a crystal will grow:

$$\sigma_T = \sigma_0 + \frac{k}{\sqrt{d}}, \tag{1.1}$$

where σ_0 – frictional constrains needed for sliding of dislocations in a monocrystal (liquidity limit); k – the Hall-Petch constant that is individual for each crystal.

1.1.2. Mixing methods for nanopowders

Nanodisperse particles can be obtained with methods based on two essentially different concepts.

The first one implies dispersing coarse particles under physical processes (pressure, ultrasonic action, electrical dispersion, electro-chemical or chemical corrosion, laser method, gas condensation method, etc.); it is so-called *the top-down method*. For example, electrical explosion of conductors by means of a heavy impulse of electric current can be used.

The second method deals with fabrication of nanoparticles of finer elements (atoms, molecules) during chemical reactions, such as plasma-chemical synthesis, thermal synthesis (the top-down method) [17, 18]. It can also be dissolution of compounds (organometallic), setting of particles from the solutions, gas-phase condensation, etc.

Apart from a set phase composition, dispersion and other properties of the components in a ceramic, their homogeneous distribution in the batch is also very important. Powders can be mixed (without parallel grinding) by gas flow, mechanical impact (screws, blades, etc.) or by rotating the reservoir with a linear speed of about 1 m/s. Among the latter are bi-conical, V-shaped blenders, “drum tumbler” blenders and others. Better blending can be achieved by complicating the trajectory, along which the particles move. This trajectory depends on the location of rotational axis, form of the drum and drum-filling level (in most cases 35…60 %). Better mixing of heterogeneous components is provided by means of planetary mixers, in which the container rotates in three dimensions and the contest moves along a vortex trajectory.

The process can run in the gaseous or fluid medium. The fluid medium provides better mixing due to a higher pressure in the thin cracks as the result of the capillary forces, which provides an additional crushing of the components. Such an approach requires application of highly-wettable liquids (alcohol, petrol, water, etc.), which can be completely removed, and an additional treatment stage – drying. Components with different densities are mixed in vacuum or with the application of a special pattern of loading for light and heavy components.

The phase contact area S can be used as the quantitative variable describing the mixability of the powders. During mixing this value exponentially increases and asymptotically approaches a certain maximum value S_{max}. The dependency $S(t)$ is described by the equation

$$S(t) = S_{\max} \cdot \left(1 - e^{-k \cdot t}\right), \tag{1.2}$$

where t – mixing time; k – mixing velocity constant depending on the relative amount and dispersive capacities of the components.

An excess mixing time does not guarantee better distribution of the components. It can be even harmful if accompanied by additional grinding or an adverse reaction between the components, which can be the result of the heated mixture after the long mixing. The qualitative criterion of the mixture homogeneity is an average mean discretion of the given parameter Δ (chemical or granular composition) from its mean value according to the normal distribution law:

$$\Delta = \frac{\sqrt{\sum_{i=1}^{n} \frac{\left(a_i - \bar{a}\right)^2}{n-1}} \cdot 100}{\bar{a}}, \tag{1.3}$$

where a_i – single parameter measurement; $\bar{a}$ – average value of the parameter; n – number of tests.

The completely homogenized mixture has the same chemical and granular composition in any set macro-volume, therefore the mixing time t is chosen according to the condition $\Delta \geq 95$ %.

The mixing time can range from 5 min to several hours according to a mixer type. Biconical mixers with the capacity from 200 to 2500 liters perform the mixing in 1…2 hours; their efficiency is in the range from 100 to 1500 kg/h. The Turbula mixer with a working capacity of up to 400 liters creates a volume circulatory motion

of the particles and mixes them in 5…10 min; the efficiency is up to 2400 kg/h. More complex devices can automatically mix several solid components in the dry mixing unit with their subsequent transfer to the wet mixing unit where a liquid component is added. The humidity of the substance transferred can reach 20 % and the complete mixing cycle can last 4…12 min.

The mixing process is controlled either through technological testing of the batch (granulose composition, bulk density, fluidity, pressing and molding capacity of the mixture, physical and mechanical properties of blanks made of it) or chemical testing. The first method characterizes the mixture quality, however it is rather difficult and time-consuming, while the other one can give just a rough estimation. Typically, several technological characteristics of the mixture are controlled and the partial or complete chemical analysis is done. It should also be noted that a long storage of the mixture may result in segregation, i.e. the layering of the components with various densities. The preparation of a powdered mixture is the final stage before the molding [19, 20].

1.1.3. De-agglomeration methods for nanopowders

During mixing the heterogeneity coefficient decreases, but later on it can increase due to aggregation of particles. It reveals another valuable characteristic of nanoparticles (despite the method for fabricating) – their aggregating capacity. Thus, there is a need to consider not only the sizes of some (nano) particles, but also their agglomerates. During compacting this factor negatively affects the quality of the ceramics obtained, because an excess energy must be spent for obtaining the needed density and porosity. This energy will be spent for destroying the agglomeration forces. Agglomerated powders require higher temperature and external pressure unlike non-agglomerated ones [21].

Despite the method of their fabricating, the nanopowders are agglomerated, and their agglomeration level depends on the type of agglomerates. They can be soft and consist of particles joint under the Van der Waals forces, which can be easily destroyed under loading, and solid, which are partially sintered [22].

Even though some agglomerates are destroyed at the initial stage of pressing (soft agglomerates), their presence leads to the formation (in the sample's structure) of defects in the form of hollows (arch defects, inter-agglomerate pores), cracks, breaks [23, 24].

Agglomeration can be partially prevented even at the formation stage. The agglomeration level of nanoparticles depends on the surface development (and an excess energy), and the environmental temperature, an increase of which additionally

activates agglomeration. When settled from the gas phase, the particles are quickly transferred from the reaction zone to the zone of lower temperature in order to slow down their growth and agglomeration. Exclusion of water from some stages can positively impact the agglomeration level.

Another method for partial de-agglomeration is mechanical treatment of a powder in the ball drum.

However, neither method can eliminate agglomerates and prevent their formation. The ultrasonic impact with a consequent increase in frequency can be used as a more intensive method for de-agglomeration of nanopowders [25].

The de-agglomeration process can use not only mechanical action, but also unique physical and chemical properties of some substances – supercritical fluids, viscous resistance forces and pressure forces from expanding gasses [26, 27]. Supercritical fluids (SCF), e.g., supercritical carbon dioxide, the density and solubility coefficient of which are similar to those of a fluid, and the diffusion coefficient and viscosity are similar to those of a gas, is ecologically clean and can be considered as an ideal environment for de-agglomeration nanoparticles. It can penetrate into intra-agglomerate nanopores, and after a rapid decrease in pressure trigger the grinding and breaking of the nano-agglomerates from inside. The use of SCF for production of well-mixed nanocomposites has a lot of advantages, e.g. absence of organic solvents; treatment at the room temperature; possibility to avoid high stresses from compression or friction.

It was found that regarding agglomerated powders, the sizes of agglomerates are more important than the sizes of crystals. The bigger is the size of agglomerate, the larger is the size of inter-agglomerate pores (fig. 1.3).

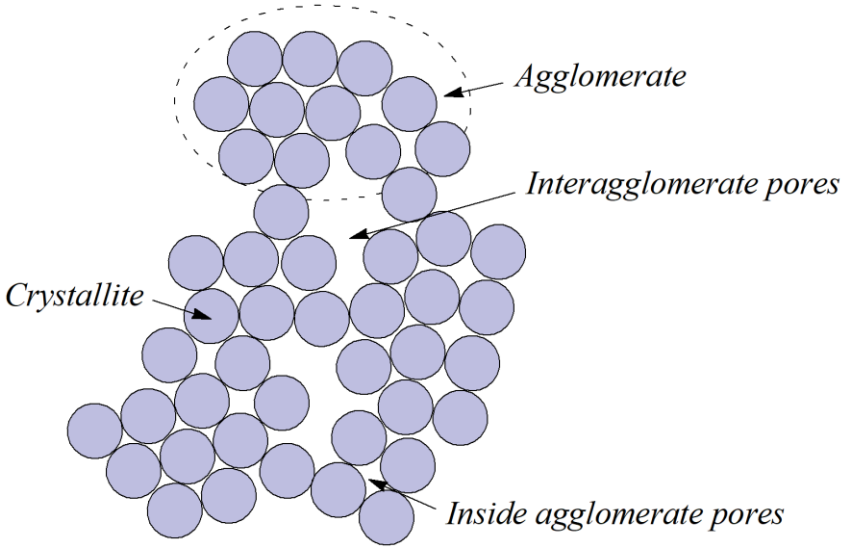

Figure 1.3 – Diagram of nanoparticle agglomerates and the pores they form

Big pores increase the diffusion distance and lead to a decrease in the decay rate. Lower density can be compensated by higher sintering temperature. However high temperatures can result in more granular structure, which complicates determination of the sizes of nanocrystal grains in the sintered material [28].

Without special techniques, it is possible to prevent interaction between individual particles in nanopowders. For example, nano-scale particles in powders can be maintained if they are used as suspensions with additives reducing the surface energy, or additives preventing aggregation of individual particles.

There are other techniques for protection of the surface of ultra-disperse particles, which can prevent coagulation and keep the particle activity. One of them is collection of materials in the organic nonpolar solvent with a surface-active agent. However, this technique is rather long-term and the output is small. Another technique is collection of particles in the water solution with oleic acid. It begins with adsorption of the monolayer on the surface of particles, when the concentration of oleic acid increases; a double layer is formed on the surface of particles. If the particles have the monomolecular layer of adsorbed acid, such particles coagulate in water. With a doubled adsorbed layer the particles are distributed in water uniformly and consistently. A monolayer is the result of chemical adsorption, and the second layer is formed through physical adsorption starting from hydrophilic groups (for example, magnetic ferrite particles). This technique maintains the Fe_3O_4 particles with a diameter of ~ 10 nm at the optimal temperature in the acid solution with the Fe^{2+} and Fe^{3+} ions; it is achieved through adding alkali [29].

1.2. Compaction methods for ceramics

1.2.1. Main regularities of sintering ceramics

Compaction of a powder material under external pressure and temperature is accompanied by a simple re-grouping of particles and complicated diffusion mass transfer processes. For simplicity the sintering kinetics of particles is described with their spherical radius *R*. A small initial area with the radius *x* is formed under the capillary force from the point contact. In the low temperature zone, where the thermal active processes are slowed down, a mass transfer in the yield flow mode can greatly contribute (gliding, doubling).

When the temperature grows (as well as the diffusion atom mobility) the contact area expands due to various non-threshold mechanisms: viscous current, volume, surface and grain diffusions. The neck increases due to the guided transfer of atoms

from the volume. The viscous coefficient, which specifies the rate of the process, is inversely proportional to the diffusion coefficient. The crystal centers become also closer when the neck grows due to accumulation of vacancies or dislocations out of the volume to their boundary (volume diffusion) and through this boundary (intra-granular diffusion). The transfer of a substance can also be made through the gaseous phase due to a difference of the equilibrium pressures of a pair near the concave and convex surfaces. The rate of such process is determined by the diffusion coefficient in the gaseous phase. The kinetics of the re-calculated mechanisms can be described as follows

$$x^n - x_0^n = A(T,R)(t - t_0), \tag{1.4}$$

where x_0, x – initial and current radius of the contact area; t_0 – initial time (at $x = x_0$); $A(T, R)$ – function depending on temperature, form and particle properties; $n = 2…5$ according to the mass transfer mechanisms [30].

If the particles of a powder body are evenly distributed in the space, even if the polyhedral particles are of various sizes in mutually perpendicular directions (i.e. the form which is different from spherical), it can be assumed that each length unit at any direction in the powder body has approximately the same amount of particles. And this powder body is called discrete-isotropous. If the probability of a mutual relative location of particles in the space is uneven, the particles, when forming the powder body structures, will tend to occupy a more advantageous position. In the process of pressing the powder particles tend to occupy such a position in which the maximum sectional area is almost perpendicular to the direction along which the formation forces are applied. Therefore, here, the number of powder particles per length unit in a powder body will depend on the mutual orientation of the particles, thus it will be uneven in various directions. Typically, the anisotropy of the properties of a powder body is complex [20, 31].

The prospective approach in obtaining compact nanocrystal materials, particularly ceramics, is hot pressing of nanopowders. However, when applying this method it is important to prevent grain coarsening at the sintering stage. It is possible at a high pressing density ($\rho = 0.7 \cdot \rho_m$), when sintering processes run rather rapidly and at a relatively low temperature $T \leq 0.5 \cdot T_{melt}$. However, nanocrystal powders are poorly compactable and conventional static compaction methods cannot provide such a high density, therefore, it is not easy to achieve such strong compacting. The physical reason of bad compacting capacity of nanonpowders is interparticle adhesion forces, the relative value of which greatly increases with a decrease of the particle size [32].

Primarily, the porosity of nanoceramics is conditioned by the pores in the triple joints of crystallites and on the grain boundaries. A decrease in the powder dispersive capacity goes along with a noticeable decrease of their density in compaction at the same pressure [33]. A decrease and more uniform distribution of porosity are achieved by means of higher temperature during pressing, which can lead to undesirable re-crystallization.

1.2.2. Hot pressing of ceramics

In recent years the world advanced trends in science and engineering are research into nanomaterial, particularly, application of nanopowder metallurgy for solution of actual material science problems [34–36]. Among other things, the problem of compaction of powders, especially high-sintering materials and compounds (carbides, borides, nitrites, silicides), melting temperature of which is very high and plasticity is low, is of interest. The most effective way to sinter these materials is hot pressing [37]. It gives the density close to theoretical at a relatively low external pressure and temperature (P = 30 MPa, T = 1300…2000 °C) [38–41].

The mass transfer and compaction processes during solid-phase sintering of high-melting compounds are complicated due to high stability of their lattice and, consequently, suppressive nature of the diffusion-viscous current processes.

These processes can be accelerated either with activating additives (components of the batch if they are ultradisperse), or with special features of the sintering method chosen [42, 43]. The consolidation speed when applying FAST-technologies can be increased by several orders of magnitude in comparison with conventional sintering due to a relatively short treatment period that compensates higher energy capacity.

Despite the fact that the impact of electric current on sintering of powders is well studied [44], its application together with other techniques (impulse [45], pressing [46]) is an impetus both practically and theoretically.

1.2.3. FAST-methods of electric consolidation

FAST (Field Activated Sintering Technique) [47] and SPS (Spark Plasma Sintering) [48] technologies are used for fabricating low-porous structures. They are based on simultaneous application of external pressure and heating with the field and direct (respectively) action of electric current, which is characterized by high efficiency (table 1.1).

These technologies can considerably speed up heating and shorten the sintering time (up to several minutes), thus there is not enough time for bigger grains to be formed.

Table 1.1 – Consolidation methods for powder materials

Consolidation methods	Pressure, GPa	Temperature, °C	Product density, %	Heating rate, °C/s	Hold time, min
Hot isostatic forging (HIF)	1.0	1200…1500	≥ 95	10…20	2…5
Quick hot isostatic pressing (QHIP)	1.0	1200…1500	≤ 95	20…30	1…5
Sintering with electrically-activated impulse field (FAST/SPS)	0.06	≤ 2200	≥ 95	20…30	3…5
Field activated Pressure Assisted Sintering (FAPAS)	0.03	≤ 3000	≥ 95	10…20	2…3
High Energy High Rate Processing (HEHR)	1.5	≤ 3400	≤ 98	20…30	1…2
Super-high pressure sintering	26	≤ 2000	94…98	3…4	5…10

Study [49] shows that FAST-methods include the already-mentioned SPS and PAS (Plasma Activated Sintering), PECS (Pulse Electric Current Sintering) owing to the presence of a field action of electric current and thus, its activating action on the medium. Both FAST and SPS run at rather low frequencies [29], which amount to approximately 70 and 60 Hz (fig. 1.4).

Evidently, low AC frequency increases a probable release of electromagnetic energy in the form of electric charge in longer semi-periods (both direct and reverse polarity) in comparison with high-frequency generation, thus this increases the effect of spark plasma in sintering.

Studies [50, 51] show that the concept of improved properties of sintered materials is based on the activation of compacting, which should run before the grain growth.

This approach is the most effective for submicro- and nanopowders, when the formation of ultra-dense and finely-disperse structure is the central target function which is aimed at technological support of competitive operational characteristics of the finished product [52, 53], and especially efficient for combined technologies based on electric consolidation [54–57].

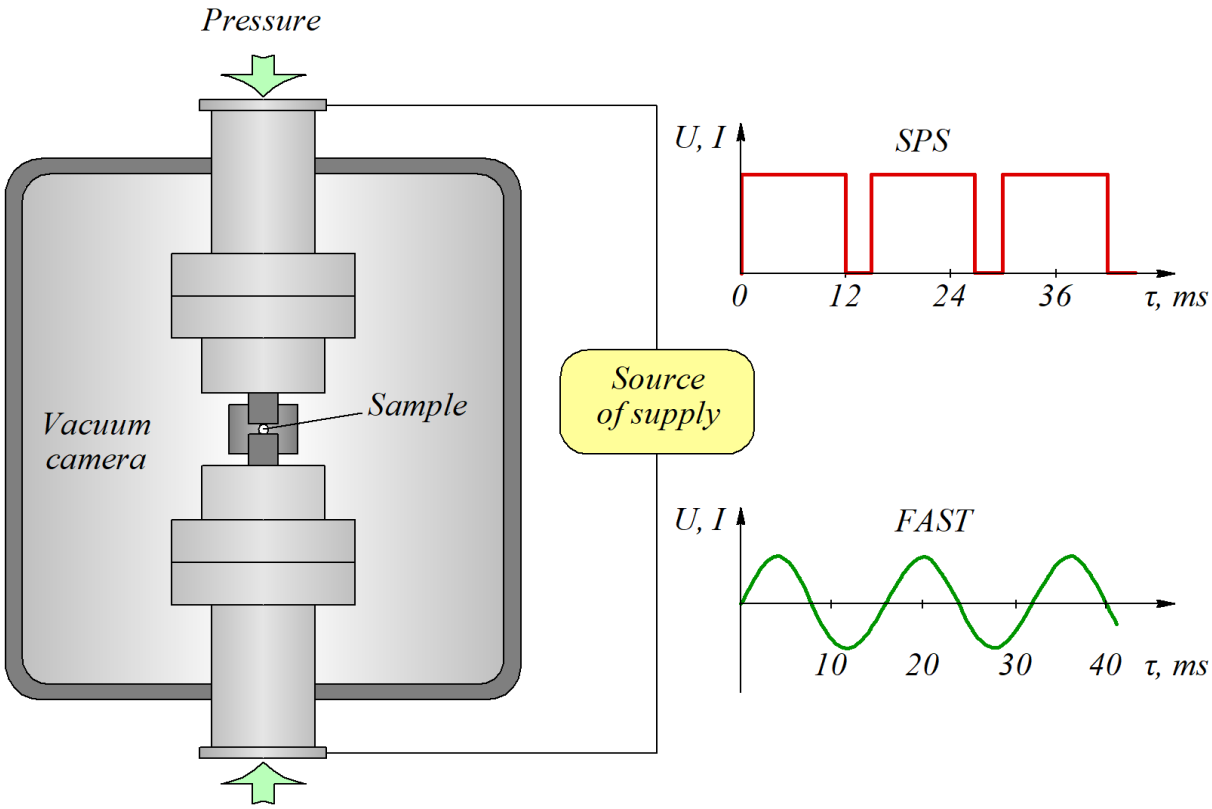

Figure 1.4 – Hot pressing installation for SPS/FAST methods

The experience [58–61] demonstrates that for nanodisperse powders (~ 100 nm) the inclusion of the batch into the electric circuit during consolidation is justified for both conductive and dielectric components of the mixture. In the former case (conductive components) electrodischarge processes on the particle boundaries run in accordance with the mechanisms of electrical contact interaction (fig. 1.5) [62]. In the latter case (dielectric components) there can be discharges distributed beyond the interface of the media with different dielectric permittivity according to the guided spark theory, thus beyond the grain boundary [63]. The local formation of plasma due to electrical discharges results in the clearing and activating of the surfaces of powders being sintered [64]. The cleaning of grain boundaries during consolidation helps eliminate heterogeneous layers, both non-conductive and impurity, with a depth of up to 5 nm on the surface of conductive particles, which considerably improve the chemical purity of the finished product and compaction of sintered powders [65–69].

With pores in the media where electric current runs (fig. 1.6) the electric current density, in the zones where the electric current flows, increases and, consequently, the temperature rises [45]. As far as near the pores with bigger cross-sections the temperature increases more, there occurs a temperature gradient initiating the diffusion of structural vacancies from the large pores to small ones.

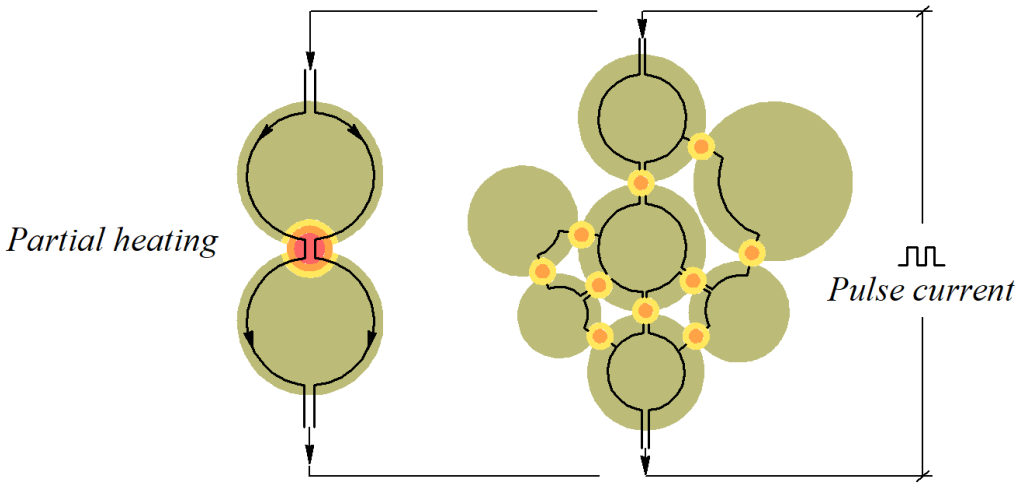

Figure 1.5 – Formation of spark discharges on the powder particle boundary [70]

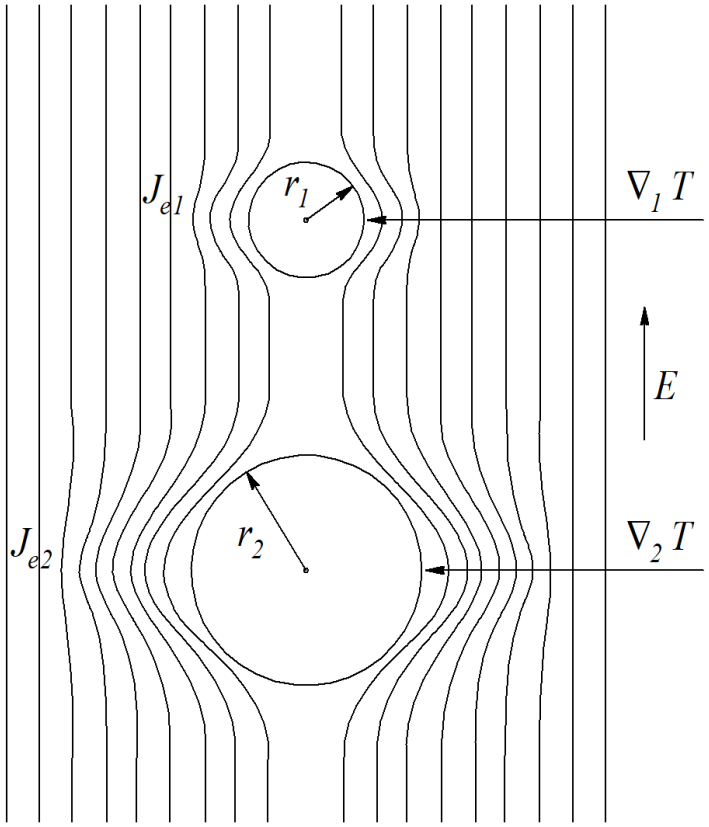

Figure 1.6 – Change in the current density ($J_{e2} > J_{e1}$) and the temperature gradient ($\nabla_2 T > \nabla_1 T$) near large (r_2) and small ($r_2 > r_1$) pores in the electric current of the electric field intensity E [45]

Thus, the current density across the section of the sintered volume becomes equal and large pores become fragmented. And, due to smaller sizes of some pores the scale of internal defects and crack formation in finished products decrease. Therefore, electric consolidation is favourably compared with conventional furnace sintering

during which the re-distribution of pore sizes runs towards an increase of large pores and a decrease of the sizes and amount of small ones [65].

According to the theoretical grounds [44] the accelerated consolidation by means of electric current can be explained by local fusing of compacts (welding) of powder particles and an additional mass transfer due to internal temperature gradients in the material because of the heterogeneity of electric current density between the pores. However, these conclusions are applicable only for current conductive powder mixtures.

1.3. Overview of the main types of ceramics and their areas of application

The continuous technological development of the mankind requires new materials with better physical, mechanical and tribological properties; and ceramics can be viewed as such materials. Despite the fact that ceramics have been used since the earliest times [30], only up-to-date raw materials and production technologies can guarantee the characteristics which are required at the present technological development stage.

Two notable characteristics of ceramics are the chemical composition and the production technology. As generally accepted, ceramics are polycrystalline materials obtained through annealing, in which at least one component is non-metal, thus it is a combination of elements of the III–IV groups of the periodic system with metals or non-metals. And during sintering the temperature does not reach the melting temperature of the main component unlike that in metallurgy technologies (with an exception of powder metallurgy) [71].

The physical properties of a solid body depend on the bond types of its components in the crystal grid. In ceramics this binding is mixed and coordinate-covalent. Absence of free electrons is the reason why ceramics are poor conductors of electric current and heat; therefore, they are used as heat and electrical insulators. The substances with narrow gap between Brillouin zones are used as semi-conductors [71].

In chemical industry ceramics are used for production of sorbents, catalytic converters (and their carriers), electrodes, gas humidity sensors, and also chemical reactor elements. Here, the following material properties are used: absorbing and adsorbing capacity, catalytic activity, and corrosion resistance.

The ceramics types used in industries are given in fig. 1.7. The most frequently used in this field are oxide ceramic (Al_2O_3, ZnO, SnO, SiO_2, MgO), titanium diboride (TiB_2) and zirconium diboride (ZrB_2) and also titanides [72].

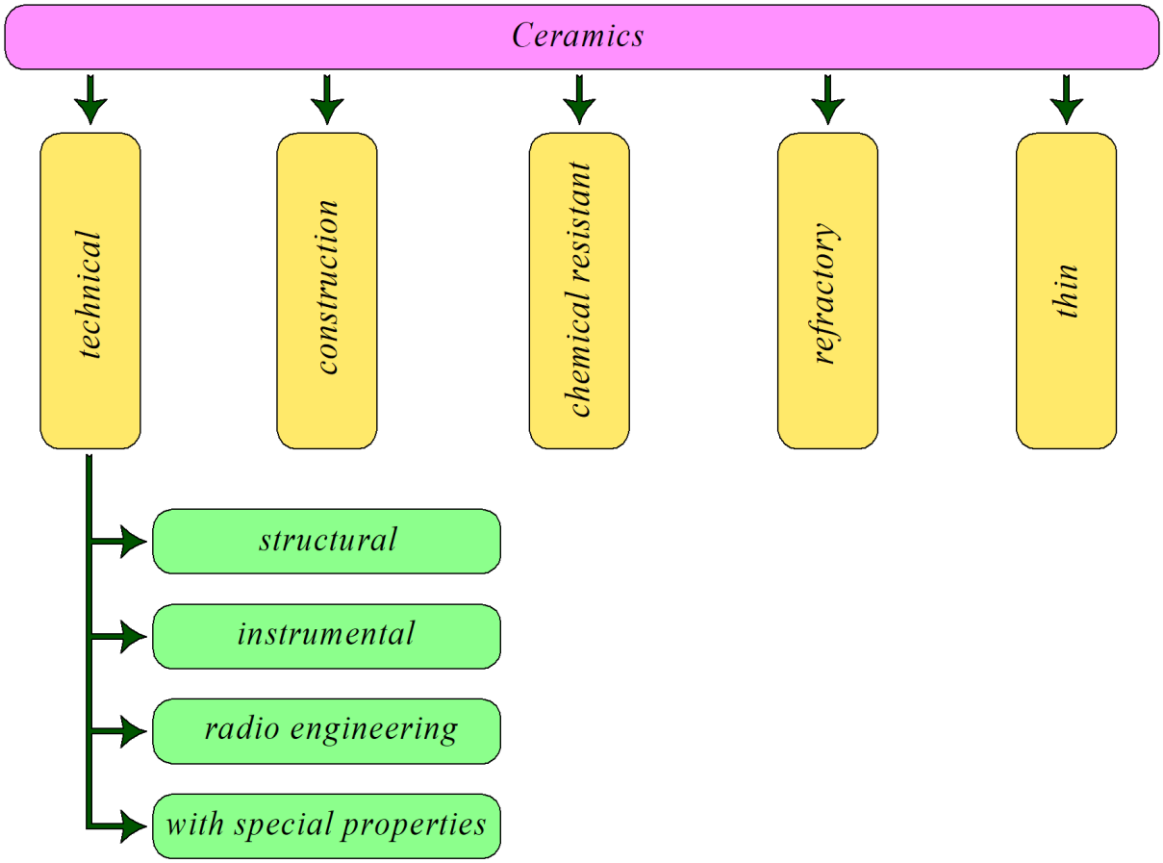

Figure 1.7 – Ceramics by industries in which they are applied

Due to biological compatibility and resistance to biocorrosion, oxide ceramics (Al_2O_3, ZrO_2) are widely used for production of endoprosthesis – teeth implants and joints. Such joints consist of friction pairs, either ceramic-metal or ceramic-ceramic [73, 74].

The ceramic polycrystalline structure impacts their heat and temperature conductivity, and these characteristics are much poorer in metals and even alloys. And, consequently, such their characteristics as high temperature strength, high temperature resistance, *TEC*, heat conductivity make them appropriate for fabricating various refractory products, linings for high temperature reactors, heat exchangers, etc.

The following ceramics are used for these purposes: white oxide ceramics (Al_2O_3, TiO_2, BeO, MgO, ZrO_2), carbide ceramics (SiC, TiC, B_4C) and others (Si_3N_4, BeS, CeS) [75].

1.3.1. Instrumental ceramics

Ceramic materials are widely used in different industries, such as electronics, metal working and structural part production. However, due to effective combination of mechanical properties (hardness, TEC, etc.), the most effective approach is their application as instrumental materials.

The required physical and mechanical properties of instrumental ceramics can be only provided with solid components – oxides, carbides, and nitrites. Such ceramics are divided into four main groups by composition:

– oxide (white ceramics) – based on Al_2O_3;

– mixed (black ceramics) – based on Al_2O_3 + Ti (N, C);

– nitride-silicone ceramics – based on Si_3N_4; and

– reinforced – Al_2O_3 with the SiC fabrics.

Fig. 1.8 and 1.9 give the temperature dependencies between the hardness and the strength limit of various instrumental materials [76–78].

A special feature of ceramics is absence of a binding component that helps achieve high heat resistance qualities (up to 1400 °C) and hardness (up to 96 HRA). It is ideal for production of cutting tools because the processing speed can be increased several times (for tempered steels – up to 100…150 m/min and for cast irons – up to 500…1200 m/min) in comparison with hard-melting tools [79].

Application of ceramics for cutting tools can greatly broaden the nomenclature of process materials [80–86].

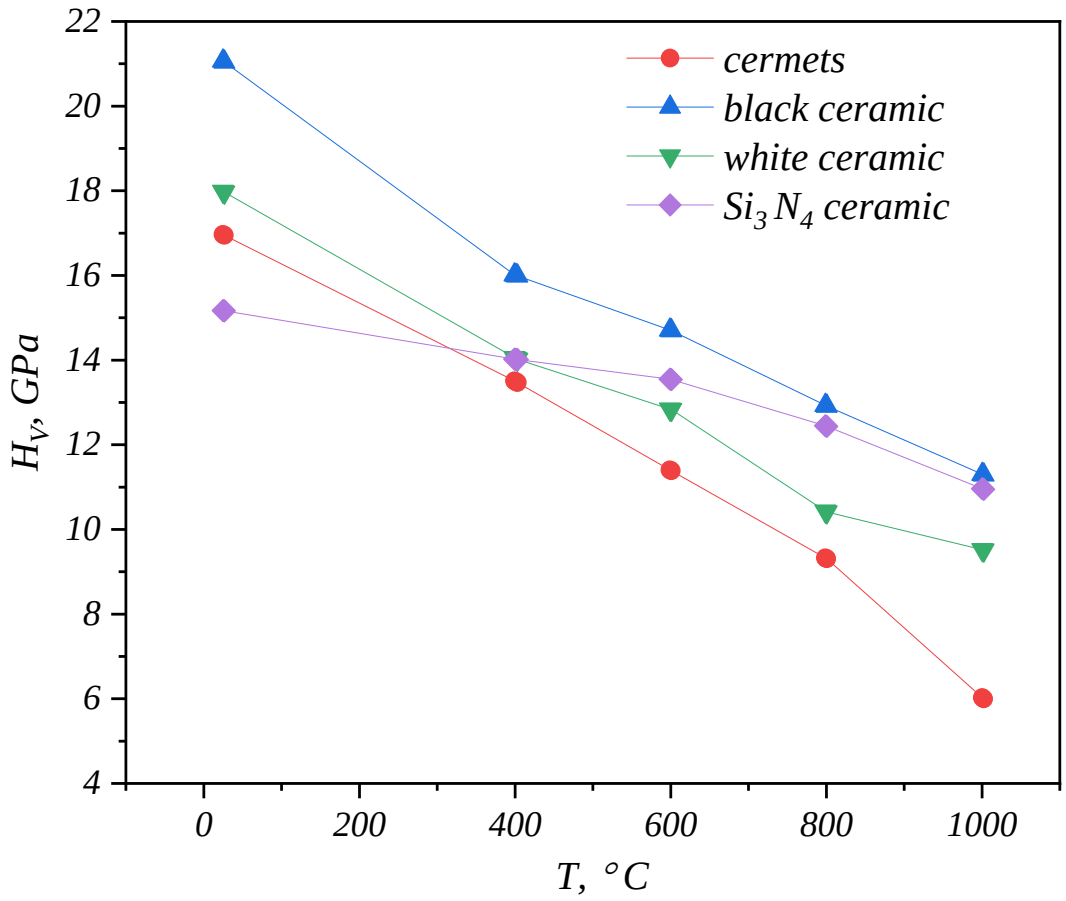

Figure 1.8 – Temperature dependencies of micro-hardness of cutting ceramics

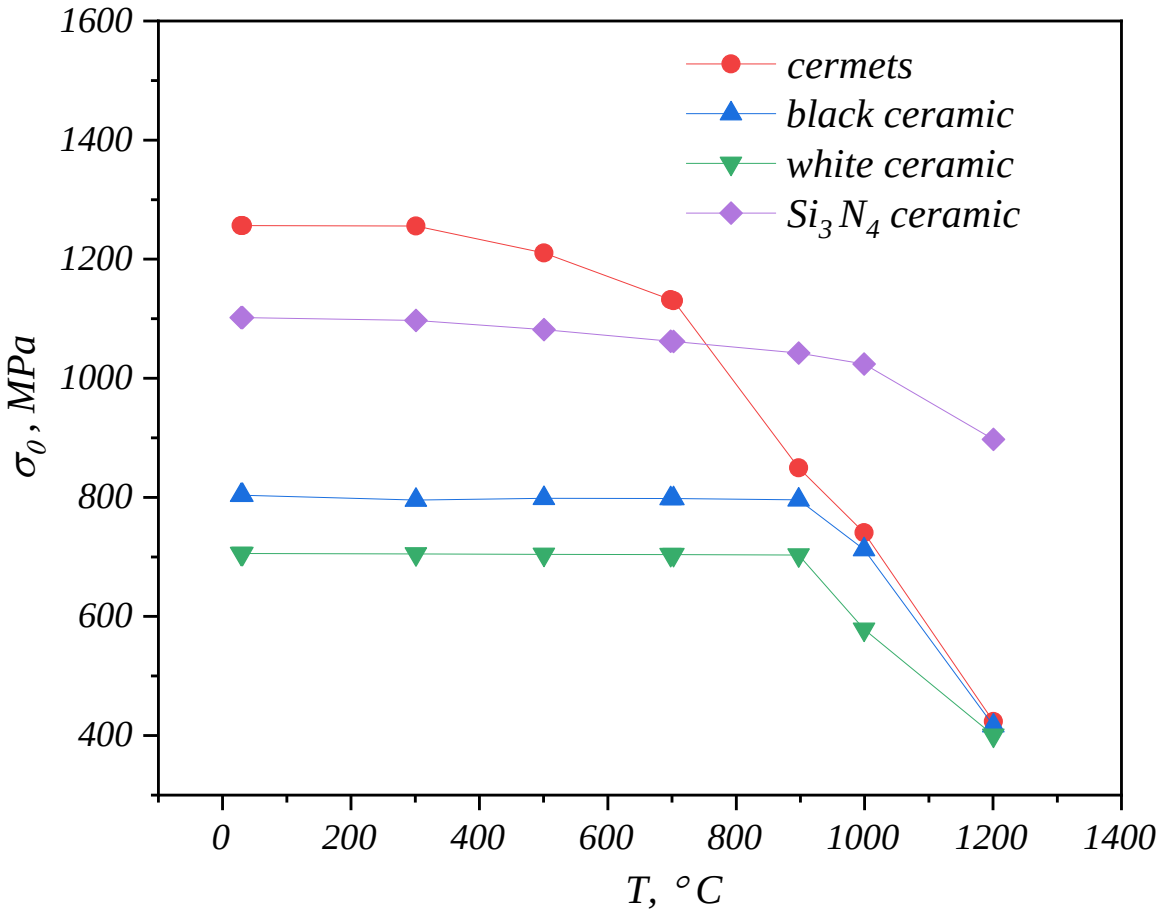

Figure 1.9 – Temperature dependencies of the strength ratio of cutting ceramics

On the contrary, the absence of a plastic component negatively impacts the sensitivity to temperature changes, embrittlement, impact viscosity and crack resistance, because cracks, when developed, can propagate without any obstacles [87, 88]. Due to specific conditions (high mechanic and temperature loading), instrumental ceramics have to be hard, heat and adhesive resistant. And only combination of these characteristics can resist negative factors in operation.

About 96…99 % of oxide (white) ceramics consists of Al_2O_3 (alumina) and oxide additives which, due to the glass phase formation, both activate the sintering process and prevent re-crystallization of the base grains (MgO, CaO, MgF_2, SiO_2 etc.) [89, 90]. Owing to the physical and mechanical characteristics of Al_2O_3 white ceramic is wear-resistant when applied for most process materials.

The possibility to implement the free sintering technology for production of cutting plates based on alumina, availability and relatively low cost of raw materials are the core criteria why white ceramics has been in effective use during a lot of years.

Ceramic cutting tools of pure Si_3N_4 are produced by means of hot pressing with addition of MgO; their hardness is 91…93 HRA, torsion strength reaches 850 MPa,

and heat resistance can be 1300…1400 °C, besides, they keep their high oxidation stability [91].

This ceramic has a low friction coefficient, high adhesion capacity and can be used for processing aluminous alloys and other materials. Silicone nitride can be used as the basis for production of composite materials. As the second phase they have solid dispersed heat-resistance carbide or nitride of the second phase; they are characterized by high hardness, strength, fracture viscosity and a lower heat extension coefficient.

The composite ceramic cutting tools of Si_3N_4 are more sustainable in comparison with those of pure Si_3N_4 and their oxidation stability is higher. Therefore, such cutting tools are especially appropriate for coarse and pure finishing, high-speed cutting, cast iron and high-temperature alloy processing. The areas of application for various ceramics are thoroughly studies in works [92–94].

In hot-pressed silicone nitride the porosity is almost equals zero, the tensile strength at the room temperature can be 800…1000 MPa. Also the following materials can be used for production of cutting tools:

– cermets – ceramic-metallic composite materials based on Ti (C, N) reinforced with carbides of high-melting metals (WC, TaC, VC). Cutting tools made of these materials can be used for processing brittle steel, alloy steel, cast iron, fiberglass and other non-metal materials and for clean finishing steel and cast iron at cutting speeds of 300…500 m/min [95];

– ceramic composites reinforced with wire-type crystals (fig. 1.10). They are resistant to impact loading and thermal impact; they can be used for processing steels with high (HRC ≤ 65) and medium hardness at high speeds [96]; and

– functionally-graded materials the properties of which are heterogeneous in total volume (fig. 1.11). They can be produced by treating surfaces, e.g. nitriding. And their service life is longer [97].

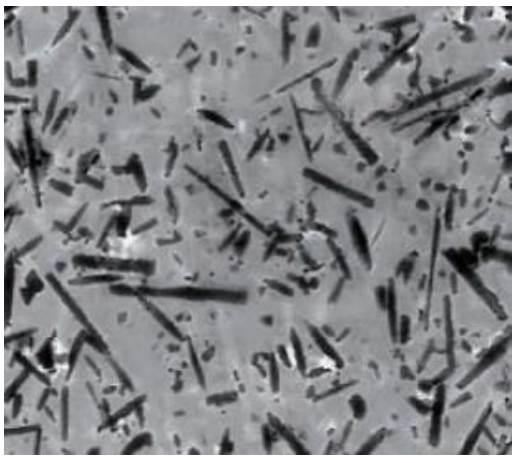

Figure 1.10 – Structure of Al_2O_3 ceramics reinforced with wire-type SiC fibres

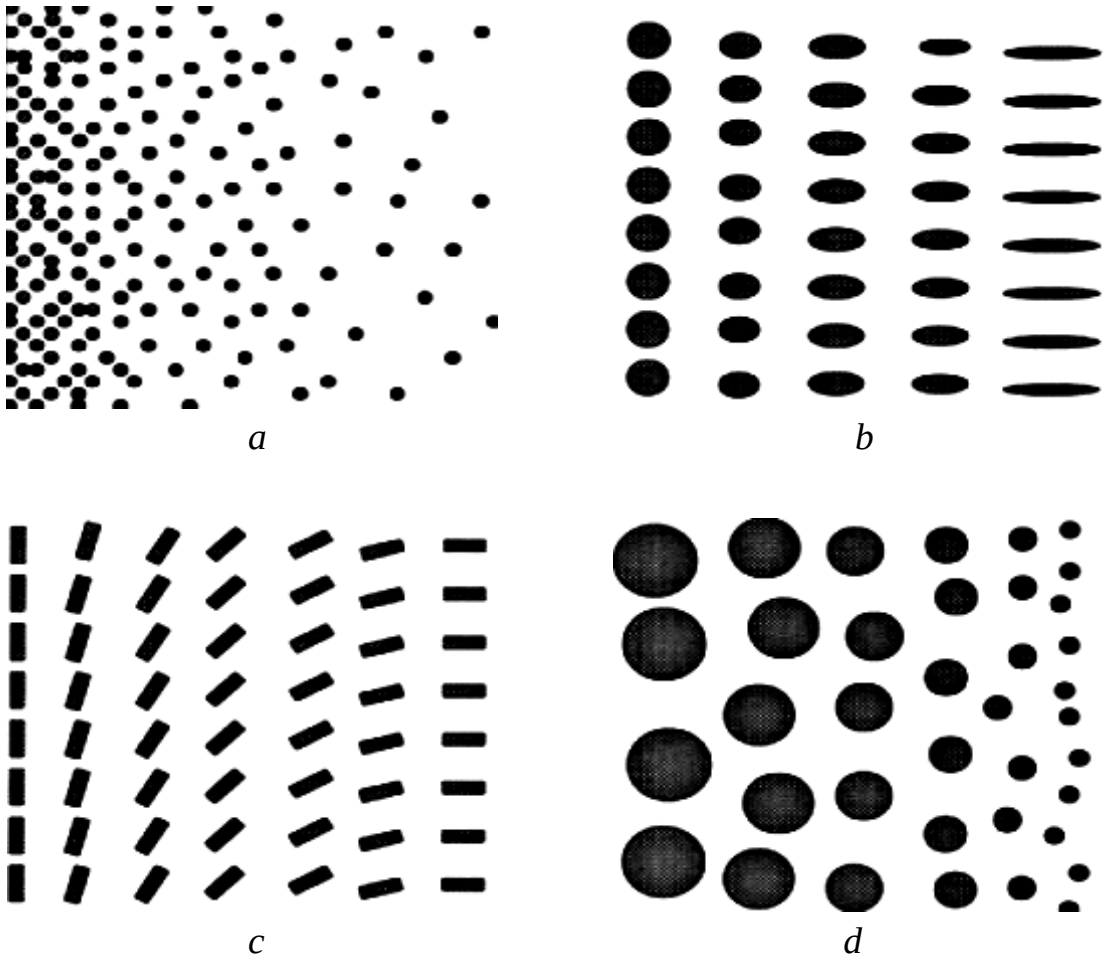

Figure 1.11 – Various types of functionally graded composites [98]:
a – fraction gradient; *b* – form gradient; *c* – orientation gradient; *d* – size gradient

1.3.2. Properties of the ceramic based on Al_2O_3 and perspectives of its application

The materials used for producing cutting tools must be hard, especially when heated, have a low thermal expansion coefficient, and high wear and heat resistance. Table 1.2 shows that regarding these characteristics oxide ceramic materials are much better than conventional materials – solid alloys and high-speed steels.

Table 1.2 – Characteristics of different cutting materials [99]

Characteristic	Material		
	High-speed steel	Solid alloy R10	Ceramic based on Al_2O_3
Softening temperature, °C	550	1100	1500
H_V, GPa	8.5	17.0	21.0
Scaling temperature, °C	1070	1070	–

High values of hardness and heat resistance of tools made of cutting ceramic based on Al_2O_3 greatly speed up the mechanical processing of steels and cast irons in comparison with processing speeds for tools made of hard alloys and high-speed steels (table 1.3).

Table 1.3 – Cutting speeds for ceramic and hard alloy tools

Process material	Hardness, HB	Cutting speed, m/min	
		ceramic	hard alloy
Gray cast iron	143…289	300…400	100…200
Ductile cast iron	140…369	200	50…100
Carbon steel	150…250	250…300	100…200
Alloy structural steel	179…241	100…160	25…65

Application of ceramic for enlarged cross-sections of cut or skip cutting considerably decreases the efficiency due to high probability (over 50 %) of abrupt failures caused by brittle fractures in the form of crumbles and spalls [100].

One of the ways to improve the strength and crack resistance of ceramic tools is development of multi-phased ceramic based on Al_2O_3, particularly, through reinforcing with mono-crystalline silicone carbide fibres (whisker ceramics) (fig. 1.12). Grade CC670 produced by “Sandvik Coromant” is an example of such cutting materials. The advantage of this ceramic is its stability under non-continuous processing, including impacts, when white and black ceramics typically break due to spallation.

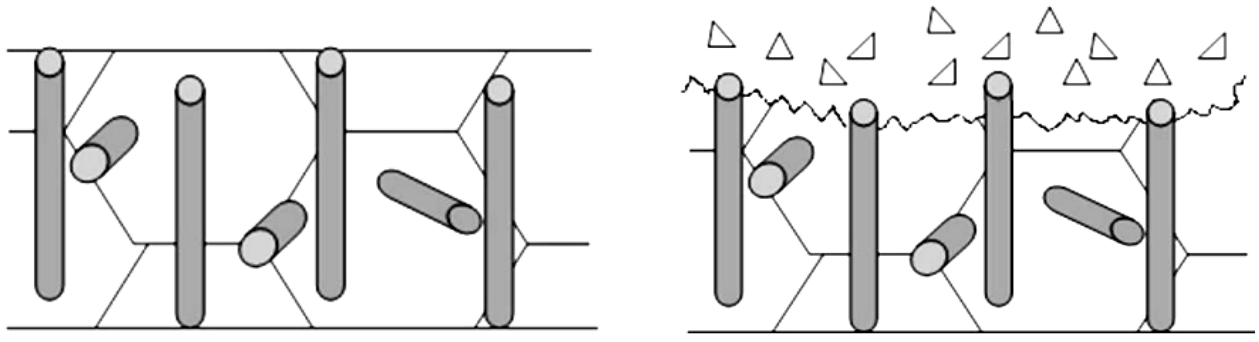

a *b*

Figure 1.12 – Surface layer of a reinforced ceramic before (*a*) and after (*b*) mechanical interaction [101]

An insufficiently wide application of this reinforced ceramic is explained by its high diffusion and adhesive activity of silicon carbide fibers towards alloys based on

Fe, Ni, Co and others; this increases the wear of tools working at high cutting temperatures.

1.4. Mechanical treatment with cutting ceramic tools

Research into the process of heat formation and transfer during metal processing [102–105] testifies that heat processes accompany the mechanical processing of metal materials; in the process of cutting 99.5 % of work transfers into heat. The characteristics of tool and detail under processing depend on the temperature (thermal expansion and lower capacity of properties with higher T); apparently it is the cause of lower wear resistance of the tool and the surface quality of the detail. The main sources of heat Q in the cutting zone (fig. 1.13) are primary deformation area ($Q_{D.Prim}$), secondary deformation area ($Q_{D.Sec}$) and tertiary deformation area ($Q_{D.Tert}$). In most cases radiation losses are neglected – they are very small.

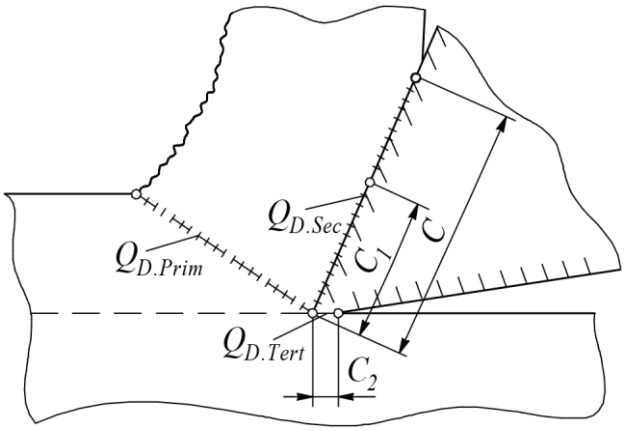

Figure 1.13 – Heat sources in the cutting zone during metal turning

Obviously, the highest temperature is observed on the frontal edge of a cutting tool, because the maximum amount of heat is concentrated in the contact area between the chip and the cutting tool; it consists of the heat $Q_{D.Prim}$ and $Q_{D.Sec}$. The formation of the average cutting heat Q_{cut} is described by the following expression:

$$Q_{cut} = Q_{D.Prim} + Q_{D.Sec} =$$

$$= \frac{\alpha_0 \cdot p \cdot \left[\left(1-\beta_0\right) - \left(\sin\gamma + \mu_0 \cdot \cos\gamma\right) \cdot \frac{1}{\xi} \right]}{E \cdot C_p \cdot \rho} + \frac{F_n \cdot \sqrt{\frac{v \cdot \pi}{4 \cdot \xi}}}{E \cdot b \cdot \sqrt{\lambda \cdot C_p \cdot \rho \cdot l}}, \qquad (1.5)$$

where α_0 – coefficient including heat losses due to the hidden deformation energy; p – specified cutting force; β_0 – coefficient including a partial heat transfer to the workpiece (about 0.1); γ – orthogonal rake angle of the cutter; E – mechanical equivalent of heat; C_p – heat capacity of the metal chip heated; ρ – chip density; b – width of the cut; λ – heat conductivity of the cutter; F_n – friction force on the front edge; ξ – chip shrinkage; v – cutting speed [106].

The friction on the flank face of a cutter can be neglected because with high sharpening this contact area shrinks to zero [107]. The maximum amount of heat is formed in the deformation zone ($Q_{D.Prim}$); it partially transfers to the workpiece and partially – to the cutting tool. For process metals with low heat conductivity (heat-resistant and titanic alloys), up to 40 % of all the heat is transferred to the cutting tool.

Expression (1.5) demonstrates the effect of different factors on deformation heat and friction heat. As seen, the friction heat is proportional to the cutting speed and inversely proportional to the heat conductivity of the material of the cutter. For a ceramic cutter the temperature in the cutter-chip friction area (fig. 1.14, *a*) is higher, than for a carbide cutter (fig. 1.14, *b*) because of the considerably low heat conductivity of ceramics. With a cutting speed increase, the temperature of the cutting tool rises due to the friction on its front surface.

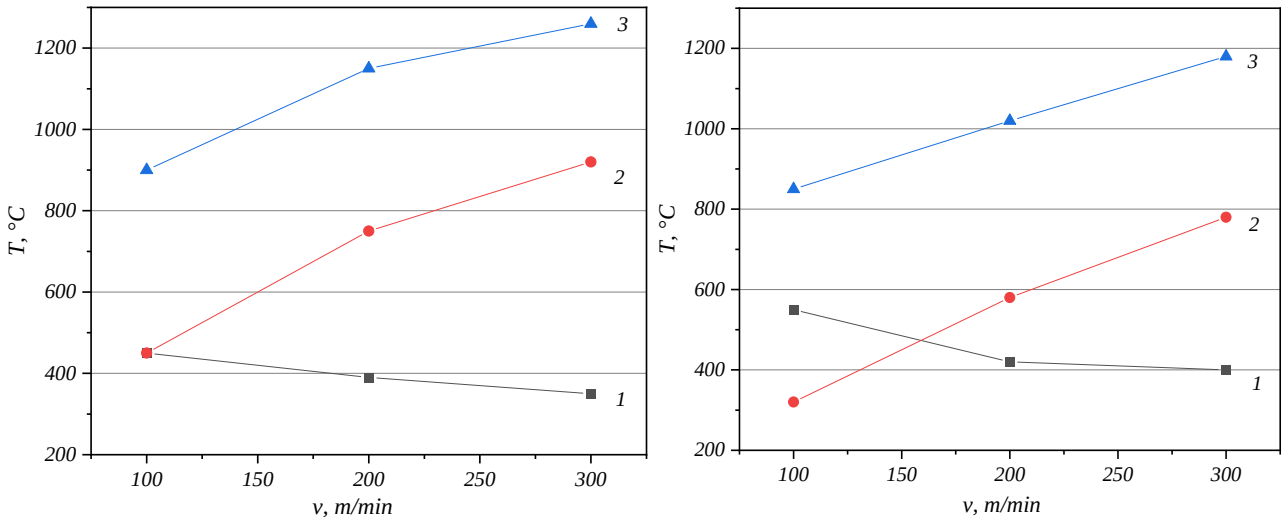

Figure 1.14 – Change in the components of a cutting temperature in the process of steel working for ceramic (*a*) and carbide (*b*) cutters:
1 – $Q_{D.Prim}$; *2* – $Q_{D.Sec}$; *3* – Q_{cut}

A temperature increase can change the configuration of the workpiece and the tool due to the heat expansion. Fig. 1.15 shows the dependencies between the extension

of the ceramic cutter and the cutting time. If the temperature of the cutting edge increases by 800 degrees, the extension is about 75 mkm, which can be compared to the finishing stage [108].

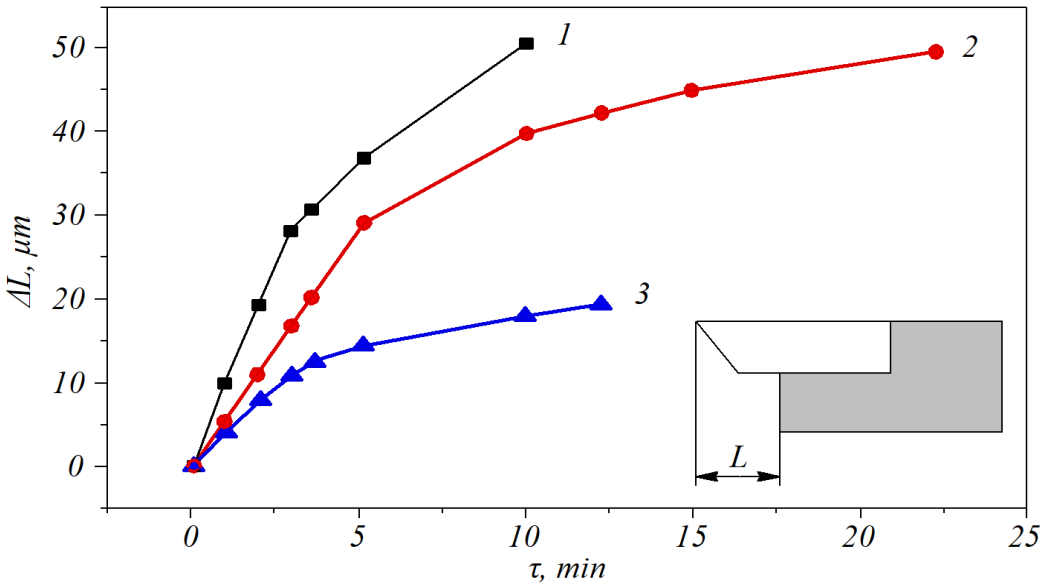

Figure 1.15 – Time diagrams for thermal extension of a ceramic cutter:
1 – L = 3 mm; *2* – L = 1.5 mm; *3* – chip is removed from the cutter

Thus, during the processing of metals with low thermal conductivity (heat-resistant and titanium alloys) great amount of heat is transferred to the cutting tool, which worsens its strength characteristics and causes its rapid wear. This fact is of particular importance to ceramic cutters with relatively low thermal and temperature conductivity.

CHAPTER 2

ELECTROCONSOLIDATION FOR NANOPOWDER COMPOSITES Al_2O_3 AND SiC

2.1. Consolidation of Al_2O_3 and SiC powders

The ceramic samples of powder batch were produced with the unique hot pressing installation where AC passed through the press mold and the sample. The composition of the sample and the pressing parameters are given in table 2.1.

Table 2.1 – Composition and pressing parameters of an Al_2O_3–SiC sample

Code	Composition	T_{sint}, °C	t, min	P, MPa	Dispersity
AS0-6	Al_2O_3	1600	3	35	mirco
As15-6	Al_2O_3 + 15 mass % SiC	1600	2	35	micro-nano
As15-4	Al_2O_3 + 15 mass % SiC	1400	2	35	micro-nano
As15-7	Al_2O_3 + 15 mass % SiC	1700	2	35	micro-nano
As15-4	Al_2O_3 + 15 mass % SiC	1700	3	35	micro-micro
As15-7	Al_2O_3 + 15 mass % SiC	1700	3	35	micro-nano
As15-6	Al_2O_3 + 15 mass % SiC	1600	3	35	micro-micro
as80-6	Al_2O_3 + 80 mass % SiC	1600	4	35	nano-nano
as50-7	Al_2O_3 + 50 mass % SiC	1700	4	35	nano-nano
as80-8	Al_2O_3 + 80 mass % SiC	1800	4	35	nano-nano
azs80-7	(ZrO_2 + Al_2O_3) + 80 mass % SiC	1700	4	35	nano-nano
as10-5	Al_2O_3 + 10 mass % SiC	1500	4	35	nano-nano
as50-6	Al_2O_3 + 50 mass % SiC	1600	4	35	nano-nano

The first letters of the code (table 2.1) indicate the batch composition and the powder types used. The letters *a* and *A* indicate nano- and micro-Al_2O_3, respectively (*S*, *s* – SiC, *z* – ZrO_2). The number after the letters indicates the content of SiC in % (by mass).

The last number indicates the sintering temperature: 5, 6, 7 – 1500, 1600, 1700 °C, respectively.

2.1.1. Mechanisms and stages of sintering

The consolidation of a powder material consisting of separate particles runs with their re-grouping and deformation. Some compaction mechanisms can only be activated if the pressure or temperature reaches a certain level (threshold mechanisms). If the value of the mechanical stress (temperature) applied does not impact the deformation, a solid body behaves as a Newtonian fluid, but with a variable yielding coefficient that depends on the structural condition (non-threshold mechanisms) [109].

The mass transfer mechanisms responsible for sintering in polycrystalline materials are crystalline lattice diffusion, surface diffusion, voluminous diffusion, plastic deformation and evaporation-condensation.

Fig. 2.1 demonstrates that all mass transfer mechanisms are directed to the contact point between two particles. The first three mechanisms mentioned do not displace the mass center of the particles, thus they have nothing to do with compaction [110].

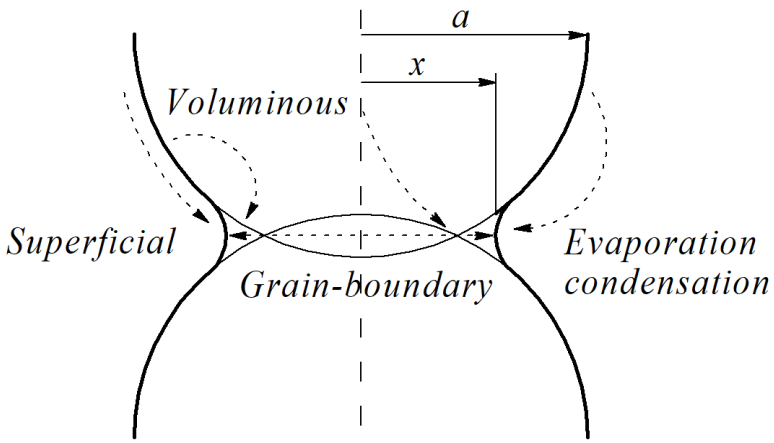

Figure 2.1 – Diffusion mechanisms during sintering of spherical particles

For simplicity the sintering process is divided into stages, though they can run simultaneously or sequentially according to the initial formation characteristics and sintering conditions.

Fig. 2.2 gives time dependencies of the sintering parameters for a sample consisting of Al_2O_3 and 15 % SiC and sintered at a temperature of 1600 °C (As15-6). At the initial stage the heating speed was about 200 °C/min.

The initial sintering stage includes re-grouping of particles, which runs together with their friction; the speed of shrinkage is constant.

This stage is characterized by formation of point contacts of their surfaces the amount of which grows rapidly.

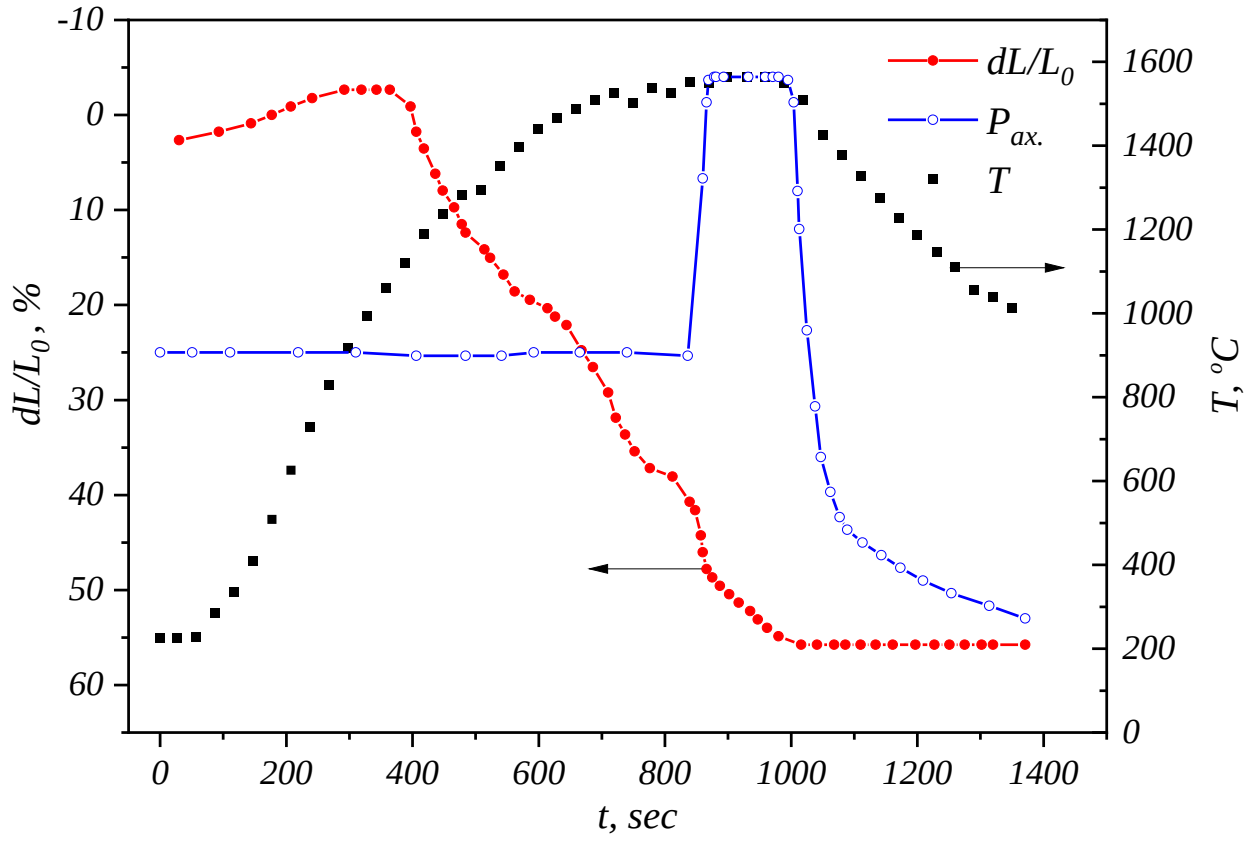

Figure 2.2 – Pressing map for an As15-6 sample

However, each particle keeps its structural pattern, thus the boundaries between the particles are kept as well as the concept of the intergrain boundary. The pores join to each other. With an increase of the pressure and deformation of the particles in the point contact area, so-called “necks” are formed between them [111]. This stage is characterized by a rapid shrinkage of the particle surface because of a rise in the number and the cross-section area of the necks, and, consequently, a reduction of pores. The grain growth remains slow.

The time dependency of a linear shrinkage of a sample (fig. 2.2) demonstrates non-linearity at the initial stage (400…800 s). With time differentiation we can find the moment of an abrupt change in shrinkage.

Fig. 2.3 gives the curves of linear shrinkage dL/L_0 and its derivative $d(dL/L_0)/dt$ which has the physical nature of speed.

The analysis of data on the pressing of another sample (As15-7) also revealed the similar behavior of the linear shrinkage curve (fig. 2.4). For the first sample it was observed at $T = 1450$ °C, and for the As15-7 sample – at $T = 1400$ °C. The both samples had a 15 % additive of nanodisperse SiC powder in their initial mixture compositions.

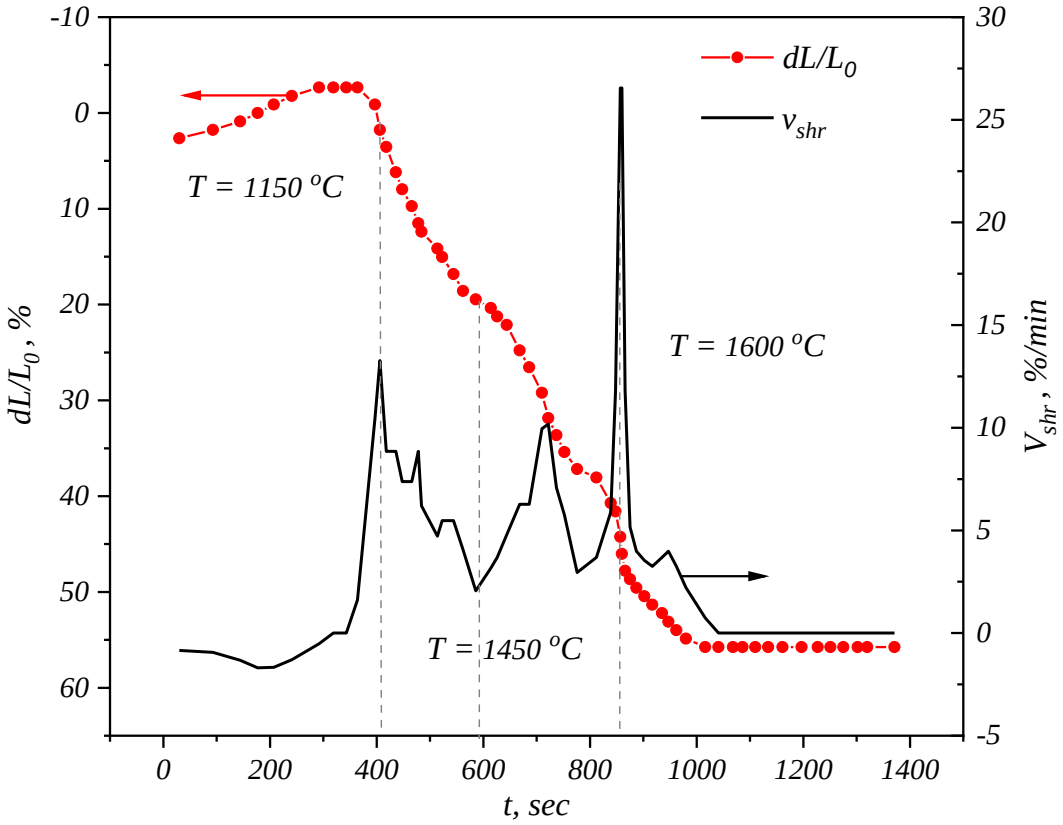

Figure 2.3 – Time dependencies of the relative linear shrinkage dL/L_0 and its speeds V_{shr} (sample As15-6)

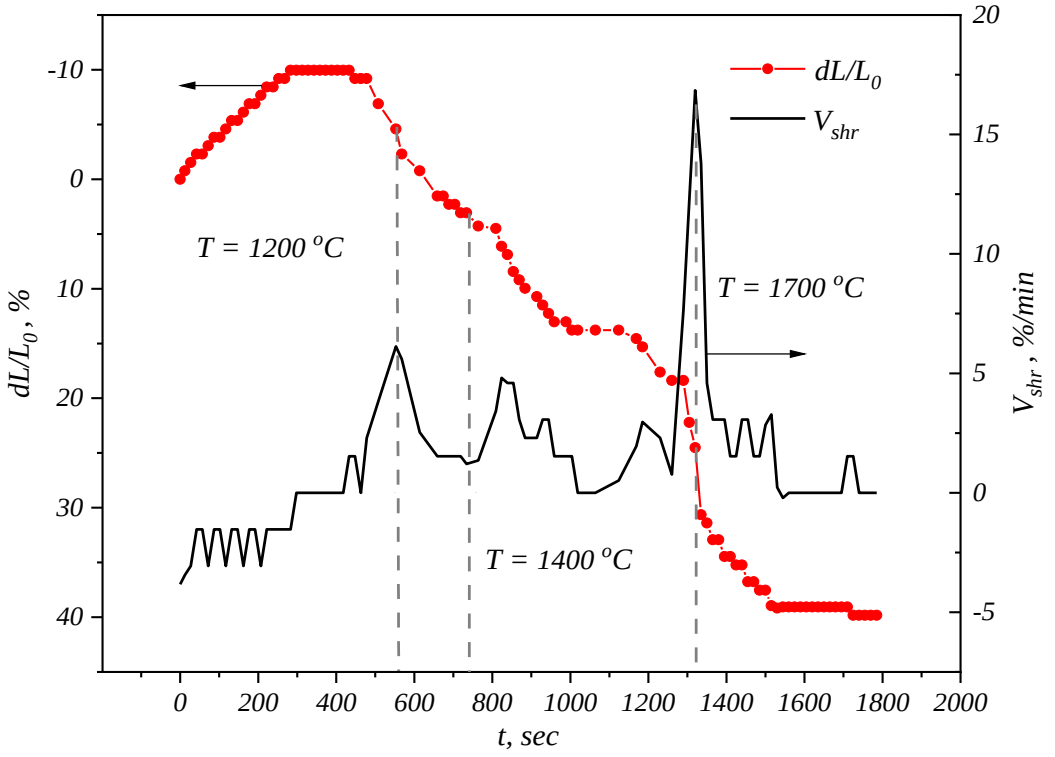

Figure 2.4 – Time dependencies of the relative linear shrinkage dL/L_0 and its speed V_{shr} (sample As15-7)

According to M. F. Ashby and R. A. Ferrell, the shrinkage of a powder material goes with a progressive breakage of the neighbouring particles and is accompanied by gliding adjacent grains with their further adjustment to the neighbouring grains due to the diffusion mechanisms of current.

Non-linearity at the initial stage of shrinkage shows, primarily, the breakage of agglomerates of nanoscale SiC particles. Evidently, these agglomerates will fill the hollows formed with triple joints of bigger particles. At the same time, a progressive rise of temperature and external pressure applied lead to plastic deformation of pore-forming particles and, consequently, to a decrease of porosity in the agglomerates. Such shrinkage behavior was observed when the temperature reached about 1400…1450 °C. The change in the curve slope (fig. 2.3) shows that further shrinkage runs faster.

Application of additives in the form of micro-disperse powders eliminated such anomalies during compaction (fig. 2.5) and the shrinkage speed at the initial stage did not change. The maximum shrinkage speed with application of the micro-micro mixture is about 4 %/min, with the micro-nano mixture it reaches 25 %/min. It can be explained by higher mobility of nanoparticles and relative ease of their re-grouping.

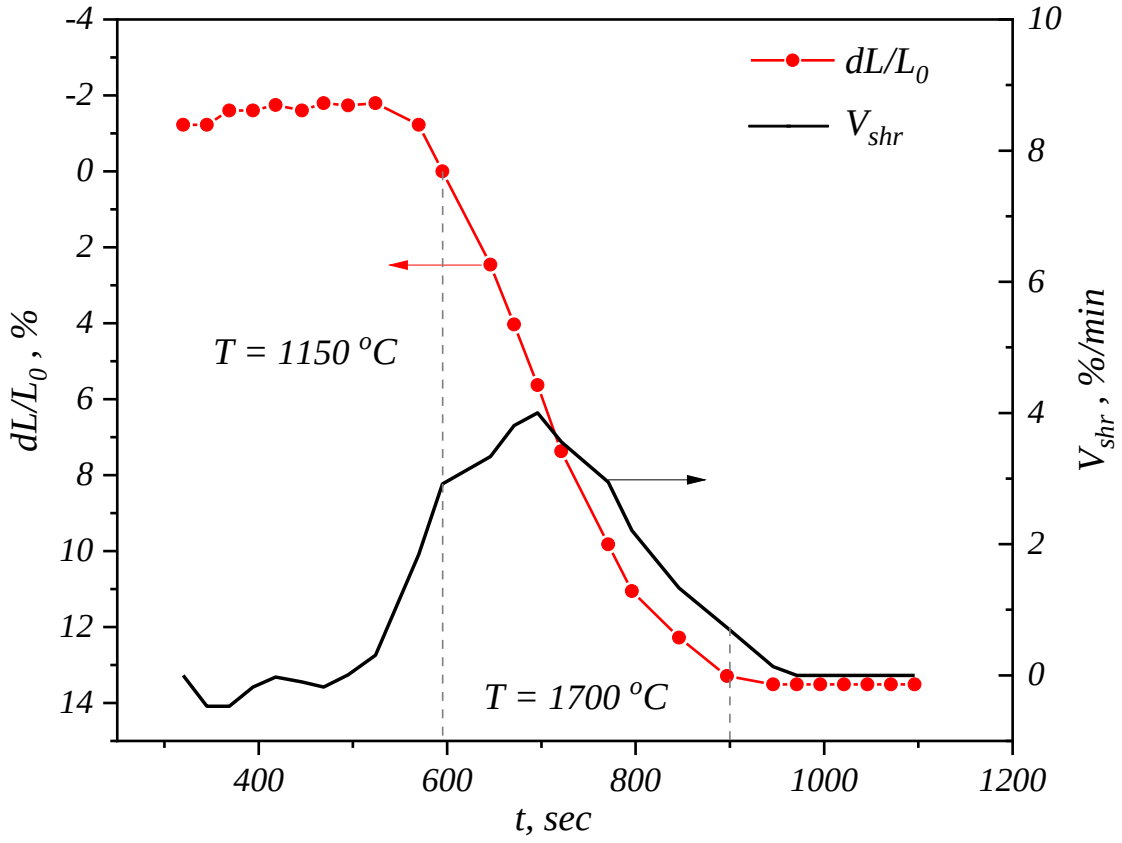

Figure 2.5 – Time dependencies of the relative linear shrinkage dL/L_0 and its speed V_{shr} (sample As15-7)

The first dotted line (fig. 2.3…2.5) indicates the beginning of shrinkage. Each marker shows the temperature at particular time. The last dotted line corresponds to the time when the axial pressure attained the working pressure (35 MPa).

The shrinkage curves and shrinkage speeds on fig. 2.3…2.4 do not differ principally, the beginning of shrinkage can be observed at the temperature 1150…1200 °C. The shrinkage pattern of a sample of micro-micro mixture (fig. 2.5) is simpler, but, at the same time, one can observe lower values of the compaction speed, which proves that application of additives as nanopowders is advantageous.

2.1.2. Modelling and approximation

The intermediate compaction stage initiates the compaction mechanisms that is characterized by rapid grain growth, shrinkage and rise in the material density up to ~ 90 % out of the theoretical density. The two-spherical Frenkel model is based on the frictional atom flow notion which links the vacancy diffusion coefficient D_v, the volume of vacancies (or an atom) Ω and the vacancy concentration gradient per square unit of the material (dC_v/dx), as presented in equation [112]:

$$Y = \frac{D_v}{\Omega} \cdot \frac{dC_v}{dx}. \tag{2.1}$$

Thus, the time dependency of the volume transfer can have the following form

$$\frac{dV}{dt} = Y \cdot S_{gb} \cdot \Omega, \tag{2.2}$$

where S_{gb} – cross-section area involved in the diffusion.

By assuming that a less reduction of the surface energy of the system is equivalent to the energy scattering with the mass flow, we can obtain some equations connecting the neck radius and the particle radius according to the sintering time [113]:

$$\left(\frac{X}{a}\right)^m = \frac{H}{a^n} \cdot t, \tag{2.3}$$

where m and n – set by the sintering mechanism; H – function depending on such parameters as diffusion speed, surface tension, size of vacancies or an atom; a – sphere radius.

There are a lot of characteristics that can be determined from the kinetic equations; among them are speed, density, sintering and activation mechanisms. The sintering mechanisms at the initial stage can be estimated with the Coble equation based on the two-spherical Frenkel model [114]:

$$y^n = A \cdot \exp\left(\frac{-Q}{R \cdot T}\right) \cdot t, \tag{2.4}$$

where n – parameter indicating the predominant mechanism of frictional flow, surface diffusion, grain boundary and crystalline lattice diffusion, n = 1, 2, 3 or 4; y – linear shrinkage of the sample; Q – activation energy; R – universal gas constant; T – absolute temperature; t – time.

This model was used for approximation of the time linear shrinkage dependency at the final sintering stage in the electric consolidation unit. As far as the temperature was constant the thermo-activation exponential factor can be neglected.

Fig. 2.6 shows the results of approximation (for the As15-7 sample) at various values of n. The approximation at n = 3 turned out to be the most precise and it testified that the grain boundary diffusion was predominant; the adjusted determination coefficient ($Adj.R^2$) equaled 0.94.

During isothermal sintering the yielding capacity of the material decreases if a heating time increases. It is explained by restoration of distortions in the crystalline lattice. Therefore, higher yielding capacity of a powder body at the beginning of sintering is conditioned by a high concentration of defects in this body, and their restoration speeds up the diffusion; the concentration of defects gradually drops.

Consequently, the points in a period of 1300…1350 s can be approximated if n = 1. Here, the total $Adj.R^2$ equals 0.96 (fig. 2.7).

It means that the beginning of pressing is characterized by a predominant frictional flow with the constant speed changed by the mass transfer mechanisms with the grain boundary diffusion.

The final stage is characterized by activation of the grain growth and mass transfer through lattice diffusion (n = 4). The main contribution to compaction is made by displacements of defects in the crystalline lattice and re-crystallization, and to a lesser extent, by elimination of residual pores.

Fig. 2.8 demonstrates that the shrinkage of the sample sintered at 1600 °C is fully completed unlike that of the sample sintered at 1700 °C in which the re-crystallization processes are active up to the end of sintering.

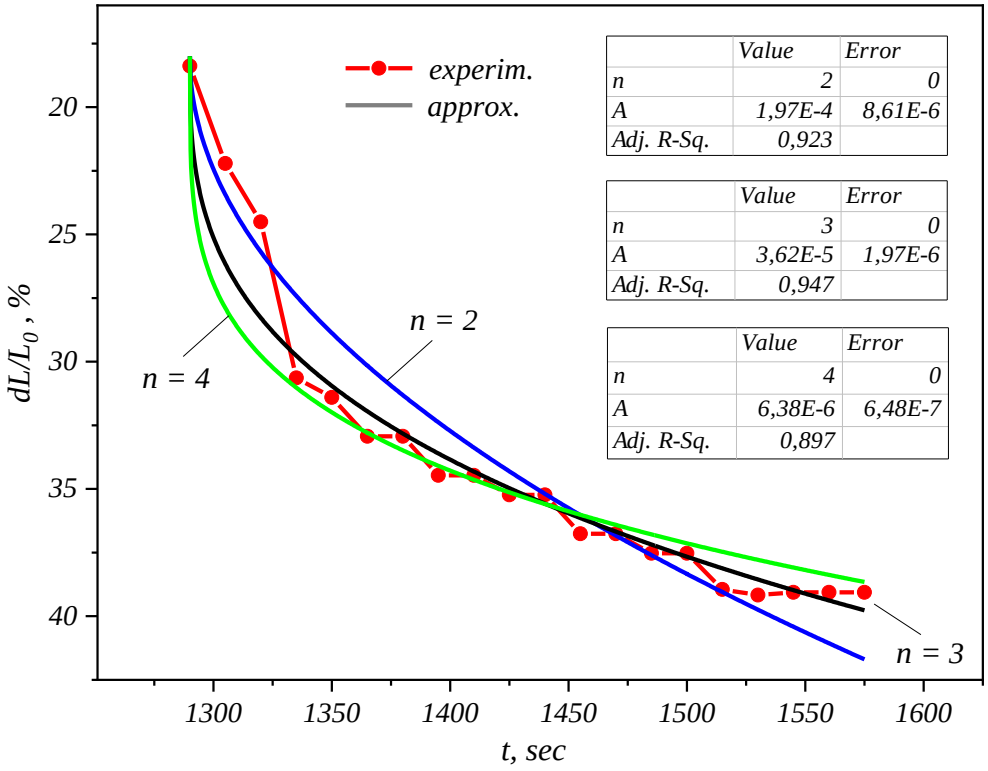

Figure 2.6 – Approximation of the time dependency of a linear shrinkage during compaction (sample As15-7; parameter n = 2...4)

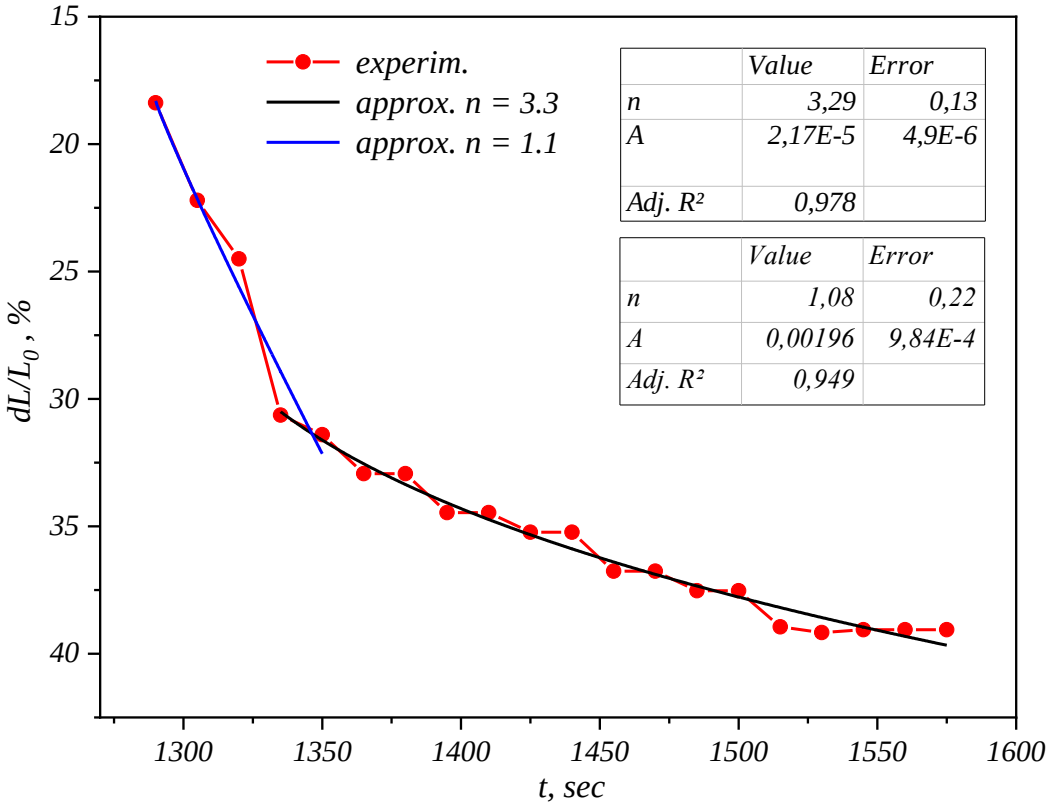

Figure 2.7 – Approximation of the time dependency of a linear shrinkage during compaction (sample As15-7; parameter n = 1.1 and 3.1)

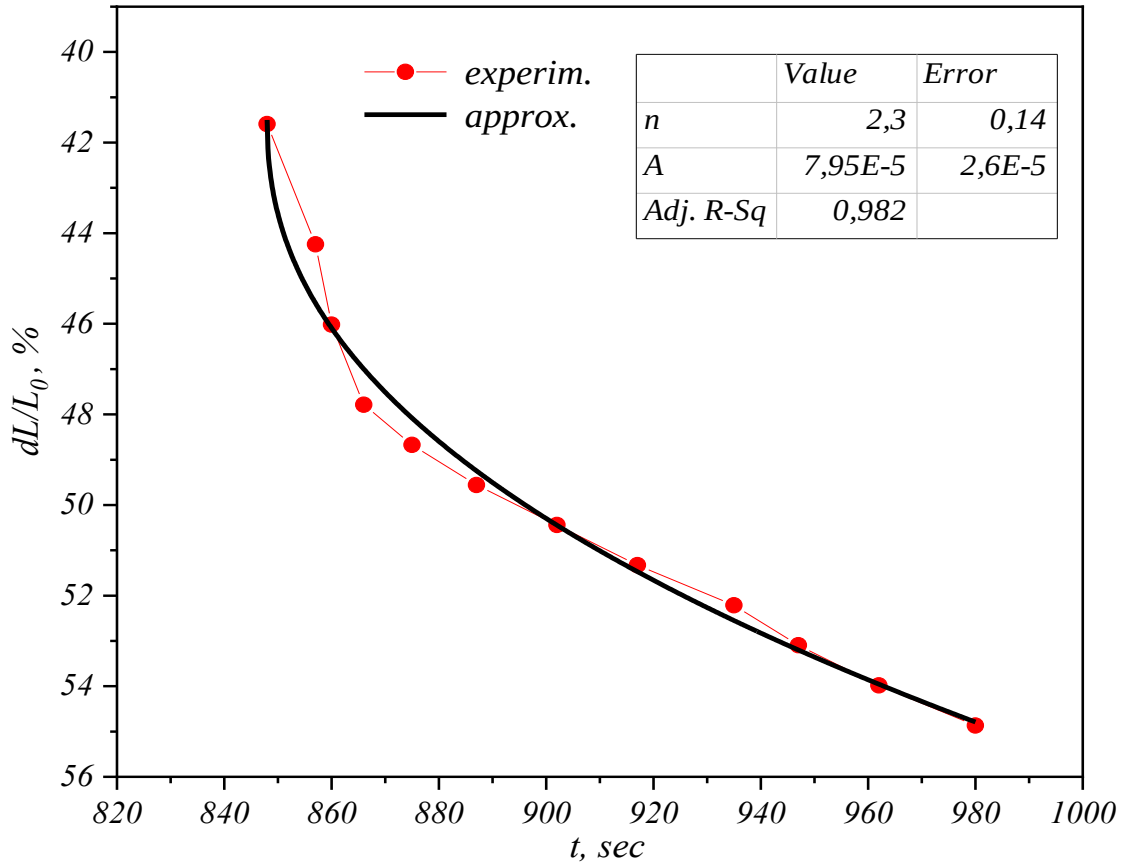

Figure 2.8 – Approximation of the time dependency of a linear shrinkage during compaction (sample As15-6; parameter n = 2.3)

Thus, the analysis of a linear shrinkage during sintering reveals the compaction mechanisms; this can be used for determination of the optimal consolidation parameters and further estimation of the quality of the materials obtained.

2.2. Effect of electroconsolidation on the material properties

2.2.1. Phase composition of primary powders

The X-ray analysis of the powders revealed the clearly marked 3C-modification phase (cubical) and presence of small amount of the 6H-modification phase (hexagonal). These silicon carbide modifications have the same density and small differences in physical properties [115].

The Raman spectrometry also demonstrated predominance of the phase of cubical SiC with transverse and longitudinal modes and presence of small amount of the 6H-SiC phase. The free carbon C was also in the composition. The analysis of the nano-SiC type powder shows that the average size of a SiC crystal is about 100 nm. The dominant SiC phase is the cubic 3C phase (fig. 2.9).

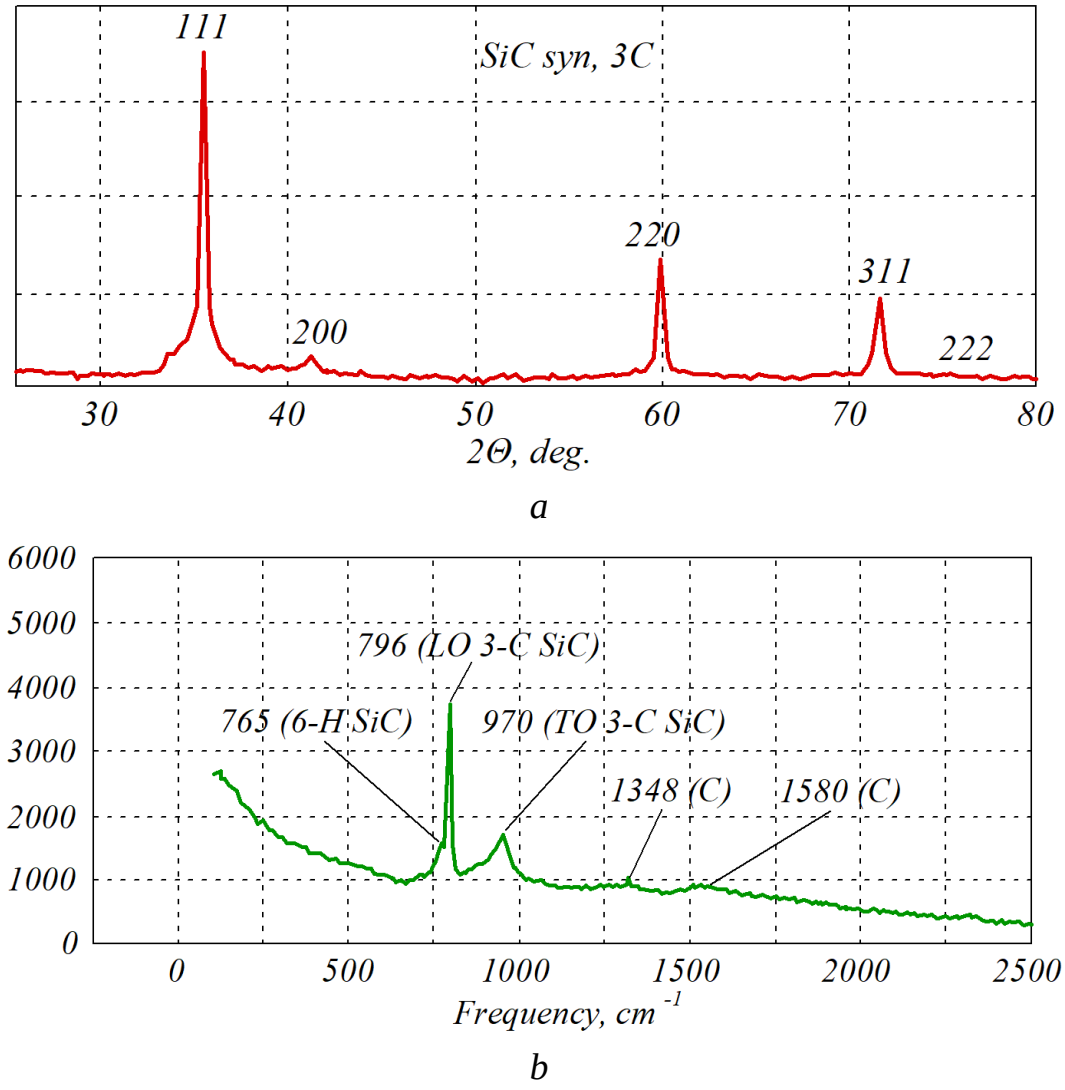

Figure 2.9 – XRD pattern (*a*) and Raman spectrum (*b*) of a nano-SiC powder

The analysis of X-rays and spectra of the combined scattering indicates the presence of insignificant amount of the phase of hexagonal 6H-SiC carbon polytype. This nano-SiC powder and nano (submicron) powder Al_2O_3 were used for fabricating batches for further compaction by means of electroconsolidation.

According to the results of the X-ray analysis batch № 1 (table 2.2) consisted of the mixture of Al_2O_3 with the lattice parameters a = 4.760 Å; c = 12.993 Å and SiC-3C with the lattice parameter a = 4.359 Å. The coherent scattering regions were practically equal and amounted to 82.7 nm and 87.7 nm, respectively. Both Al_2O_3 and SiC were nano-structured. Batch № 2 consisted of Al_2O_3 with the parameters a = 4.760 Å; c = 12.991 Å and SiC-6H with the lattice parameters a = 3.083 Å; c = 15.110 Å. The coherent scattering region equaled 201.5 nm and 68.6 nm, respectively. The X-ray diffraction patterns of the Al_2O_3–SiC mixtures are given in fig. 2.10.

Table 2.2 – Parameters of Al_2O_3–SiC powder mixtures

Composition №	Phase	% mass	Lattice parameters, Å	Coherent scattering region *D*, nm	*ε*	Samples
1	Al_2O_3	85.6	a = 4.760; c = 12.993	82.7	$1.0 \cdot 10^{-4}$	asx-y
	SiC-3C	14.4	a = 4.359	87.7	$< 10^{-4}$	
2	Al_2O_3	85.4	a = 4.760; c = 12.991	201.5	$3.4 \cdot 10^{-4}$	Asx-y
	SiC-6H	14.6	a = 3.083; c = 15.110	68.6	$1.85 \cdot 10^{-3}$	

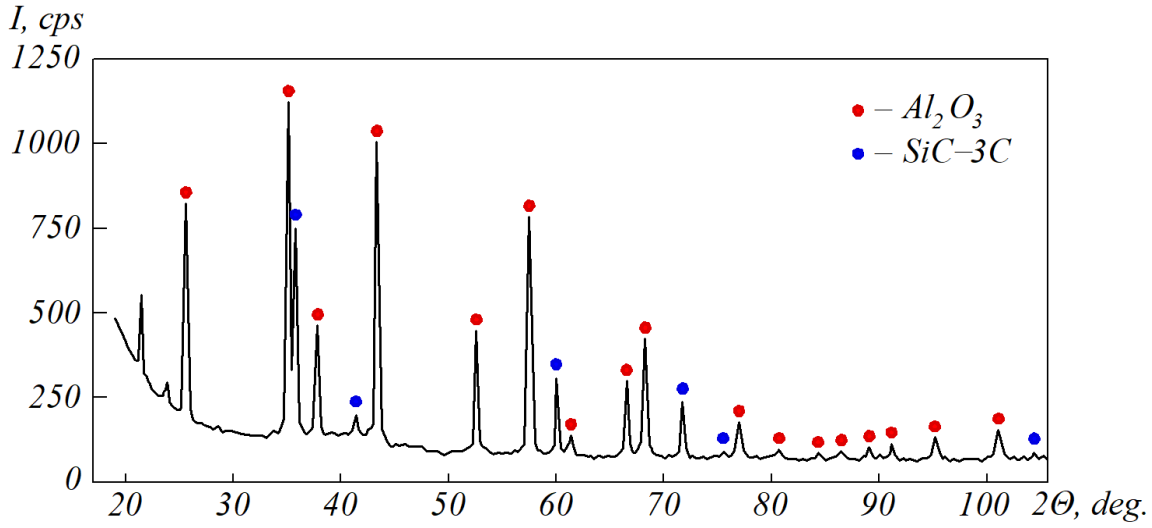

a

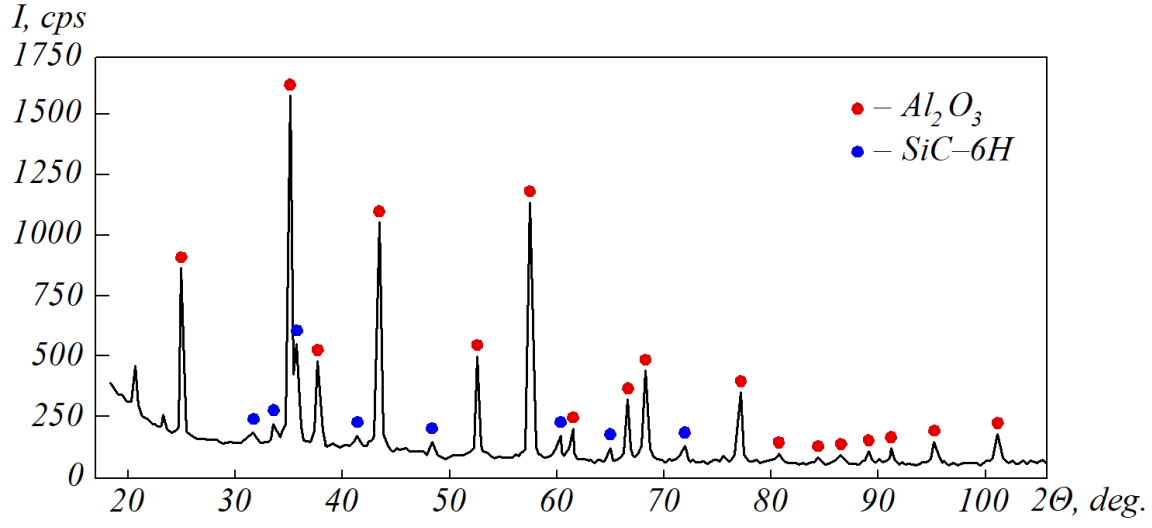

b

Figure 2.10 – X-Ray diffraction patterns of the powders with compositions № 1 (*a*) and № 2 (*b*)

The X-ray diffraction patterns (fig. 2.10) have additional lines from Vaseline used for connection of the powders, however it did not change the line width.

2.2.2. Effect of consolidation temperature on the phase composition

The results of X-ray study into asx-y samples are presented in fig. 2.11 and in table 2.3. The results of the X-ray shows that consolidation of nanopowders at the temperature T_{sint} = 1600 °C does not change their phase composition. The as80-6 sample consists of Al_2O_3 and various SiC modifications: 3C (cubic), H (hexagonal) and SiC-IV (Si_7C_7).

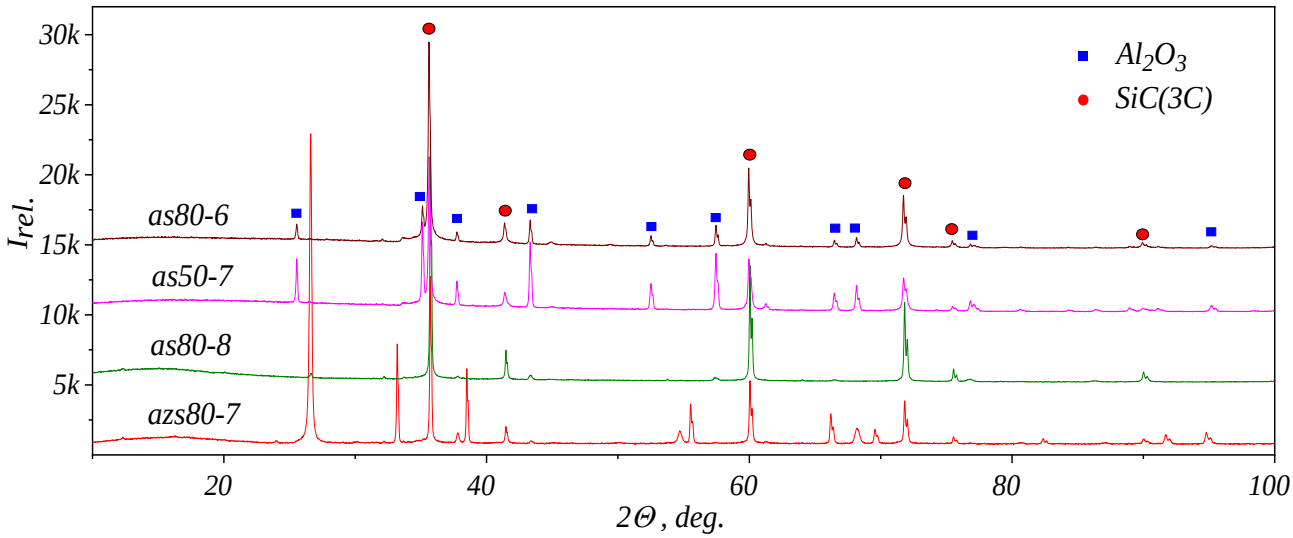

Figure 2.11 – X-ray diffraction pattern of the ceramic samples based on SiC with Al_2O_3 and ZrO_2 additives

Table 2.3 – Phase composition of the samples after electroconsolidation

Phase	Formula	Space group	Sample			
			as80-6	as50-7	as80-8	azs80-7
Moissanite (3C)	SiC	216: F-43m	●	●	●	●
Corund	Al_2O_3	167: R-3c, hex-l	●	●	●	●
Moissanite (H)	CSi	186: P63mc	●	●		
SiC-IV	C_7Si_7	160: R3m, hex-l	●	●		
Silimanite	Al_2O_5Si	62: Pbnm			●	●
ZrC	CZr	225: Fm-3m				●

In a sample with similar composition a rise in sintering temperature up to 1800 °C can initiate the phase of sillimanite $(Al_2O_3)(SiO_2)$ with low hardness and

density (sample as80-8), which negatively impacts the mechanical properties of the finished product. At this temperature it is highly undesirable that sintering time does not exceed several minutes, because, according to research [116], sillimanite sustains intra-structural re-grouping and de-composition into mullite, which is accompanied by an increase of volume by 7.2 % and a decrease in density up to 3.02 g/cm^3.

It has been found that dioxide zirconium in the initial composition decreases the sillimanite formation temperature up to 1700 °C, and the total ZrO_2 (≈ 10 % mass) disintegrates and forms ZrC:

$$SiC+ZrO_2+Al_2O_3 \xrightarrow{T = 1700\ ^\circ C} Al_2O_5Si+ZrC. \quad (2.5)$$

As known from [117] an Al_2O_3 and ZrO_2 mixture in equal proportions at the temperature 1860 °C forms the liquid phase which facilitates compaction of the base material during consolidation. However, great amount of a liquid-phase activator can lead to a porosity increase through its displacement from the volume being compacted. Fig. 2.12, *a* demonstrates the ceramic structure (composition of the azs80-7 sample), pressed at a temperature of 1860 °C and a hold time of 4 min; fig. 2.12, *b* gives the marks of the liquid phase on the press mold parts.

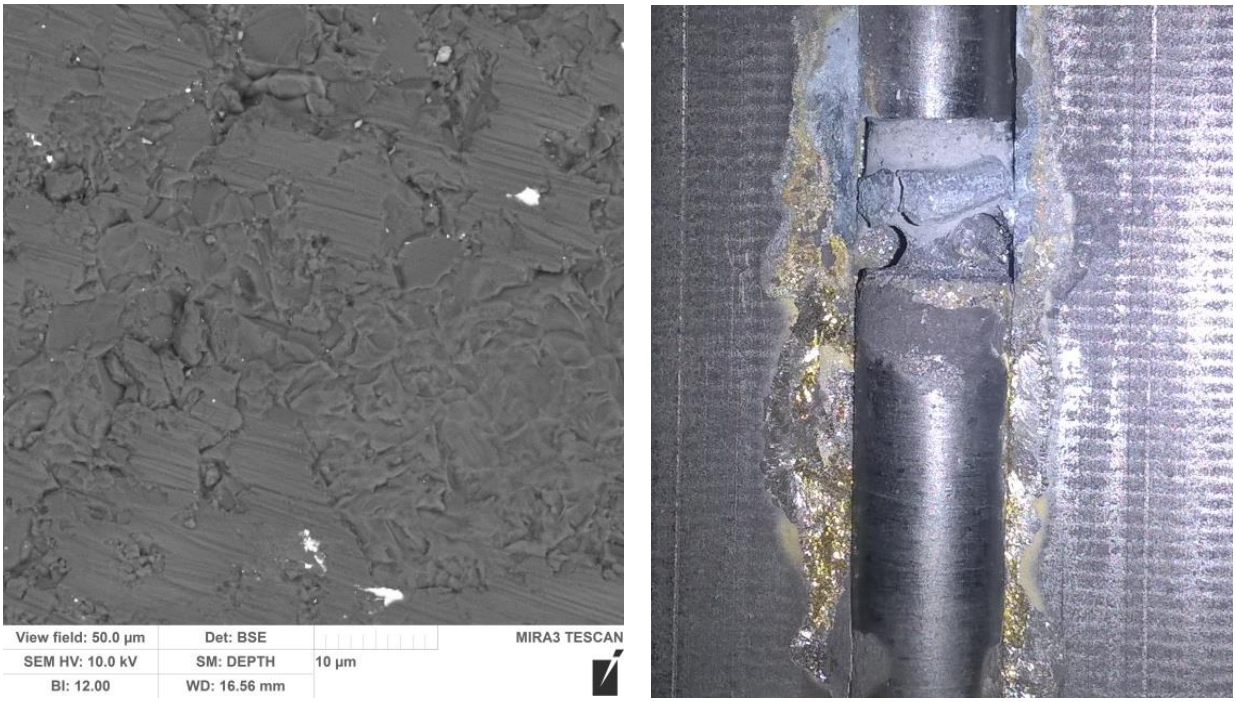

a *b*

Figure 2.12 – Structure of ceramic (ZrO_2 + Al_2O_3) + 80 % SiC, T = 1860 °C, τ = 4 min (*a*) and marks of the liquid phase on the press mold parts (*b*)

It is clearly visible that they are golden metalscent, which, most likely, indicates the presence of nitride zirconium ZrN formed during the reaction [118]:

$$2ZrC+N_2 \xrightarrow{\geq 1100\ ^\circ C} 2ZrN+2C. \qquad (2.6)$$

Despite the data presented in the above-mentioned literature showing that the eutectics Al_2O_3–ZrO_2 has the melting temperature 1860 °C, if nanopowders of these oxides are used (50 nm), the liquid phase can be observed during pressing even at the temperature 1700 °C (sample azs80-7). Obviously, it can be explained by high chemical activity of nano-disperse materials in comparison to micro-disperse ones. A higher sintering temperature always leads to activation of undesirable processes, particularly, chemical reactions with extraction of the gas phase (for the mixtures Al_2O_3–SiC it is SiO, Al_2O, CO), which can considerably decrease the material density [119]:

$$2Al_2O_3+9C \xrightarrow{1800\ ^\circ C} Al_4C_3+6CO\uparrow. \qquad (2.7)$$

The sample As15-7 made of mixture № 2 at a sintering temperature of 1700 °C and a hold time of 4 min consists of 82.8 % Al_2O_3 and 13.3 % SiC according to the results of the analysis (fig. 2.13).

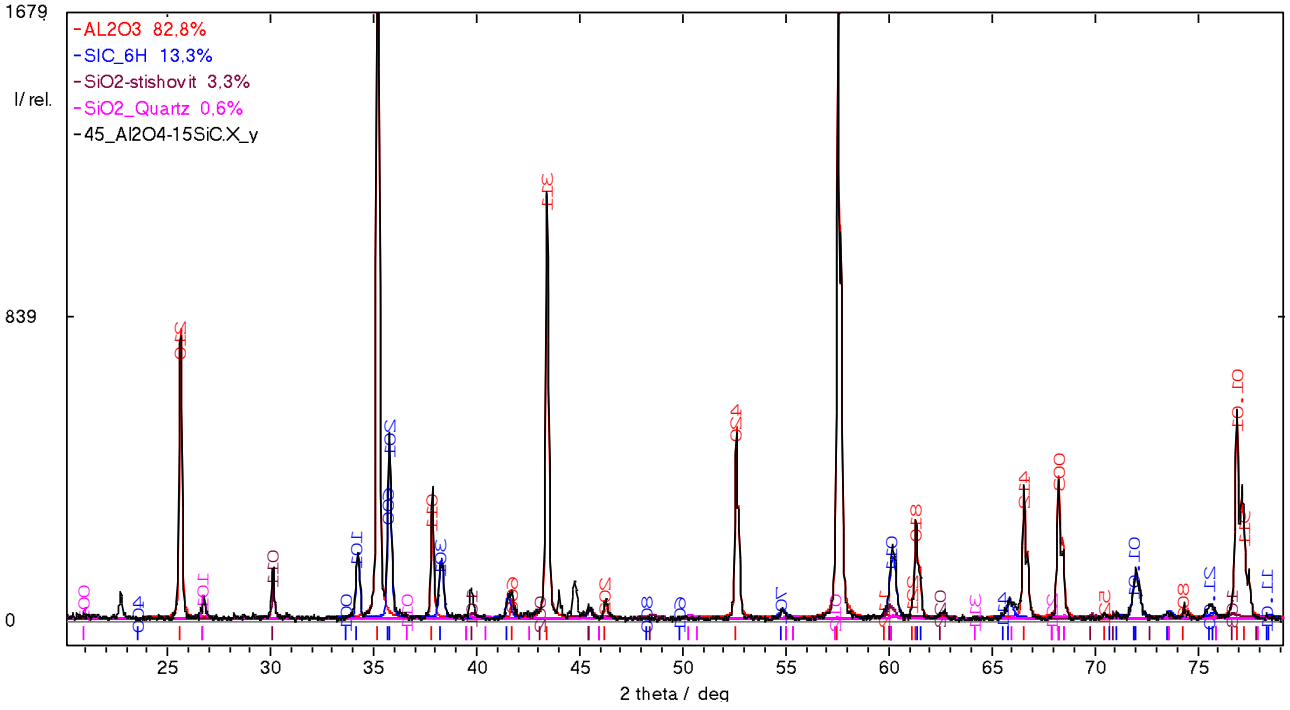

Figure 2.13 – X-ray pattern of the sample As15-7

If compared to the primary composition, the mass part changed as a result of chemical reactions. And after consolidation the sample composition has the SiO_2 phase.

Thus, the advantage of nano-disperse powders in the process of liquid-phase sintering is a lower sintering temperature at which the needed properties are maintained. The higher dispersive capacity of a powder implies more defects in its crystalline lattice and an excess energy reserve. A wider surface layer with the distorted lattice speeds up the surface diffusion and mass transfer. This approach belongs to physical methods used for activation of sintering.

2.2.3. Influence of mixture composition on the ceramic density

The relative density of a composite is calculated on the basis of picnometer calculations and the theoretical density; it equals 3.99 and 3.21 g/cm^3 for Al_2O_3 and SiC, respectively. Fig. 2.14 demonstrates the dependencies of the relative density on the SiC content for Al_2O_3–SiC sintered materials at 1400, 1500, 1600 and 1700 °C, respectively. It is found that at each sintering temperature under study the density of sintered materials changes abruptly when the SiC content in the composites increases.

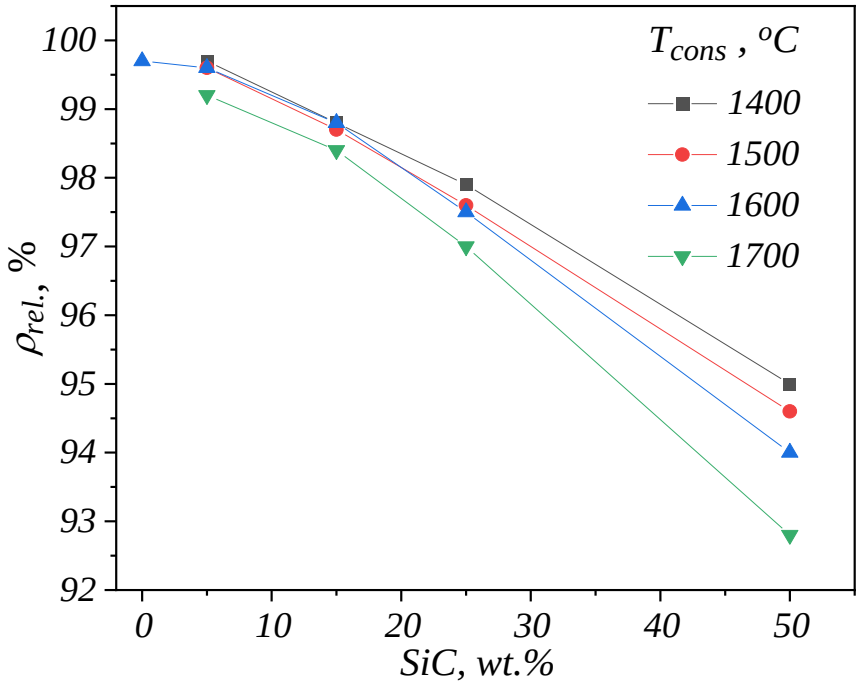

Figure 2.14 – Relative density of Al_2O_3 composites according to the SiC content and the sintering temperature

It can be explained by the fact that a greater number of SiC particles and their agglomerates can be considerably retarding for the compaction mechanism and, thus,

prevent the motion of grain boundaries. However, it should be noted that for the porosity at which compaction is poor, a rise in the temperature would reduce the porosity, however it will not work for Al_2O_3 + 25 % SiC and Al_2O_3 + 50 % SiC composites. It testifies that lower densities are also the result of the carbon presence or formation of glass-like phases with lower density.

The X-ray analysis of the sample As15-7 after compaction (fig. 2.14) shows the presence of SiO_2 that can cause higher porosity inside the composites due to decomposition described by the following reaction:

$$SiC+2SiO_2 \rightarrow 3SiO\uparrow +CO\uparrow, \qquad (2.8)$$

which can cause lower density of the composite sintered at temperatures higher than 1600 °C.

Fig. 2.14 demonstrates the relative density of Al_2O_3 composites according to the SiC content and the sintering temperature. It can be observed that at each sintering temperature under study the density of sintered materials changes abruptly with an increase of the SiC content in the composites. It can be explained by the fact that a greater number of SiC particles can be considerably retarding for the compaction mechanisms and prevent the motion of grain boundaries. When the temperature rises, SiC slows down compaction as indicated by the curve slopes. Besides, the presence of the SiO_2 glass-phase can cause the gas formation, which, if the pores are closed substantially, decreases the material compactibility.

2.2.4. Influence of the dispersive capacity of additives and the isometric hold time on the grain growth in a matrix

As know, during sintering the grain growth accelerates with an increase of temperature and hold time. During compaction of ceramic of pure Al_2O_3 without any additives at the temperatures 1600…1700 °C the average grain size is about 20 mkm (fig. 2.15, *a*), which is rather large.

The growth of grains can be slowed down through decreasing the sintering temperature and shortening the hold time; but it leads to poor sintering of particles due to the non-complete grain boundary diffusion. With an increase of SiC particles in the primary mixture, the average grain size decreases. The presence of the particles of additives (SiC) prevents the grain growth without a drop of the sintering temperature and the hold time. Fig. 2.15, *b* demonstrates that SiC added to Al_2O_3 maintains the composite microstructure. With application of micro-SiC the grain size is about 3 mkm at a sintering temperature of 1400 °C.

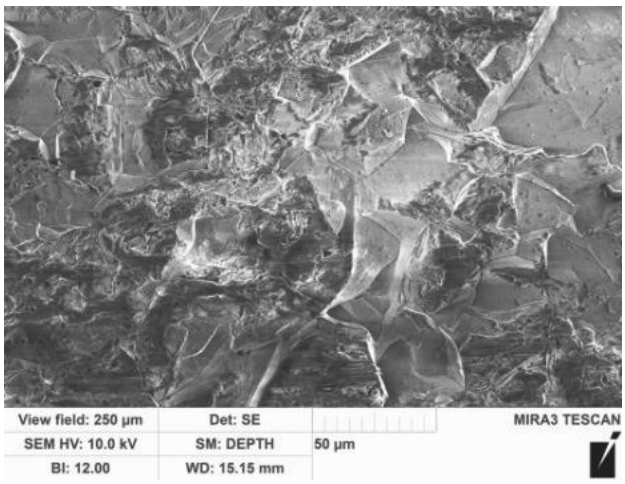

a

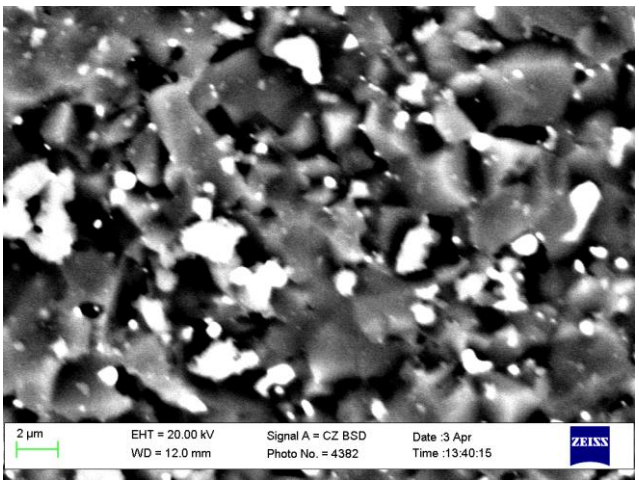

b

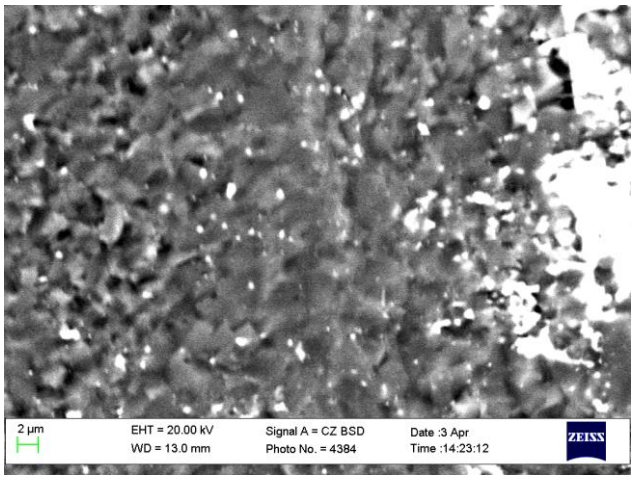

c

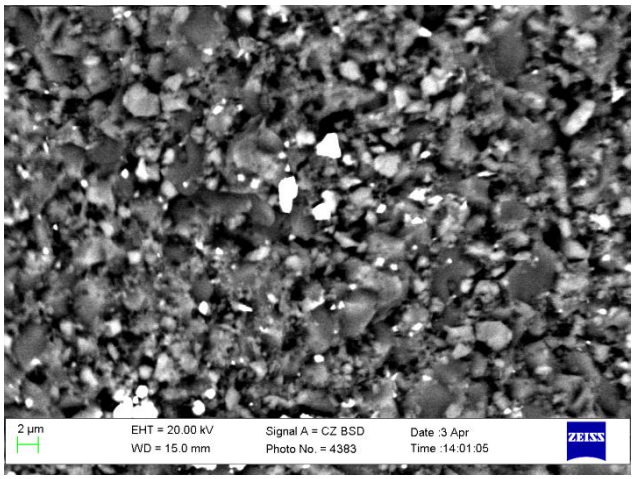

d

Figure 2.15 – Microstructure of Al_2O_3 composites:
a – sample AS0-6; *b* – sample AS15-4; *c* – sample As15-4; *d* – sample As15-7

Taking into account the form of the primary powders, it is possible to conclude that the growth of grains can be effectively slowed down if the number of reinforced particles is three times as many as the number of particles in the matrix. This can be attained either by increasing the SiC mass content in the composite to rather high values or by applying fine SiC powders.

As seen in fig. 2.15, *c*, *d* when nano-disperse SiC is used, the composite keeps its microstructure even at a temperature of 1700 °C and its grain size is smaller than that of AS15-4 composite.

One of the most important conditions for application of nanopowders is the isothermal hold time that should be several minutes for such highly active materials. Fig. 2.16 demonstrates the structure of two samples of the same composition sintered at different hold times in similar conditions.

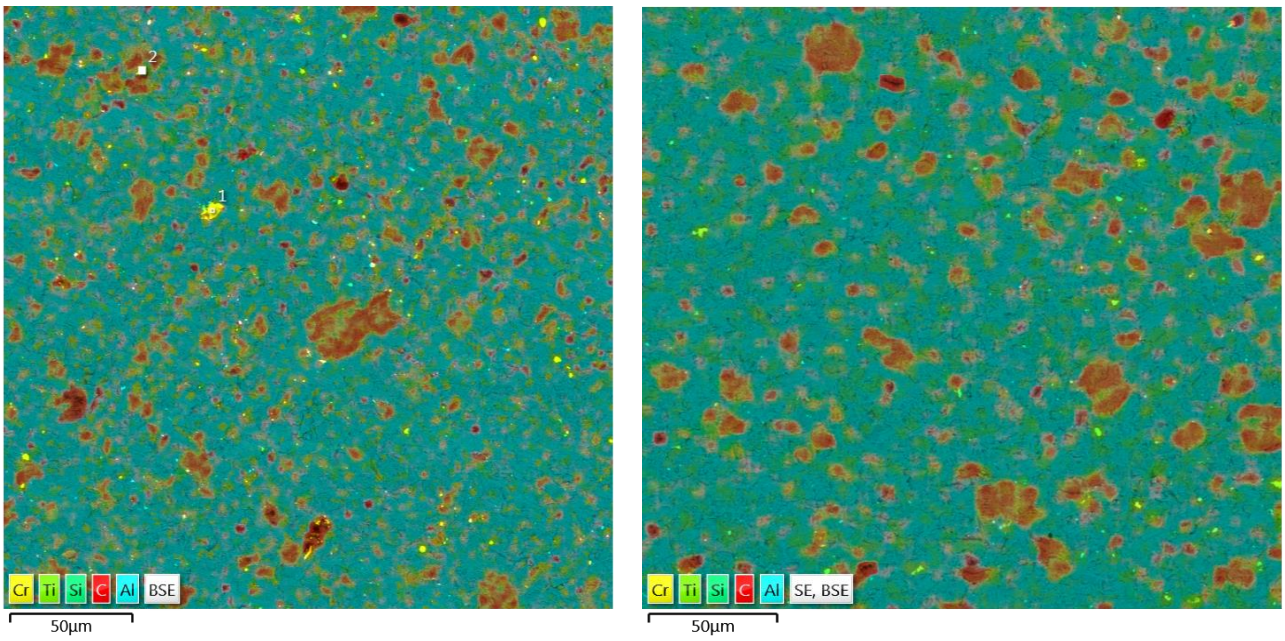

a *b*

Figure 2.16 – Multilayer map of the energy disperse spectroscopy of Al_2O_3–SiC composite:
a – sintering temperature T_{sint} = 1500 °C, hold time t = 3 min;
b – T_{sint} = 1500 °C, t = 10 min

As seen, if the hold time varies from 3 to 10 minutes, the distribution of SiC particles becomes less equilibrium, which worsens the material dispersive capacity.

2.3. Mechanical properties of Al_2O_3–SiC composites (nano)

2.3.1. Micro hardness of Al_2O_3–SiC composite

The porosity considerably impacts the mechanical properties of ceramics. For the sample Al_2O_3 + 15 mass % SiC the flexing strength increases from 500 MPa to 600 MPa with an increase in the sintering temperature from 1600 °C to 1700 °C, which shows better grain boundary diffusion.

Another important factor affecting the strength is the grain size. According to Griffith's theory [120] the strength of ceramics depends on the number of defects, and the number of defects is proportional to the grain size for ceramics, thus a smaller grain size can worsen the strength of polycrystalline materials.

The coarse-grain structure (pure Al_2O_3) implies low flexing strength (250 MPa). The reason for formation of internal defects in pure Al_2O_3 composite, along with its coarse-grain structure, can also be explained be the heat expansion anisotropy of a

matrix grain [121]. Therefore, the composite strength grows with a decrease of the size of the grain matrix by adding SiC, and considerably decreases with an increase in the sintering temperature due to rapid grain growth.

The same is true about the hardness (fig. 2.17), its value rises if SiC is added, but at reaching some value the concentration of an additive begins to decrease.

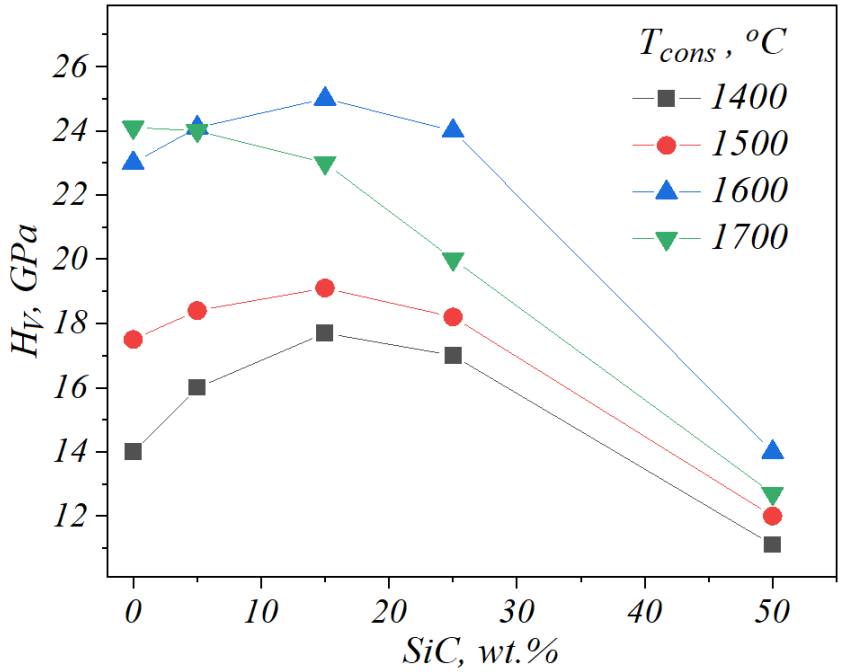

Figure 2.17 – Micro-hardness H_V of samples of Al_2O_3 ceramic according to the SiC content and the sintering temperature

The sample with the highest hardness was obtained through sintering Al_2O_3 + 15 mass % SiC composition at the temperature T = 1600 °C and the hold time t = 3 min.

As far as the micro-hardness is conditioned by a number of physical characteristics of a substance (interatomic interaction power, level of co-valence, interatomic distances), the distribution of micro-hardness values by the diameter of the sample will characterize homogeneity of the properties in the consolidated sample, quality of sintering, and equilibrium of the density distribution.

The last condition characterizes the service life of ceramic products if they are used as instrumental and construction materials.

The distribution of micro-hardness by the diameter of the sample was studied and the results are presented in fig. 2.18.

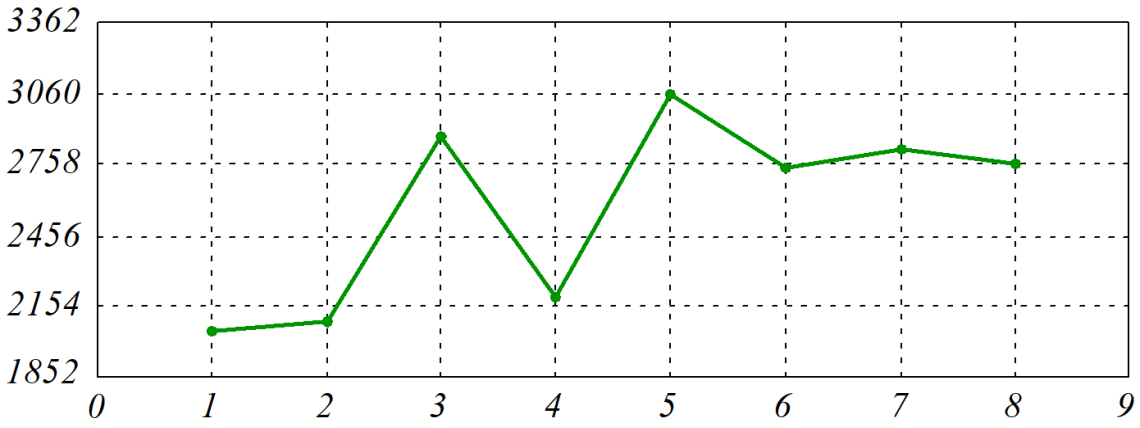

Figure 2.18 – Distribution of the micro-hardness H_V by the diameter of the sample Al_2O_3–15 mass % SiC fabricated at the temperature 1600 °C

The mean square difference of the micro-hardness value by the diameter was 14 %.

2.3.2. Crack resistance of Al_2O_3–SiC composites

Apart from porosity and grain size another important factor affecting the mechanical properties is the residual stress conditioned by inconsistency of the thermal expansion coefficient (TEC) between the Al_2O_3 matrix and the SiC particles. The average TEC of Al_2O_3 ($\approx 9 \cdot 10^{-6}$ K^{-1}) is approximately two times exceeds the average value for SiC ($\approx 4.5 \cdot 10^{-6}$ K^{-1}) [122, 123].

Therefore, the Al_2O_3 matrix is under the tension stress after cooling to the room temperature [124]. Obviously, the value of residual stress increases with an increase of the SiC amount, and higher tension stresses on the grain boundary can result in a transcrystalline crack. Therefore, the type of fracture can change from a completely transcrystalline break for pure Al_2O_3 to an intercrystallite fracture for composites with great amount of SiC (fig. 2.19).

For the intercryatalline fracture there is a stronger dependency of the crack resistance on the grain size, than that for the transcrystalline fracture because more grains get into the area of plastic deformation at the crack apex.

In any case microcracks can appear on the surface of Al_2O_3–SiC due to interphase compressive stresses, thus increasing the fracture energy and, consequently, improving the mechanical properties.

Fig. 2.20 demonstrates the value of crack resistance K_{IC} of the samples Al_2O_3 + x % SiC (x = 0, 5, 15, 25, 50) sintered at various temperatures. We can see that the crack resistance of the samples grows with an increase of the SiC content (to the value 15 mass %), and later on it decreases with its content.

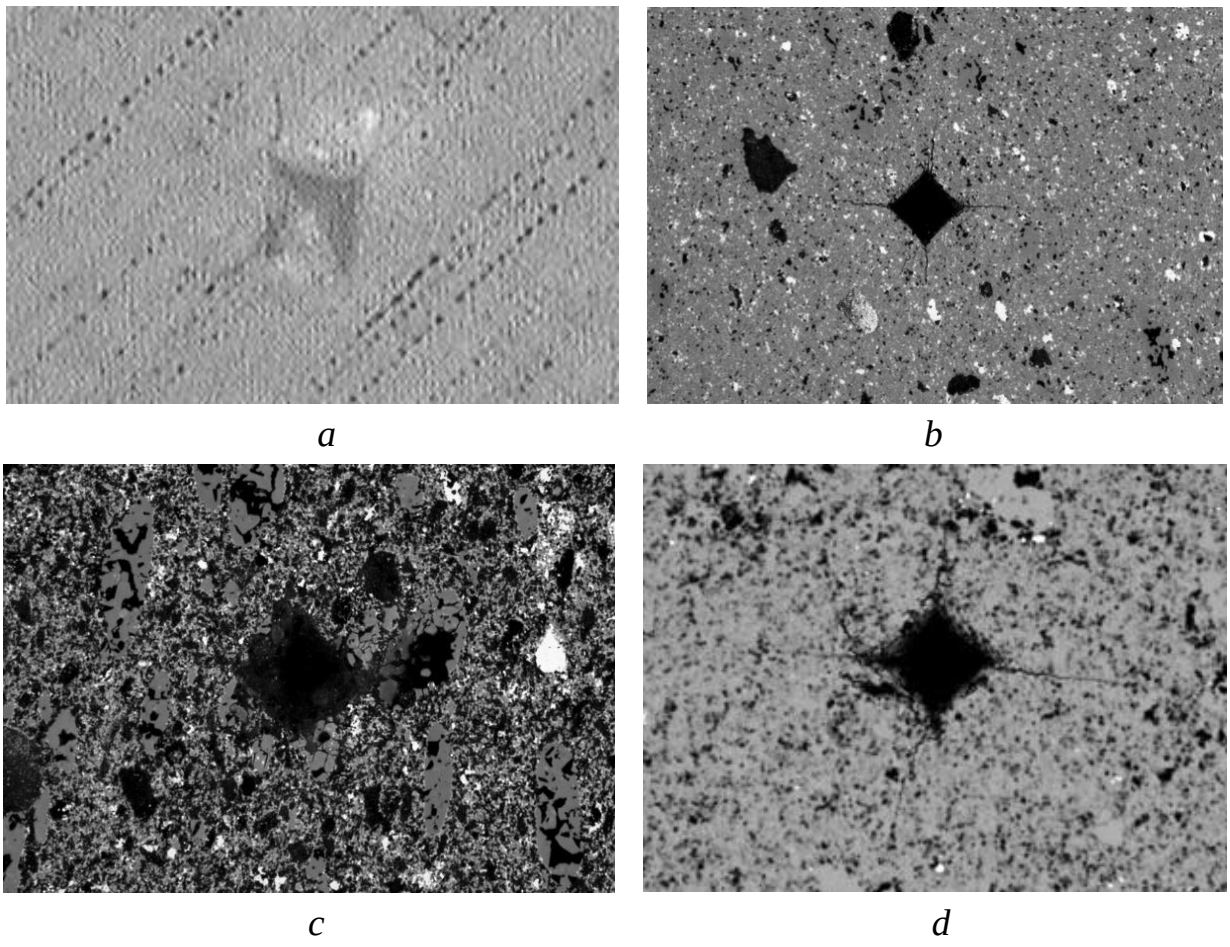

Figure 2.19 – Surface of the samples of Al_2O_3 ceramic after indentation: *a* – sample AS0-6; *b* – sample as10-5; *c* – sample as50-6; *d* – sample as80-6

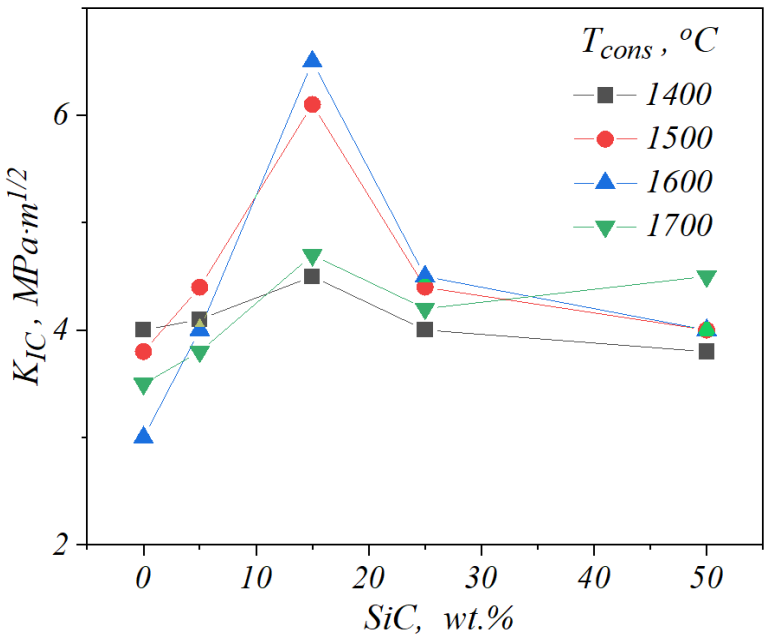

Figure 2.20 – Crack resistance K_{IC} of the samples of Al_2O_3 ceramic according to the SiC content and the sintering temperature

On the surface of the sample AS0-6 (fig. 2.19, *a*) we can clearly see the crack deflection and its zigzag-like form, and if 10 % SiC (sample as10-5) is added, the cracks do not change their direction and they become straight.

A larger grain size improves the crack resistance, which is explained by the bypassing effect in a polycrystalline material [125]. With small amount of SiC added, the fracture viscosity of the samples improves due to intensification of the SiC effect – crack formation or crack deflection. As seen from fig. 2.20 the crack resistance of the composite reaches the maximum value with the amount of SiC 15 mass %. And its higher concentration reduces its crack resistance because the grain size becomes very small.

It is not easy to achieve the high strength and high impact viscosity in one sample, but application of nanodisperse SiC powders and the electroconsolidation technology made it possible to fabricate the composite material with the micro-hardness H_V = 25 GPa and the crack resistance K_{IC} = 6.5 MPa·m$^{1/2}$, which is higher than those of the existing analogues.

2.4. Design of the complete factorial experiment

In ceramic composites, particularly in the Al_2O_3–SiC system, microstructure is of primary importance because of its mechanical properties. It can be changed with the amount of additive, as well as the consolidation temperature. The character and the impact level of these parameters are essential for development of the optimal mode of sintering for the phase composition. Therefore, finding the dependency between the temperature of electroconsolidation for nano-scale oxide powders and the properties of the composite obtained is a very important task.

This task was solved with the research into an impact of the consolidation temperature of nano-powders of alumina and silicon carbide and the amount of SiC on the stress intensity coefficient of the obtained composite ceramic by means of the statistical method for planning the complete factorial experiment [126].

The research into the technological process of electroconsolidation of nano-powders of the Al_2O_3–SiC system uses the critical stress intensity factor K_{IC} as the design and engineering optimization parameter *Y*, the amount of SiC, mass % – as the factors x_1; and x_2 – the consolidation temperature, °C. The lower and upper levels of the factors are determined according to the results of theoretical research and search experiments. The results of coding and selection of the variability intervals are given in table 2.4.

Table 2.4 – Coding of factors and their variability intervals

Factor	Value	
	x_1	x_2
	Amount of SiC, mass %	Consolidation temperature T, °C
Basic level	7.5	1500
Variability interval	7.5	100
Upper level of the factor	15	1600
Lower level of the factor	0	1400
Response function	Y – stress intensity factor K_{IC}	

With the average confidence probability $p = 0.95$ and a limit of error, the research included a regular duplication of experiments with three parallel tests. The random nature of the research was provided with a gradual increase of the numbers in column four in the random number table. During the planning of the experiment the square effects x_1^2 and x_2^2 were neglected, it was taken into account that the corresponding regression coefficients b_{ij} were close to zero. This assumption was checked by means of an additional experiment close to the center of planning (7.5 mass % and 1500 °C). The result of it was the value $Y_{01} = 4.83$ MPa·m$^{1/2}$. The difference between $\overline{Y}$ (the average value by four tests) and Y_0 is the evaluation for $\sum b_{ii}$.

And in this case they were equal to $\overline{Y} - Y_0 = 4.48 - 4.83 = -0.35$ MPa·m$^{1/2}$, which was less than the experimental error, therefore, the assumption on small values of the coefficients was acceptable. The results of the research were used for compiling the matrix of experiment planning (table 2.5).

Table 2.5 – Planning matrix of the multi-factor experiment

Test №	x_0	x_1	x_2	x_1x_2	Y_1	Y_2	Y_3	$\overline{Y}$	S^2
1	1	1	1	1	6.43	6.51	6.50	6.48	0.002
2	1	1	–1	–1	4.31	4.60	4.52	4.48	0.022
3	1	–1	1	–1	3.20	2.82	3.05	3.04	0.037
4	1	–1	–1	1	3.90	4.20	3.88	3.99	0.032

The following characteristics were checked: homogeneity of dispersions, statistic value of the regression and adequacy coefficients of the models. The value of

the Cochran test was $G = 0.40$, and the condition $G < G_{cr}$ was fulfilled, which confirmed the experiment reputability; the error mean square was $S_Y^2 = 0.023$.

The regression coefficients were calculated and the regression equation obtained the form

$$Y = 4.50 + x_1 + 0.25 \cdot x_2 + 0.75 \cdot x_1 \cdot x_2. \quad (2.9)$$

Equation (2.9) shows that K_{IC} considerably depends on the silicon carbide concentration in the initial powder, as the regression coefficient is the highest at x_1. The significance of the regression coefficients obtained by the *t*-test equals 100, 22.2, 5.6 and 16.7 for b_0, b_1, b_2, b_{12}, respectively. The tabular value t_{cr} for the accepted reliability α = 95 % equals t_{cr} = 4.3, and the values t_i obtained are higher than t_{cr}, which confirms the significance of the coefficients selected.

CHAPTER 3

THERMAL-PHISICAL AND THERMAL-MECHANICAL PROPERTIES OF Al_2O_3–SiC NANOCOMPOSITES

3.1. Mechanisms of heat-transfer and scattering

3.1.1. Heat-transfer mechanisms

The heat in solid bodies is transferred by various types of elementary excitations, such as phonons (quants of collective oscillations of ions of the crystalline lattice), electrons, etc. For a simple cubic lattice the heat is distributed by the law

$$\overline{H} = -\lambda \cdot grad(T), \tag{3.1}$$

where $\overline{H}$ – vector, the value of which equals the heat flow; λ – heat conductivity coefficient; T – temperature.

When the heat is transferred by the carrier system, either phonons or electrons, the thermal conductivity coefficient can be estimated by means of the standard gas-kinetic equation

$$\lambda \sim \frac{1}{3} \cdot \rho \cdot C \cdot v \cdot l, \tag{3.2}$$

where ρ – material density; C, l and v – thermal capacity, free path and average velocity of heat carriers, respectively (for corundum $v \approx 8.5 \cdot 10^3$ m/s [127]).

The composite under study is dielectric; therefore, we will consider only phononic thermal conductivity.

When heat is transferred, any elementary disturbances scatter and this leads to dissipation of a heat flow. It occurs during a collision with defects of the crystal lattice, phonons, boundaries, etc. The heat resistance $(W = 1/\lambda)$ follows Mattiessen's rule:

$$W = \sum_{j=1}^{n} W_j. \tag{3.3}$$

For dielectrics in which electrons are involved in neither the heat transfer process nor scattering it has the form

$$W = W_b + W_d + W_p + W_u, \tag{3.4}$$

in which the right part is the sum of thermal (conditioned by the scattering of phonons at the boundaries), dotted, plane defects and those on phonons, respectively [128].

As far as $l = l(\omega) = \tau(\omega)\cdot\upsilon$ (where ω – phonon frequency), ratio (3.2) has the form

$$\lambda = \frac{1}{3}\cdot v^2 \cdot \int_0^{\theta/T} \tau(x)\cdot C(x)\cdot dx, \tag{3.5}$$

where $x = (\hbar\cdot\omega)/(k_B\cdot T)$, ($k_B$ – Boltzmann's constant; $\hbar$ – Plank's constant) and, according to (3.4)

$$\tau = \frac{1}{\tau_b^{-1} + \tau_d^{-1} + \tau_p^{-1} + \tau_u^{-1}}. \tag{3.6}$$

In the nominator of expression (3.6) the first summand describes the scattering on the boundaries of the sample or other structural defects with the size far larger than the length of the wave of the dominant phonons; the second and the third summands describe the scattering on dotted and plane defects, respectively; the forth summand describes the phonon-phonon U-processes [128].

3.1.2. Scattering mechanisms

At low temperatures ($T << \theta$, where θ – the Debye temperature), when exited elements are mainly long-wavelength phonons, the scattering on dotted and linear defects is insignificant, and the heat flow is restricted by the sample surface. Under these conditions the free run length of a phonon is constant and depends on the crosswise size of a given sample. Therefore, in (3.6) the summand corresponding to the relaxation time at the boundary scattering of phonons has the form

$$\tau_b^{-1} = \frac{v}{A_1}, \tag{3.7}$$

where A_1 – coefficient equal to the least size of the sample.

In polycrystals formed of separate grains or other structural compositions divided by the boundaries, the boundary scattering can be observed at higher temperatures and corresponds to the size of these elements.

Non-ideal crystals have defects the size of which is close to the ion size. These defects are called point defects. They are foreign atoms in the nodes or between the nodes, the native atoms displaced from their equilibrium positions, vacancies and/or their complexes. The displacement of the atoms around the defect results in change of interatomic distances leading to scattering. The Rayleigh law for the relaxation time during scattering on the point defects has the form [128]:

$$\tau_d^{-1} = A_2 \cdot \omega^4. \tag{3.8}$$

The coefficient A_2 contains the information on the value of homogeneity, how it differs from the main crystalline lattice in terms of compressibility and density. The coefficient A_2 has the dimension [s^3].

Apart from point defects (zero-dimensional), there also exist one-dimensional and two-dimensional ones. The reverse relaxation time τ^{-1} during scattering on these defects is proportional to ω^3, ω^2, respectively. Among one-dimensional defects are dislocations, which should be taken into account, if the material under study is mechanically treated by forging, fullering, etc. [129].

Two-dimensional defects were described in [130]. In this case the contribution of two-dimensional defects during the relaxation time can be described as

$$\tau_p^{-1} = A_3 \cdot \omega^2, \tag{3.9}$$

where the coefficient A_3 has the dimension [s].

In an ideal dielectric unlimited crystal the final value of thermal conductivity is determined by the photon-photon interaction (umklapp scattering, U-processes). The greatest contribution into thermal resistance is achieved at high temperatures ($T >> \theta$). Here the probability of phonon scattering is proportional to the temperature, and the thermal capacity is constant which gives the dependency $W_u \sim T$.

At low temperatures long wavelength phonons are dominant in the heat transfer processes, and the umklapp scattering freezes out when the temperature drops, and the heat resistance conditioned by them decreases exponentially [131]:

$$W \sim \left(\frac{\theta}{T}\right)^3 \cdot \exp\left(-\frac{\theta}{b \cdot T}\right), \tag{3.10}$$

where b – constant equaling one.

According to this, the expression for the relaxation time during phonon-phonon scattering can be written as follows

$$\tau_u^{-1} = A_4 \cdot \omega^2 \cdot T \cdot \exp\left(\frac{-\theta}{A_5 \cdot T}\right), \tag{3.11}$$

where the coefficient A_4 has the dimension [s/K].

Regarding the additivity of the value $W(T)$ it is possible to evaluate the contribution of each component. Fig. 3.1 demonstrates temperature dependencies of the cumulative thermal sample As15-5 and its components according to expression (3.4).

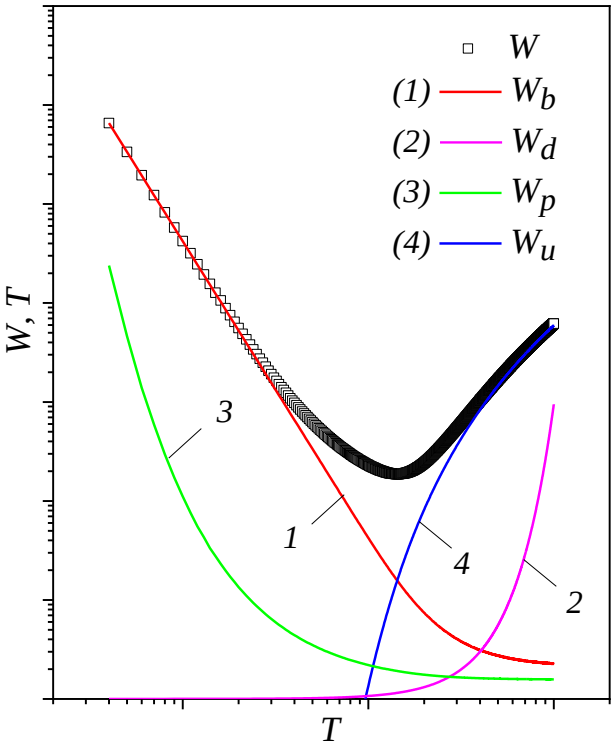

Figure 3.1 – Qualitative dependency of heat resistance in the sample As15-5 on the temperature and contributions of different scattering mechanisms:
1 – boundaries; *2* – point defects; *3* – two-dimensional defects; *4* – phonons

Fig. 3.1 shows that at low temperatures the dominant process is the boundary scattering (curve *1*), and at high temperatures the dominant process is phonon-phonon scattering which leads to the dependency $W \sim T$. In the valley minimum $W(T)$ defect scattering is also of importance. Such behavior of thermal scattering at low temperatures (minimum) is typical for solid bodies without conduction electrons.

3.2. Approximation of the experimental data on thermal conductivity

3.2.1. Mathematical model

Approximation of the experimental data by thermal conductivity was made by means of the Debye model of the phonon spectrum with application of equation (3.5), which, after substitution of the data on heat capacity and with consideration of the Dulong-Petit law, obtained the form

$$\lambda(T) = \frac{k_B}{2 \cdot \pi^2 \cdot v} \cdot \left(\frac{k_B}{\hbar} \right)^3 \cdot T^3 \cdot \int_0^{\theta/T} \tau(x) \cdot \frac{x^4 \cdot e^x}{\left(e^x - 1\right)^2} \cdot dx. \qquad (3.12)$$

The Debye temperature θ for this composition, calculated on the basis of data for Al_2O_3 [132] and the percentage relation of silicon carbide and alumina, was 887 °C. In the element of integration the reverse relaxation time $\tau^{-1}(x)$ is the sum of reverse relaxation times:

$$\tau^{-1}(x) = \frac{v}{A_1} + A_2 \cdot \omega^4 + A_3 \cdot \omega^2 + A_4 \cdot \omega^2 \cdot T \cdot \exp\left(\frac{-\theta}{A_5 \cdot T} \right). \qquad (3.13)$$

For adjustment the coefficients $A_1 \ldots A_5$ varied, and the accuracy was controlled with the corrected determination coefficient $Adj.R^2$, which was the squared multiple correlation coefficient with consideration of the number of independent variables (approximation parameters) and it was no less than 0.996. If this coefficient equals one it implies the zero dispersion.

3.2.2. Results of approximation

Fig. 3.2 and table 3.1 present the results of approximation. Physically the coefficient A_1 is the length of a free run of heat carriers and its value can be compared with the size of a given sample.

The minimum value of this parameter, when the sintering temperature T_{sint} changes, means a finer structure of this ceramic, which is observed at T_{sint} = 1500 °C.

Higher consolidation temperature leads to activation of re-crystallization and grain growth which is confirmed by the higher parameter A_1 for the sample As15-7 and pure oxide ceramic (the data have been taken from literature).

All types of point defects, such as vacancies and additives, distort the crystal lattice and, to a certain degree, influence the physical and mechanical properties. There

appear elastic stress fields near such centers, which give the alloying effect and complicate the dislocation motion [133].

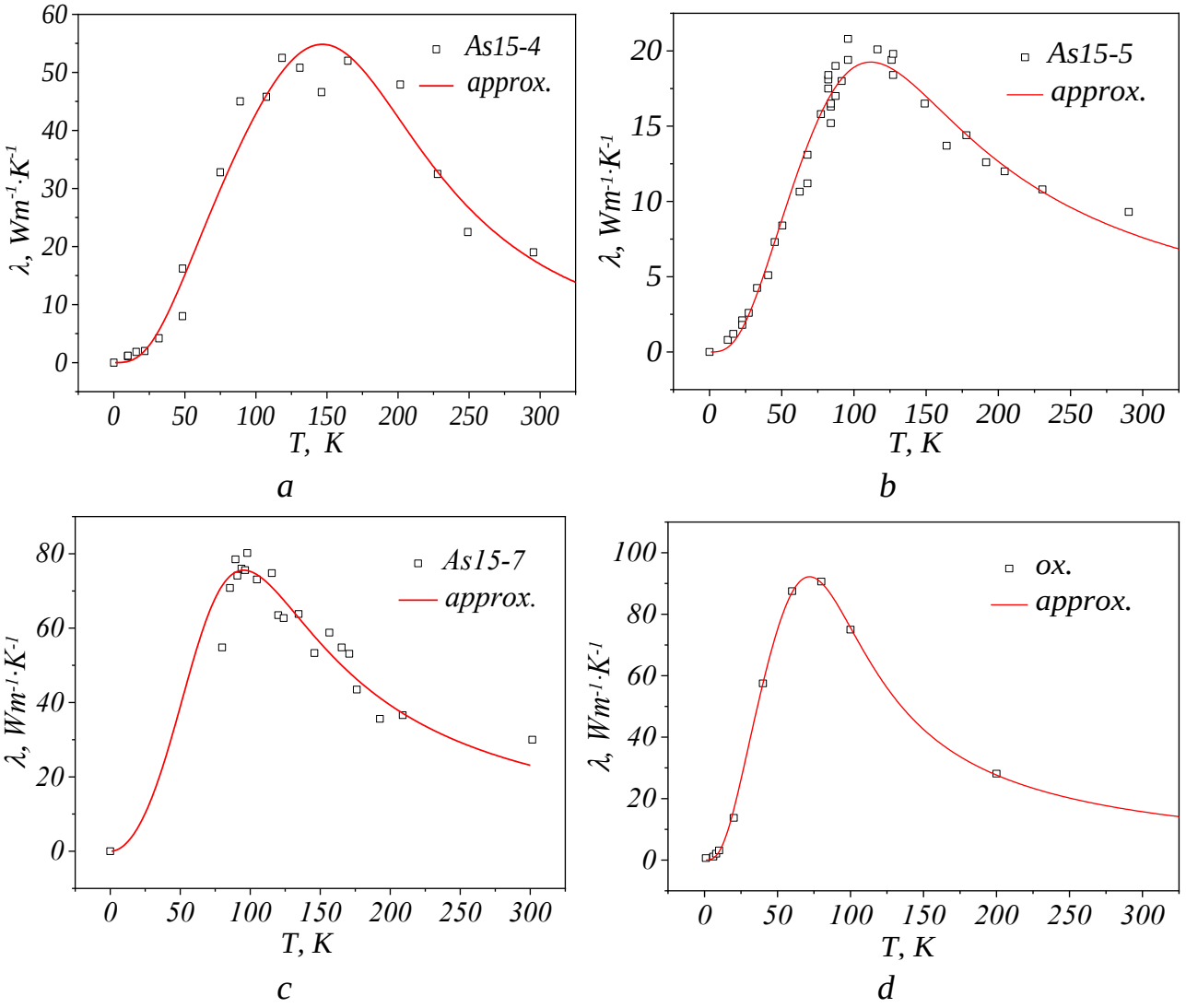

Figure 3.2 – Approximation of temperature dependencies of thermal conductivity for composites pressed at T_{sint}:
a – 1400 °C; *b* – 1500 °C; *c* – 1700 °C; *d* – pure Al_2O_3

Table 3.1 – Approximation of temperature dependences of thermal conductivity

Sample	T_{sint}, °C	Coefficients of approximation					$Adj.R^2$
		$A_1 \cdot 10^{-3}$, м	$A_2 \cdot 10^{-46}$, с^3	$A_3 \cdot 10^{-50}$, с	$A_4 \cdot 10^{-20}$, с/К	A_5	
As15-4	1400	0.267	0.41	1.01	3.01	1.44	0.998
As15-5	1500	0.172	1.16	1.00	1.96	2.80	0.999
As15-7	1700	0.565	0.17	1.10	0.52	3.48	0.996
Al_2O_3 [134]	–	3.210	0.42	1.00	0.81	3.14	0.999

As seen from table 3.1 the coefficient A_2, indicating the presence of point defects, is maximum for the sample sintered at the temperature T_{sint} = 1500 °C. A higher level of deformation solidification for the similar compaction conditions and the composition was also indicated by the data on the mechanical properties described above.

The coefficient A_3 has low values and does not affect the results of approximation. It proves the absence of two-dimensional defects in the samples under study.

In real crystals the character of maximum thermal conductivity at low temperatures depends on the combination of phonon scattering on phonons and defects (point defects, dislocations, inclusions, pores). These processes correspond to the coefficients $A_4 \ldots A_5$ and A_2 in the model used for approximation. When the crystal structure breaks and the defective capacity of a crystal increases, the peak of thermal conductivity rises with temperature and becomes less distinct up to its complete disappearance (for amorphous bodies) [128].

Fig. 3.3 gives temperature dependences of the thermal conductivity for composites based on Al_2O_3 sintered at various sintering temperatures T_{sint}.

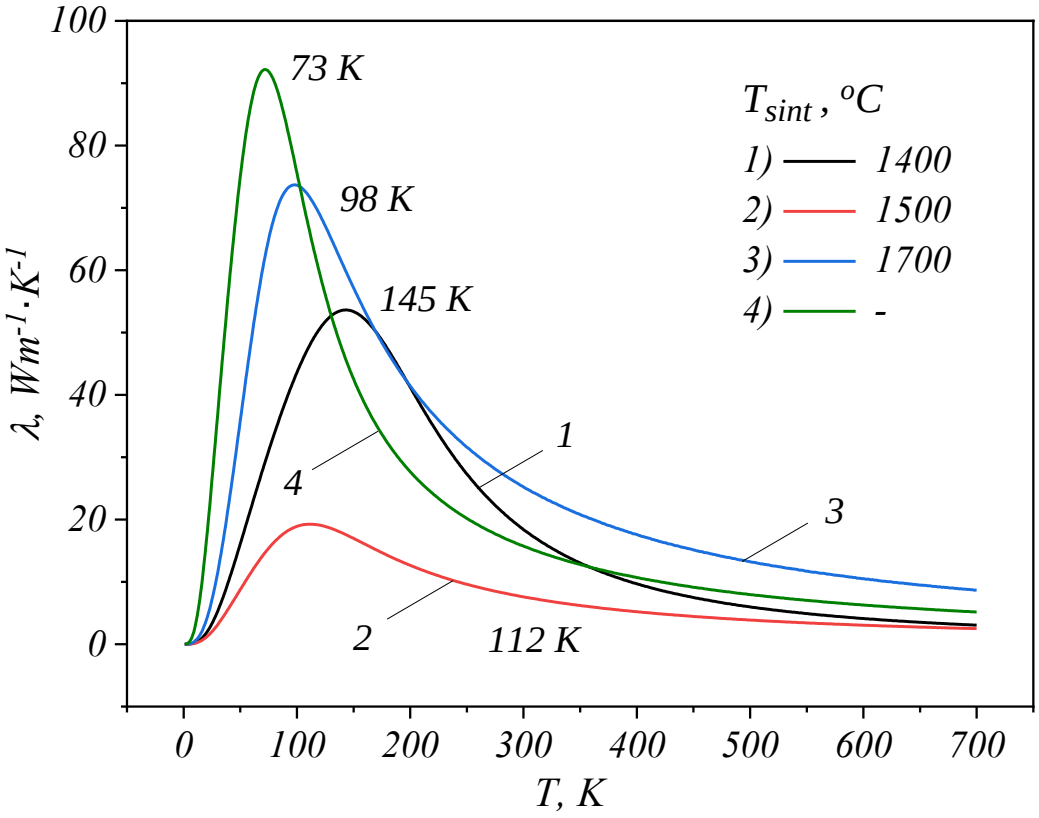

Figure 3.3 – Temperature dependencies of thermal conductivity for composites based on Al_2O_3 sintered at various T_{sint}

The peak displaces from 145 K to 98 K with a rise in the consolidation temperature. Pure alumina acts as a model in this case and its well-pronounced peak is at the temperature 73 K.

According to the above-mentioned, we can conclude that higher sintering temperature for Al_2O_3–SiC nano-composites produced with the electric consolidation method from 1400 to 1700 °C leads to an increase in the thermal conductivity coefficient through decreasing the defectiveness and increasing the consolidation of the composite. The level of thermal conductivity of such composites $\lambda \sim 25$ W/(m·K) can be compared with the parameters of the high speed steel R18. Higher thermal conductivity of ceramics to the level close to that of metal alloys at the hardness which is several times higher, makes them a good alternative to high-speed steels and solid alloyed, and in comparison with these materials they can be used at much higher cutting speeds.

3.3. Thermal-mechanical properties of instrumental materials

A known value of the thermal conductivity coefficient can be used to estimate distribution of the temperature fields in the volume of the composite product. In the process of high-speed treatment with tools (cutters) of ceramics and their composites the temperature in the cutting zone can reach 1100 °C [135].

The right selection of treatment modes and instrumental materials is based on the information on the heat wave velocity across the cutter with its further withdrawal from the cutting zone to the heat sink.

The similar calculations can be made with the value of temperature conductivity α, which numerically equals the ratio of thermal conductivity to the volume heat conductivity at the constant pressure [136]:

$$\alpha = \frac{\lambda}{C_p \cdot \rho}, \tag{3.14}$$

where ρ – density.

When selecting the material for production of tools, there is a need to consider each main property (hardness, crack resistance, temperature conductivity) and provide their optimal combination. However, it is not an easy task, and commonly this choice is based on only one property that mostly impacts the working capacity of this tool. The approach to these tasks is proposed in [137] with the introduction of the parameter

B, which includes the key properties needed for comparative evaluation of various materials.

The material for high-speed cutting tools must have high wear resistance and thermal conductivity, therefore, the thermal mechanical parameter *B* is the product of the temperature conductivity α and the micro-hardness H_V.

In the research the properties of the composite material obtained were compared with several existing materials used for similar tasks.

1) High-speed steel R18 – typical high-alloy steel. Great amount of wolframium (18 %) and other carbide-forming elements in similar steels provide the high heat resistance. These steels can improve the efficiency of treatment by 2…4 times in comparison with conventional carbon steels, and maintain the hardness HRC ≥ 60 to the temperature 620 °C.

2) Instrumental oxide-carbide ceramics VOK-60 used in mass production for manufacturing cutting plates for turning iron alloys and cast iron. They are produced of Al_2O_3 and TiC by hot pressing. It is intended for finish and semi-finish turning operations on hardened structural steels with a hardness of HRC ≥ 60, gray malleable cast irons at high-speed cutting velocities.

3) HC1 – white ceramic based on alumina produced by NTK (Japan). It is intended for semi-finish and finish treatment of cast iron at the speeds 500 m/min.

4) HC2 – ceramic based on alumina similar to HC1 ceramics, but with TiC additive and better hardness, produced by NTK (Japan). It is intended for treatment of tempered metals at higher temperatures at speeds of 400 m/min.

5) As15-6 – composite material obtained in the research. The foundation is micro-disperse alumina with 15 % mass nano-SiC additive sintered at T_{sint} = 1600 °C with the electroconsolidation method through direct passing of current. The axial pressure is P = 35 MPa, the hold time is t = 2 min.

The mechanical and physical properties of these materials, used in the comparative analysis, have been taken from literature and the author's research; they are presented in table 3.2.

Due to application of SiC additive, thermal conductivity of which is considerably higher than the heat conductivity of Al_2O_3 [134], the heat conductivity of the composite has been increased up to λ = 25…30 W/(m·K), which can be compared with the thermal conductivity coefficient of metal cutters of the high-speed steel R18. Besides, it should be noted that higher sintering temperature of up to 1700 °C contributes into the transformation of SiC from 3C (cubic) to 6H-polytipe (hexagonal) [141] with the thermal conductivity coefficient two times higher. Steel R18 has the lowest thermal mechanical parameter *B*. It can be explained by low hardness (H_V = 7.6 GPa) in

comparison with the hardness of ceramic materials. The hardness of oxide-carbide ceramics VOK-60 is two times higher (H_V = 14.6 GPa), and its heat conductivity is relatively low which ultimately impacts the parameter *B*, the value of which is only 33 % higher.

Table 3.2 – Mechanical and physical properties of some instrumental materials

Name	Composition	λ, W/m/K	ρ, g/cm^3	H_V, GPa	C_p, J/kg/K	$\alpha \cdot 10^{-6}$, m^2/s	$B \cdot 10^3$, N/s	Source
R18	Fe,W, Cr	22.1	8.80	7.6	393	6.4	48.6	[138]
VOK-60	Al_2O_3 TiC	15.0	4.30	14.6	800	4.4	64.2	[139]
HC1 (Japan)	Al_2O_3	17.0	4.00	18.0	750	5.7	102.6	[140]
HC2 (Japan)	Al_2O_3 TiC	21.0	4.30	21.0	796	6.1	128.1	[140]
As15-6	Al_2O_3 SiC	23.0	3.87	25.0	696	9.4	216.2	This research

According to these data, we can see that ceramic of micro-disperse oxide alumina reinforced with nanodisderse silicon carbide has the thermo-mechanical parameter *B* of the value about 200 that is four times higher than this value for high-speed steel R18 and two times higher than that for modern ceramics based on Al_2O_3 produced abroad.

3.4. Thermal processes and their dynamics during electroconsolidation

Application of innovative consolidation technologies for ceramic materials such as FAST (Field Activated Sintering Technology), SPS (Spark Plasma Sintering) and their combination can be used for fabricating new materials with submicron and nano-structures [142]. The advantage of these technologies is the activation nature of the electric field and current, which considerably intensifies the sintering process as compared to traditional methods.

High-dense Al_2O_3–SiC ceramic was obtained by means of the hot pressing method with direct current (electroconsolidation) after 3-min hold time; it cannot be achieved by conventional hot sintering methods due to rapid growth of grains and poor compactibility (fig. 3.4).

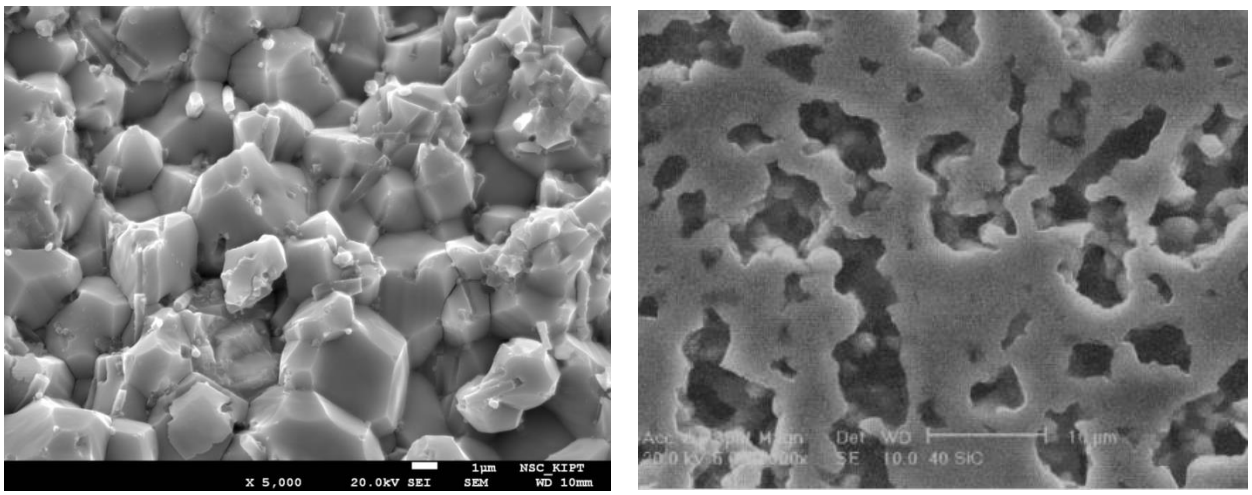

a *b*

Figure 3.4 – Microstructure of the ceramic sintered by means of the electroconsolidation method:
a – at T_{sint} = 1400 °C, t = 3 min, P_{ax} = 30 MPa; *b* – sintered in the argon media without activators [143]

Implementation of such technologies is explained by a need to carefully design the equipment directly involved in consolidation, as far as the required characteristics of material can be obtained only if the consolidation parameters (such as temperature, pressure, etc.) are accurate and predictable. And of high priority here is obtaining information on temperature distribution in the components of the installation, and also electric current distribution in the parts engaged in its transfer. The most accurate source of such information is computer simulation with special software.

Fig. 3.5 presents a design area in the form of a two-dimensional model of the installation for hot vacuum pressing. The task was solved with the finish element method together with the radiosity method, where the design area was divided into the mash of 923 eight-unit elements with quadratic approximation.

An alternating voltage of about 5 V was applied to the surfaces of the brass current carries with a frequency of 50 Hz. A special feature of such installations is a short synthesis period due to the current of about several kA. Besides, the heat exchange with the external environment and the heat exchange inside the installation were also included. The surfaces *ABC* and *OL* had the convective heat exchange with the flow of cooling water: the coefficients of convective heat transfer in the cooled zones were α_{top} = 35 kW/m^2·K and α_{bot} = 15 kW/m^2·K on the top and bottom current carriers, respectively.

On the *MD* and *KL* surfaces the heat exchange with the press plates is included through modelling the heat exchange with the coefficient of convective heat exchange.

On the *MDEFGHKL* surface the heat exchange with the air is included through the coefficient of convective heat exchange. In vacuum hollows *1* and *2* (fig. 3.5, *b*) the heat exchange runs by means of emission between the surfaces of structural elements forming these hollows.

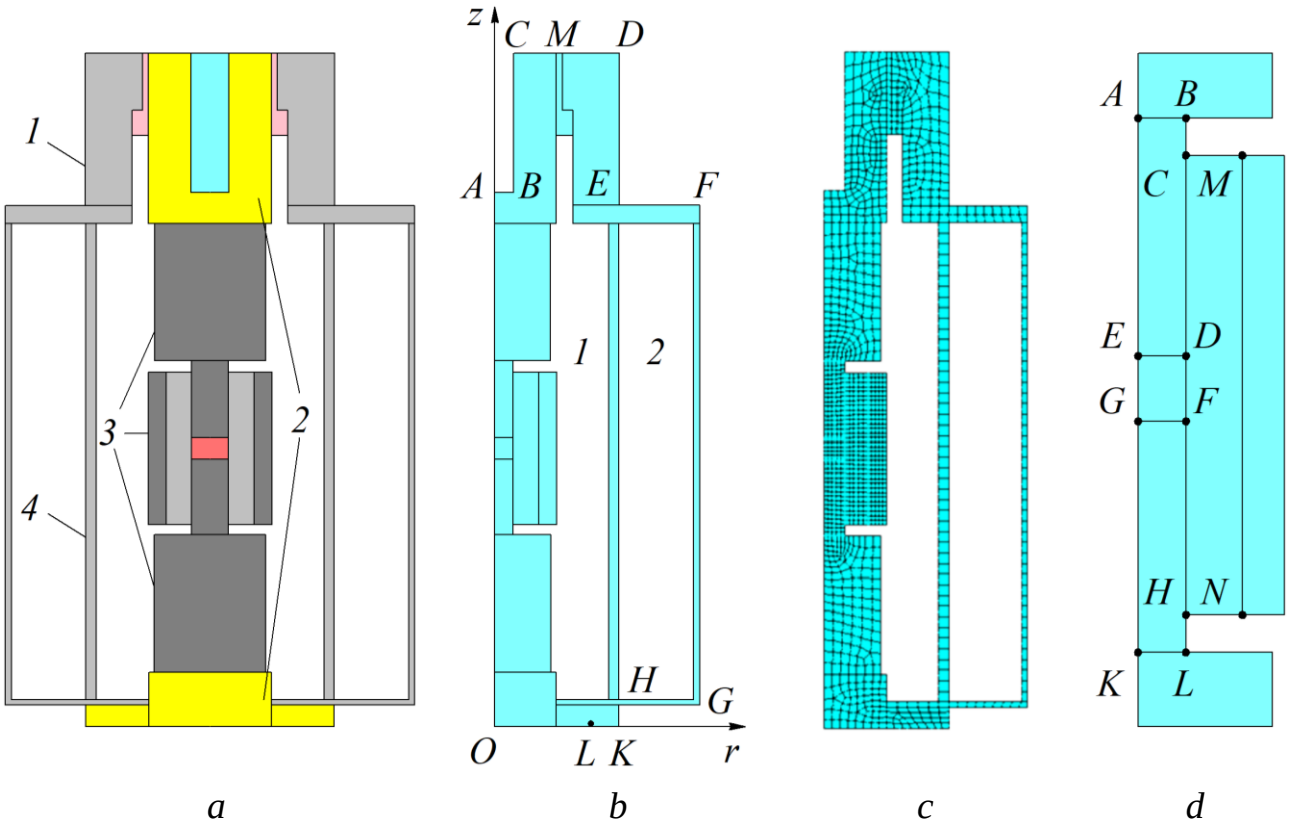

Figure 3.5 – Diagram of the installation for pressing (*a*), design area (*b*), its division into a mesh of finished elements (*c*) and contact electric and heat resistances on the contact surfaces (*d*):
Oz – pressing axis; *Or* – radial axis of the installation; *1* – body (steel);
2 – current carriers (brass) cooled by water; *3* – press mold and dies (graphite);
4 – inner lining (expanded graphite)

The contact electric and heat resistances on the contact surfaces are also included (fig. 3.5, *d*): *AB* and *KL* – graphite dies with graphite down conductors, *DE* and *FG* – sample with graphite dies; *DF* – sample with the graphite press mold; *CD* and *FH* – graphite dies with graphite press mold; *MN* – graphite press mold with the cylindrical panel. The values of contact electric and heat resistances and their dependency on temperature and compacting pressure were taken from literature.

Fig. 3.6 demonstrates dependencies of the temperature in different points of the sintering zone on time. The time interval from 0 to 400 sec corresponds to an intensive

heating, and from 400 sec – to the onset of the temperature mode and the beginning of sintering. The diagram shows that in the pairs of points *s1–s4* and *s2–s3* the temperature is maintained over the whole interval; it indicates the absence of an axial gradient of temperature between the top and bottom dies. This heat dissipation balance proves that the calculation made for the components of the installation and the cooling system of the top and bottom current conductors was correct.

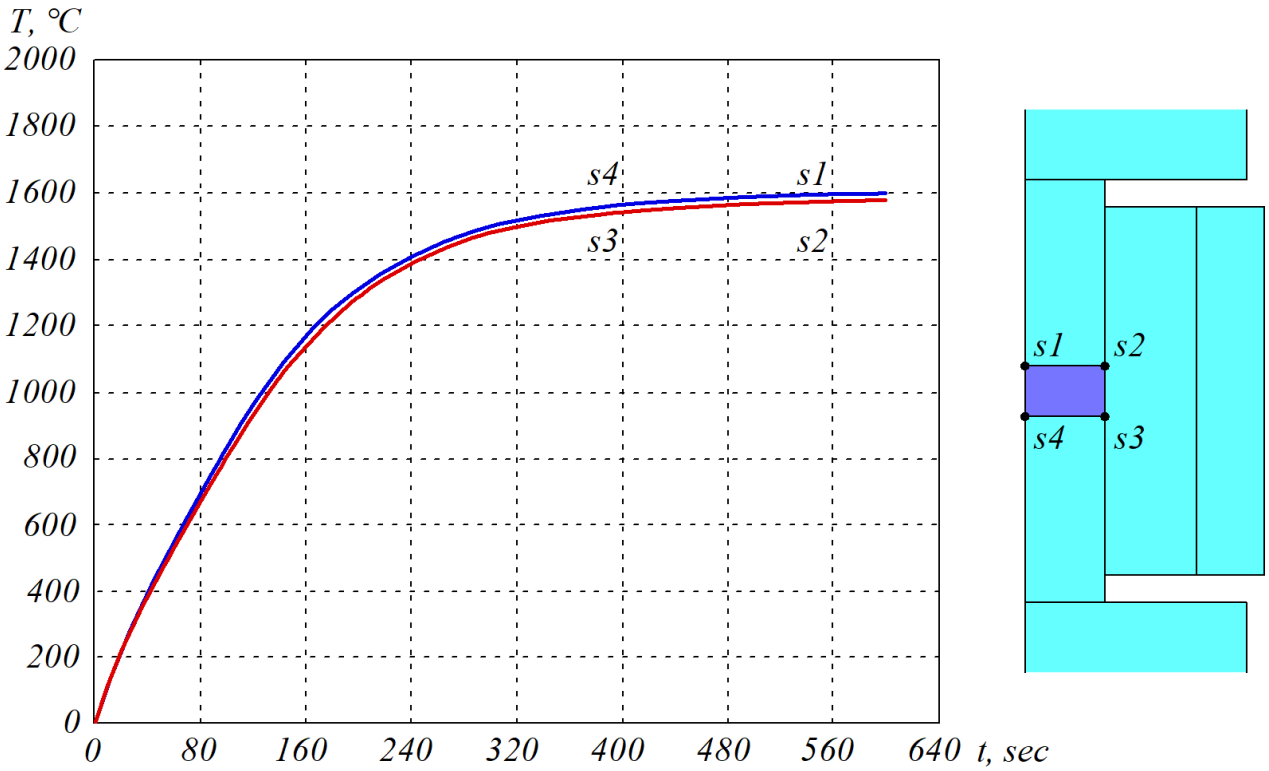

Figure 3.6 – Change of temperature in the points on the surface of compacted volume:
s1–s2 – upper surface; *s3–s4* – lower surface

On reaching the compacting temperature there is observed a small difference of temperature in the points *s1* and *s2* (*s3* and *s4*) due to the heat removal through the external part of the press mold by means of emitting. Despite the radial gradient the difference of temperature between the center and the edges of compacting does not exceed 10 K, which, in this case, corresponds to 0.6 % out of the sintering temperature.

The results of compacting for powder materials can be forecast and reproduced through careful control of the main consolidation parameters, such as temperature, pressure and hold time. The temperature control in the compacting zone is the most difficult task, because the access to it is complicated. But the temperature control on the edges of the press mold is a relatively simple solution to it.

Fig. 3.7 gives temperature changes in the points on the radial axis obtained by mathematical modelling. Thus, the diagram shows that the temperature control on the edges of the press mold (point *c3*) has to include the difference of temperatures $\Delta T \approx 200$ K.

The model designed can be verified by comparing the results of modelling with the actual values obtained by measuring.

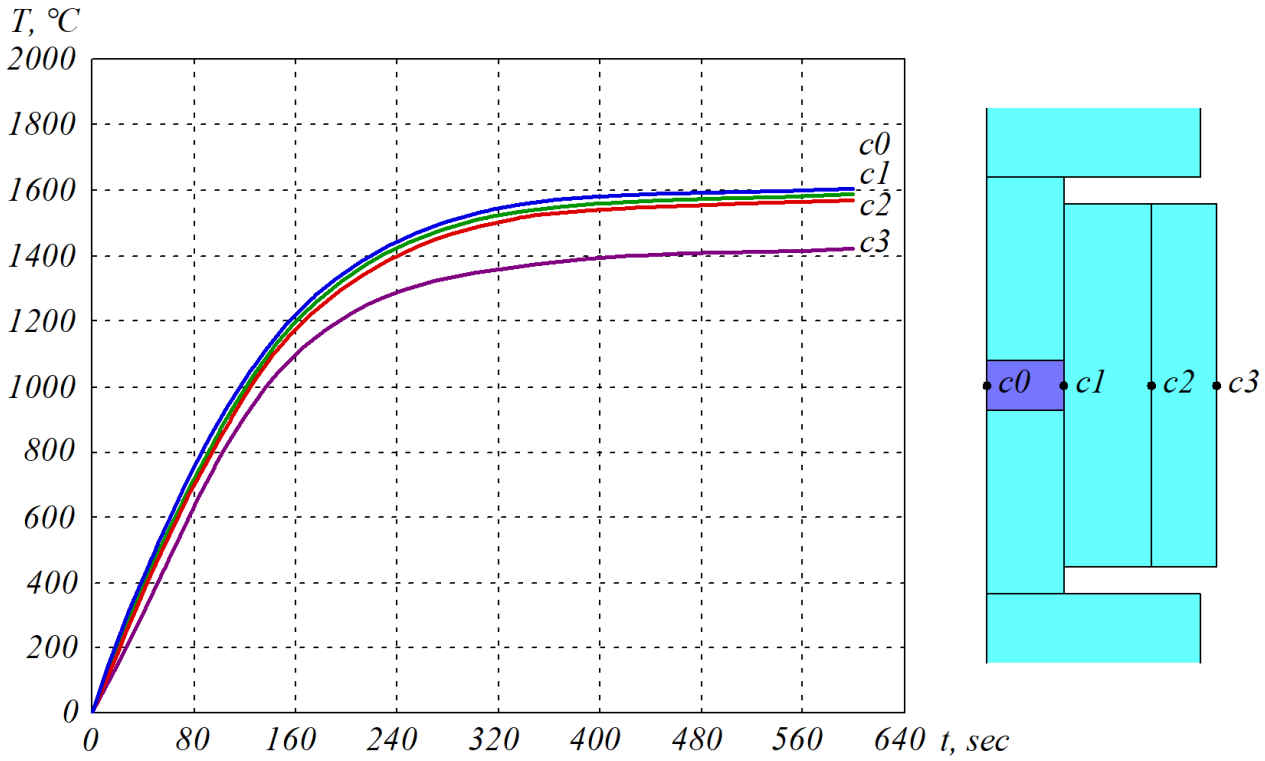

Figure 3.7 – Change of temperature in points on the cross axis:
c0 – center of compacted volume; *c1* – border with the press mold; *c2* – border of the press mold with the composite die; *c3* – external part of the die

Fig. 3.8 gives time dependencies of the temperature measured on the edges of the press mold during electroconsolidation and the results of simulation. The differences at the previous stage are the result of the different initial current and, consequently, the heating speed.

The action of electric field for an actual process and for the model stops at $t = 1100$ sec and $t = 1000$ sec, respectively.

If the differences in the values of the current at the initial stage are reduced to the minimum, the results of modelling will fully correspond to the actual behavior of the temperature in the controlling point, which confirms the validity of the results obtained through simulation.

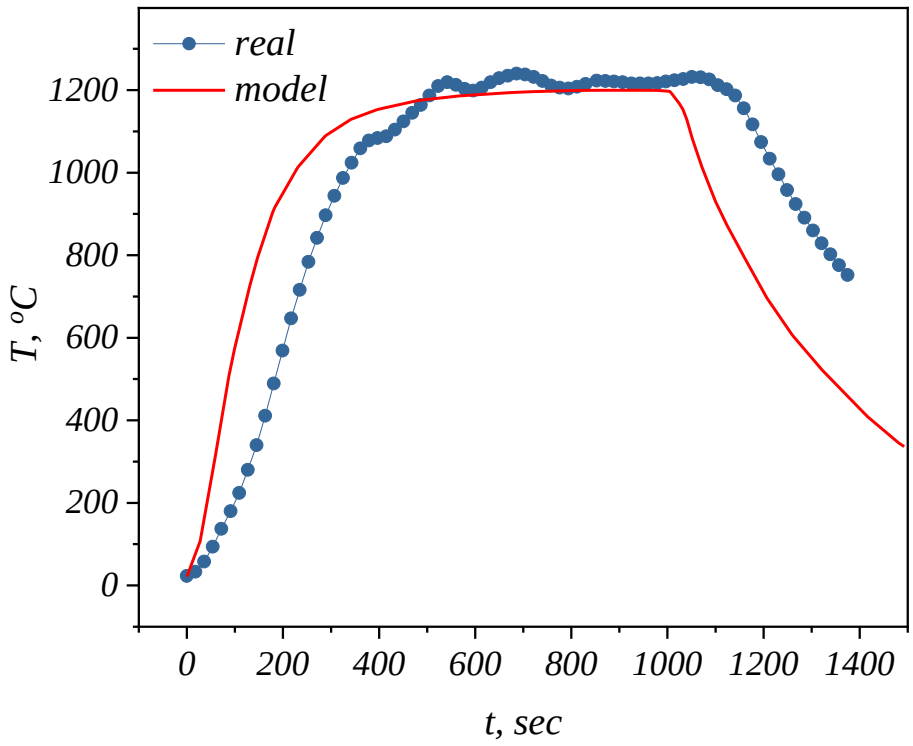

Figure 3.8 – Dependency of the temperature of the die in the press mold on time: *points* – actual measurements; *solid line* – result of modelling

Fig. 3.9 shows the temperature field dynamics in the volume of the press mold and the installation elements during electroconsolidation. These data are the results of the computer modelling described above. As is seen, the maximum speed of heating is achieved in graphite dies, as the density of current running in these areas is maximal. Besides, the absence of high temperature gradients in the pressing zone proves the right configuration of the press mold and its sizes. In any direction the temperature gradient is symmetrical to the pressing zone, which has a positive effect on the homogeneity of sintered products.

More detailed distribution of temperatures in the pressing zone is presented on the diagrams in fig. 3.10 where each shows the temperature field in different time moments. It can be noted that the central parts of the upper and lower boundaries of the sample have the maximum temperature in the process of heating.

The highest non-homogeneity of the heating of the volume with the batch during pressing is observed at the initial stage in the course of intense heating (fig. 3.11), the speed achieves 360 °C/min, the difference of temperature in the compacted volume does not exceed 12 %.

ΔT_{max} has an obvious correlation with the temperature variation rate, and as far as the actual heating speed at electroconsolidation is about 200 °C/min, it indicates that the value ΔT_{max} = 12 % cannot be reached.

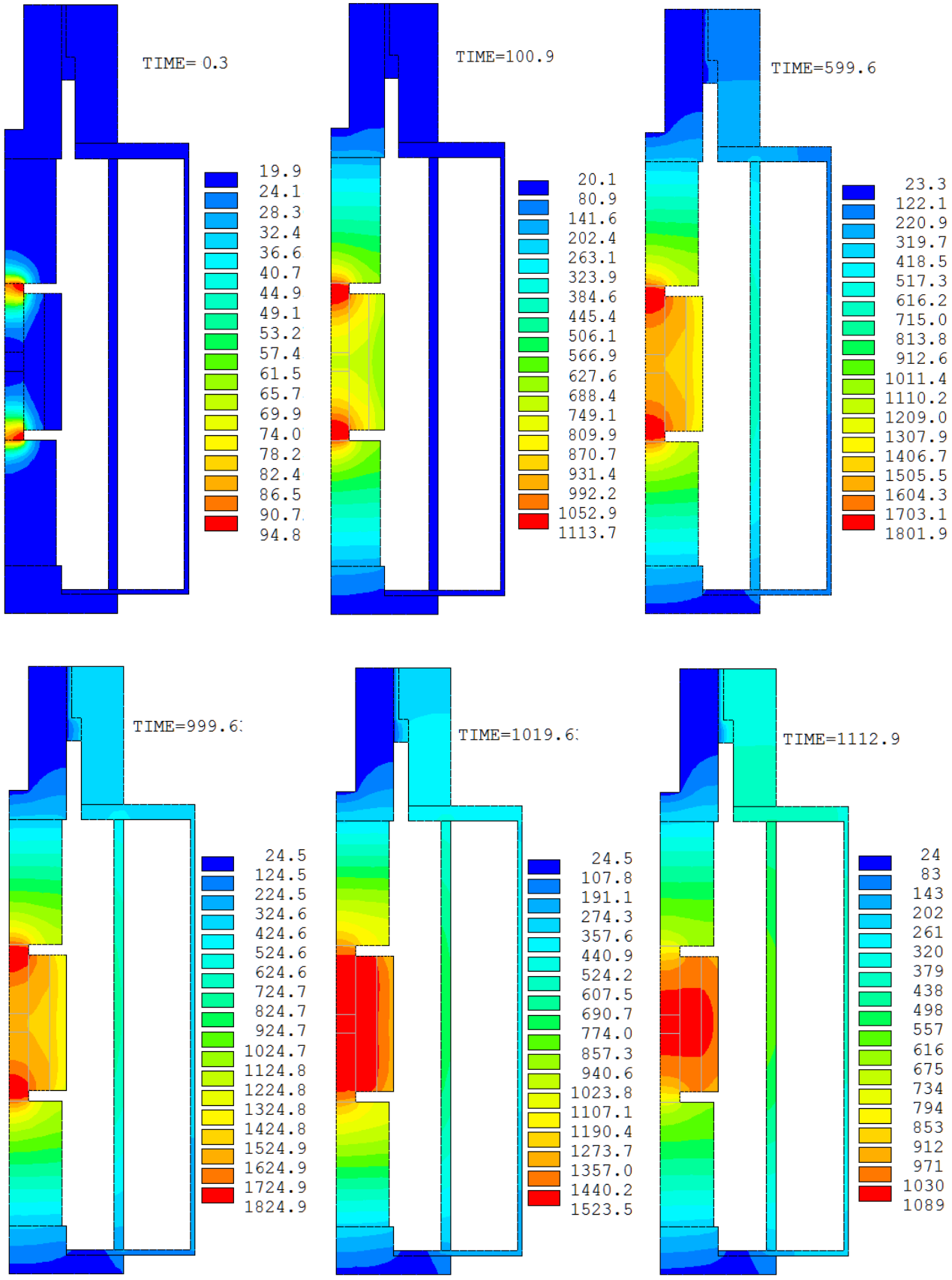

Figure 3.9 – Dynamics of the temperature field in the volume of a press mold and the installation elements during electric consolidation (TIME – period in seconds; temperature is coloured, °C)

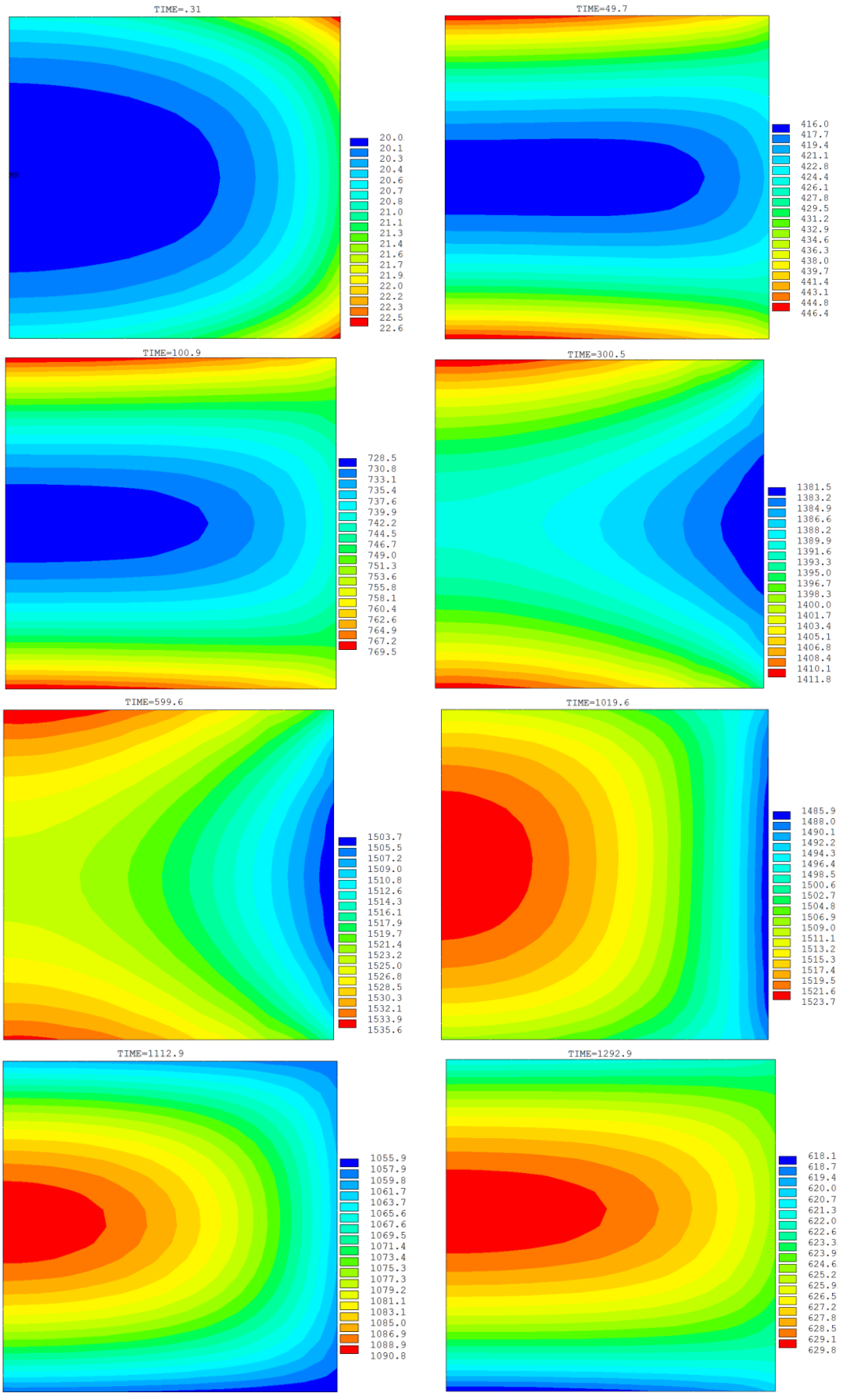

Figure 3.10 – Distribution of temperature in the compacted volume in the course of consolidation (TIME – period in seconds, temperature in °C)

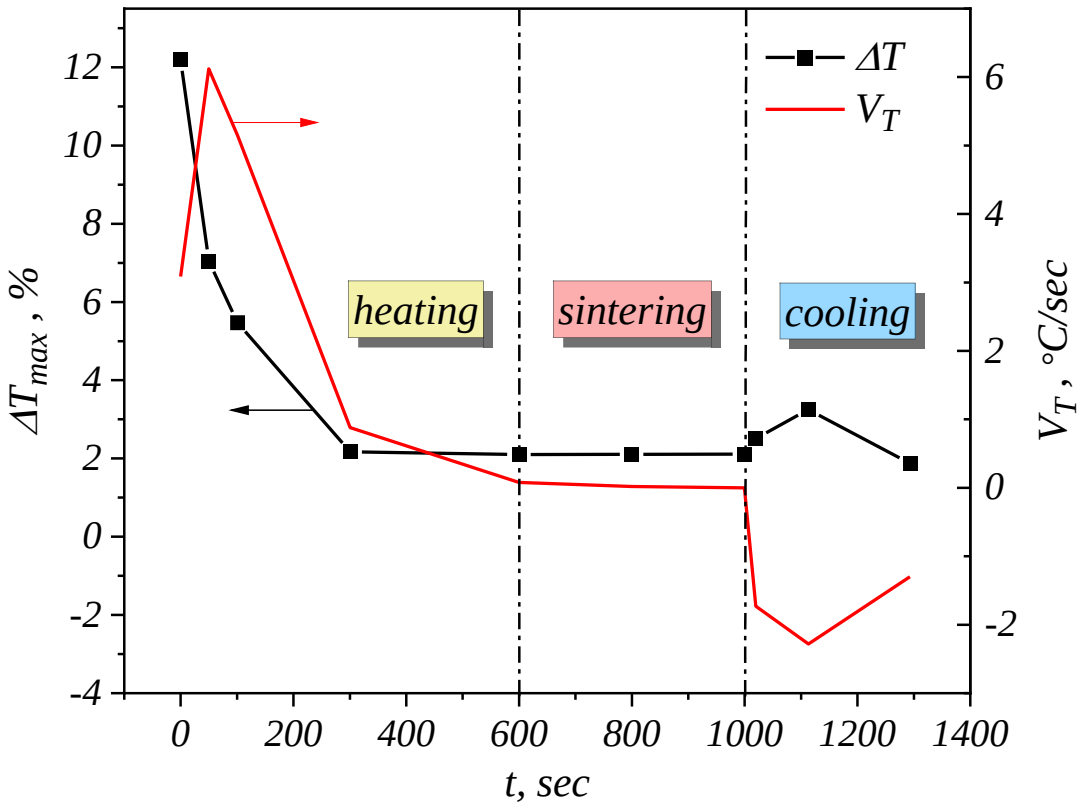

Figure 3.11 – Temperature variation rate in the compacted volume ΔT_{max} and the heating (cooling) speed v_T in the process of consolidation

The temperature variation rate v_T (fig. 3.11) is the temperature derivative T by time, correspondingly, v_T obtains negative values on the cooling stage when the temperature decreases. Despite the absence of high temperature differences (> 10 %) in the whole process of electroconsolidation, what is more important in terms of the control of technological parameters is a homogeneous temperature distribution at the sintering stage.

The results of modelling (fig. 3.11) show that the homogeneity of temperature in the compacted volume does not exceed 2 % out of the sintering temperature. The adequacy of this was confirmed at the sintering stage (t = 600…1000 sec) that indicates that the properties of materials are fully maintained, especially, with subsequent mechanical treatment of their surfaces.

3.5. Technological process of production of cutting plates of composite material (As15-6)

The research into the structure formation and properties of Al_2O_3–SiC composite materials with different SiC content in the primary mixture has allowed developing the

technology for fabricating new instrumental material As15-6 intended for the finish and semi-finish turning of hardened steels. The main component of this material is alumina; its unique abrasive properties are maintained after hot pressing. The primary powders of alumina and silicon carbide were mixed in ceramic drums in the isopropyl alcohol media. They were mixing in the planetary mill over two hours. Then the powders were dried in the vacuum drying oven and sieved. After that some amount of the batch obtained was placed in the graphite press mold and pressed at 35 MPa and the temperature 1600 °C for an isometric hold time from 3 to 5 min. These process parameters make it possible to obtain samples with high relative density and fine structure.

The technological production diagram of cutting plates of As15-6 nanocomposite is given in fig. 3.12.

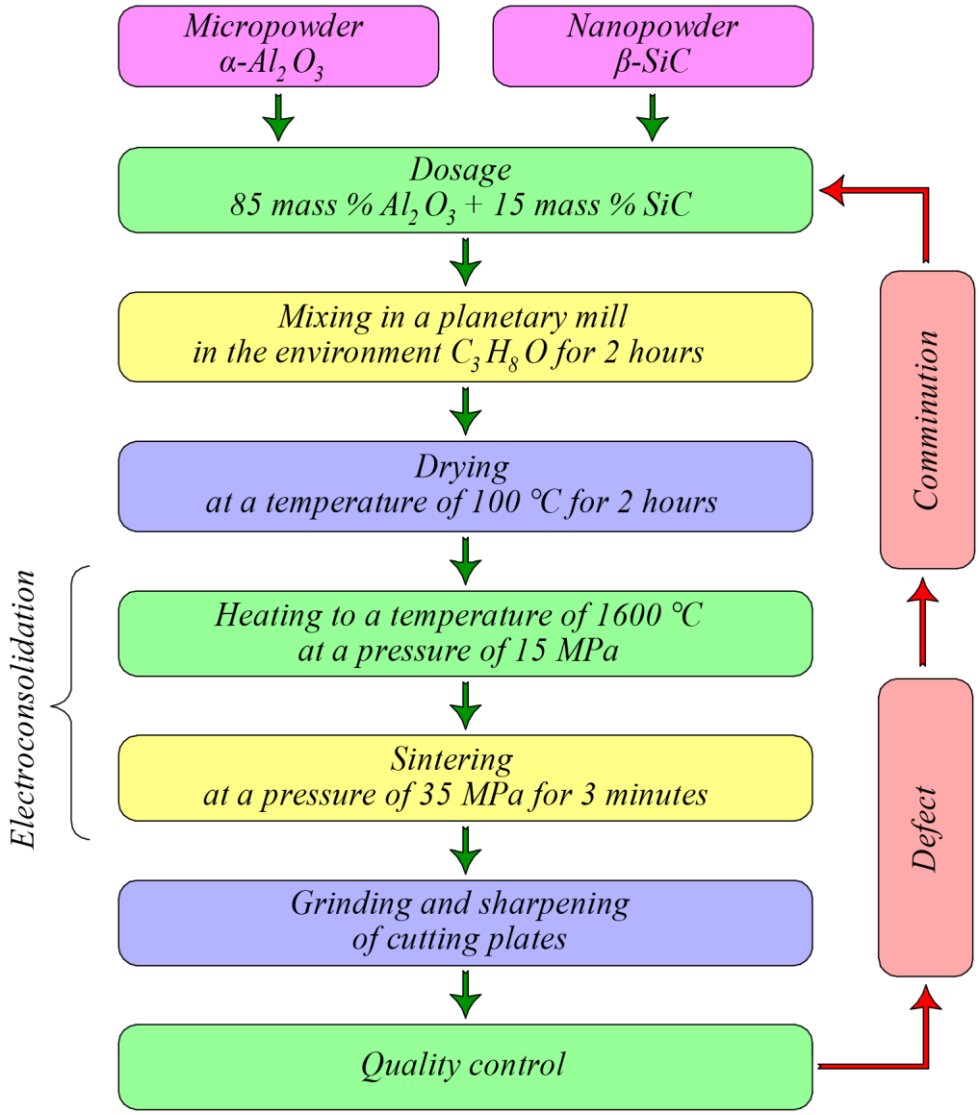

Figure 3.12 – Technological diagram of manufacturing cutting plates of As15-6 nanocomposite

Hot vacuum pressing can be used for manufacturing composites with fine-disperse structure and high purity of grain boundaries, which eventually guarantees obtaining samples with better mechanical properties. These samples have to be grinded with the 100/80 diamond wheels bonded organically. They are processed with a cutting speed of 25…30 m/s to a depth of up to 0.02 mm per double run.

The further refinement of the sample edges is made on the universal grinding machine with a cup wheel with a grain fineness of 20/14, and the final height of micro-irregularities of the cutting edges is 0.4…0.6 mkm.

3.6. Research into the cutting properties of As15-6 composite material

The most important criterion of instrumental materials is their wear resistance that depends on the wear processes at certain cutting modes for some workpieces. In the moment of cutting the stresses and temperatures at the cutting angle reach such values at which the following clogging can occur: hardenings in the plastic state on the chip-tool interface, and a relative motion of the chip towards the tool creates an intensive shear zone between the chip and the tool. It generates the heat that partially goes to the chip, but can also rise the temperature on some areas of the tool up to 1000 °C [135]. Due to high temperatures the wear processes in the tool can be both mechanical and chemical. The abrasive wear occurs at mechanical impact of solid particles in the workpiece; therefore the material for the tool must be hard and have enough fracture toughness. When the flank wear land reaches some value the cutting edge can fracture or spall. Their intensity on the cutting edge is determined by dynamic properties of a workbench [144], working modes and the structure of a cutting material.

The research into the properties of As15-6 material was made in the process of turning the thermally treated Steels 45 (40…45 HRC), HVG (58…60 HRC), ShH15 (58…60 HRC), a also Cast iron VCh45 (38…40 HRC). The results were compared with oxide ceramic VO-13, oxide-carbide ceramics (VOK-60, VOK-71) and oxide-nitride ceramic (Kortinit). The comparison included the working mode within $v \times s \times t$ = 100…300 m/min × 0.085…0.3 mm/r × 0.1…0.5 mm.

Fig. 3.13…3.16 present the results of the research in the form of dependencies between the strength of cutters and the cutting speed at different cutting modes, and also dependencies between the flank wear land and the cutting time. The strength was determined as a time over which this wear reached the value $h_з$ = 0.3 mm.

In the process of turning the rolls of hardened Steels HVG and ShH15 at cutting parameters of $v \times s \times t$ = 120 m/mm × 0.1 mm/r × 0.2 mm the strength of composite

As15-6 was at the same level as for plates of VOK-71 and amounted to about 65 min. The rigidity of the surface was R_a = 0.70. When the speed reached s = 0.25 mm/r the strength of the plates of As15-6 decreased two times, and for the plates of VOK-71 – four times, the plates of VOK-60 spalled at the first seconds of turning. When the cutting speed reached 200 m/min the strength of the plates of As15-6 composite was 15 min; it was five times less than the strength of the plates of VOK-71.

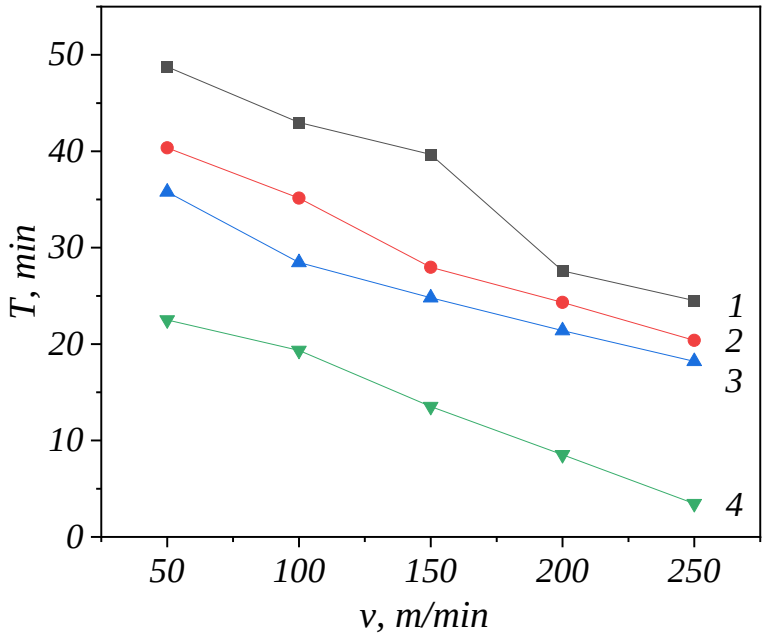

Figure 3.13 – Dependency of the wear resistance of cutting ceramic plates on the cutting speed during treatment of Steel ShH15 (58…60 HRC): *1* – As15-6; *2* – ONT-20; *3* – VOK-60; *4* – VO-13 (cutting mode $s \times t$ = 0.15 mm/r × 0.2 mm)

Fig. 3.14 presents the dependency between the flank wear of the cutting edge on the turning time for some cutting plates of various materials. The wear intensity of serial plates of oxide and oxide-carbide ceramics (VO-13, VOK-71) increases over time, however cutting plates of the composite obtained demonstrate the opposite effect. It confirms the optimal cutting mode and temperature for composite As15-6. One of the tasks in developing the new composite cutting material of ceramic was to obtain its better thermal and physical properties to provide favourable temperature conditions for cutters working at higher processing speeds. The thermal conductivity of the material obtained ($\alpha = 9.4 \cdot 10^{-6}$ m^2/s) exceeded the existing oxide-carbide analogies at least 1.5 times. It testifies that a heat removal rate is higher in the cutting zone; this fact is very important for ceramics that are sensitive to heat impacts, and this can be seen in fig. 3.14.

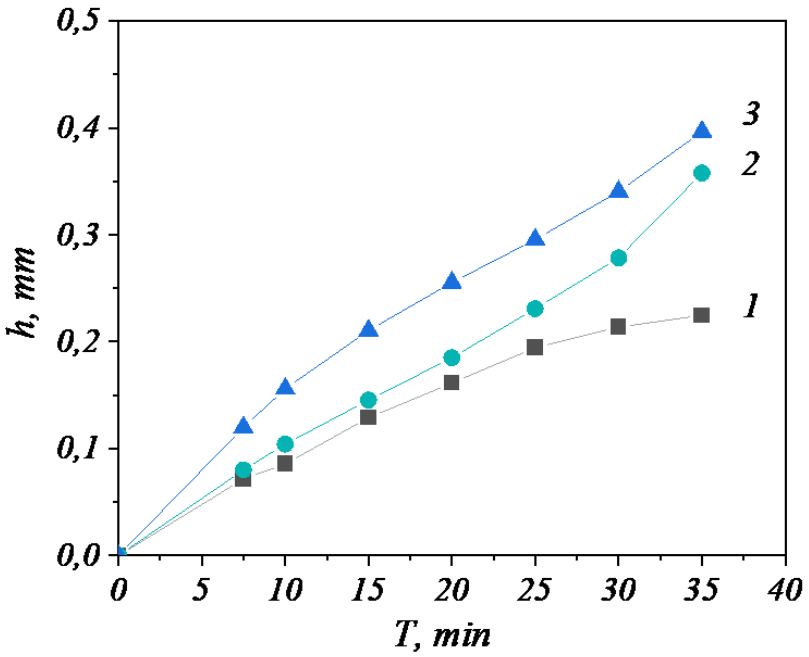

Figure 3.14 – Dependency of the flank wear on the processing time for Steel 45 (40…45 HRC) with plates of:
1 – As15-6; *2* – VOK-71; *3* – VO-13
(cutting mode $v \times s \times t$ = 200 m/min × 0.085 mm/r × 0.2 mm)

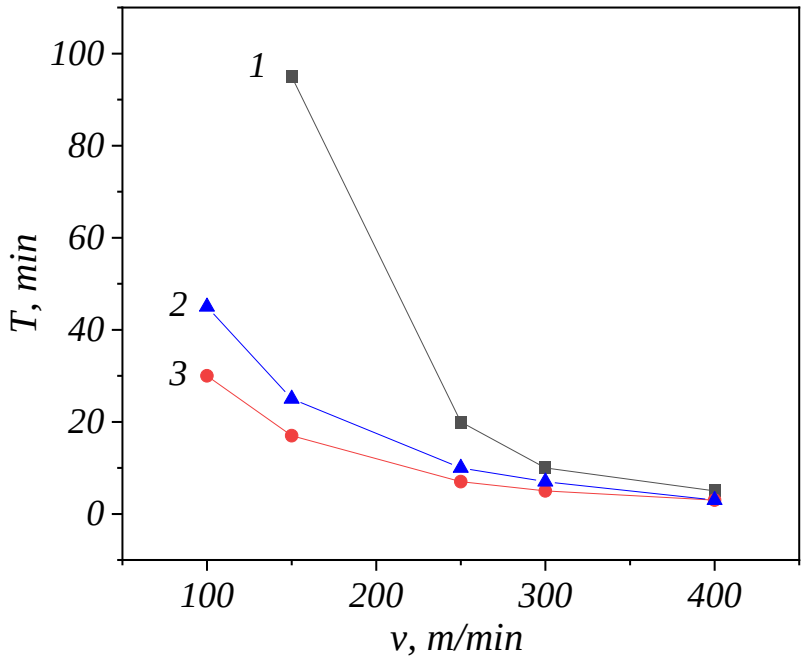

Figure 3.15 – Dependency of the wear resistance of cutting ceramic plates on the cutting speed during processing of Cast iron VCh45:
1 – As15-6; *2* – VOK-71; *3* – ONT-20
(cutting mode $s \times t$ = 0.2 mm/r × 0.5 mm)

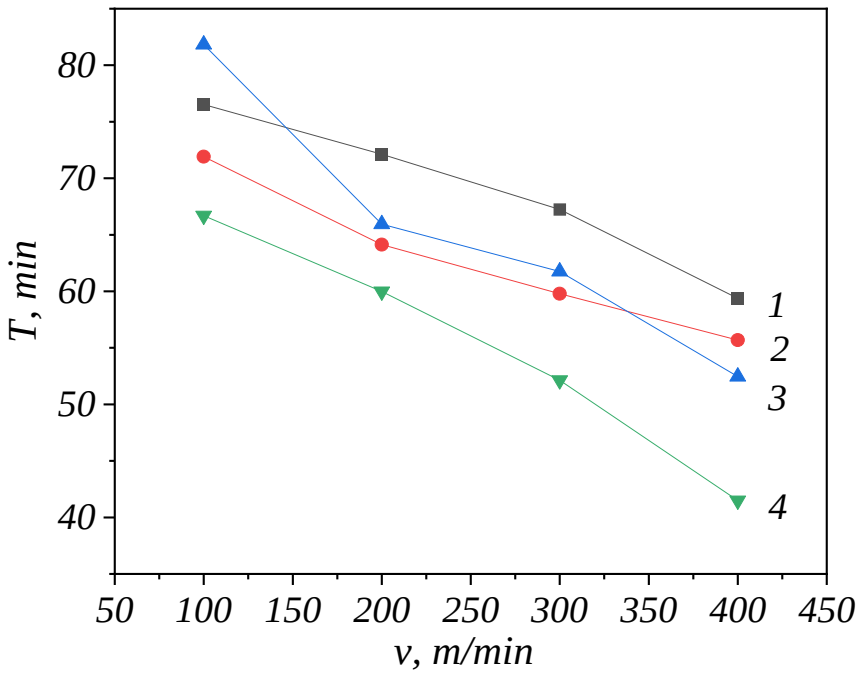

Figure 3.16 – Dependency of the strength of cutters with plates of ceramics during turning Steel 45 (40…45 HRC) on the speed:
1 – As15-6; *2* – ONT-20; *3* – VOK-71; *4* – VO-13
(cutting mode $s \times t$ = 0.085 mm/r × 0.2 mm)

The wearing of cutting ceramics accompanies by creating a hole on the rake face and a dimpled zone on the flank face (fig. 3.17). The research demonstrates that the wear of cutting ceramic As15-6 can be considered through universal wear dependencies [145] of the cutting instrument.

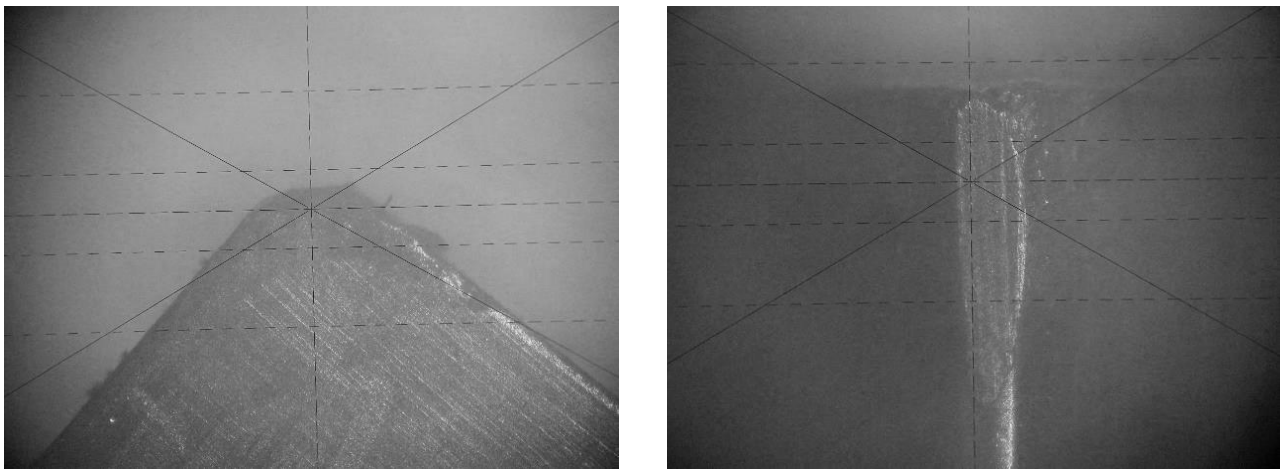

a *b*

Figure 3.17 – Wear of the rake (*a*) and the flank (*b*) faces on the cutting edge of an As15-6 plate after testing

After diamond turning the grains in the oxide, nitride and carbide phases of the ceramic have a certain dislocation density. In the process of external friction during cutting the dislocation density in the grains increases.

The analysis of microphotography of the wear surface demonstrates that wearing of As15-6 ceramic runs together with micro-deterioration of the grains as a result of a rise in dislocation density up to critical, cyclic slacking and breakaway of grains.

The fractographic analysis shows the predominance of the grain-boundaries fracture mechanism (intercrystalline), while the fracture of big grains are transcrystalline (fig. 3.18). The development of microcracks on the grain boundaries due to pore formation and creep in the surface layers leads to spallation on the cutting edge. High spallation resistance of As15-6 ceramic is conditioned by its high dispersity and presence of excess mechanical stresses around SiC grains.

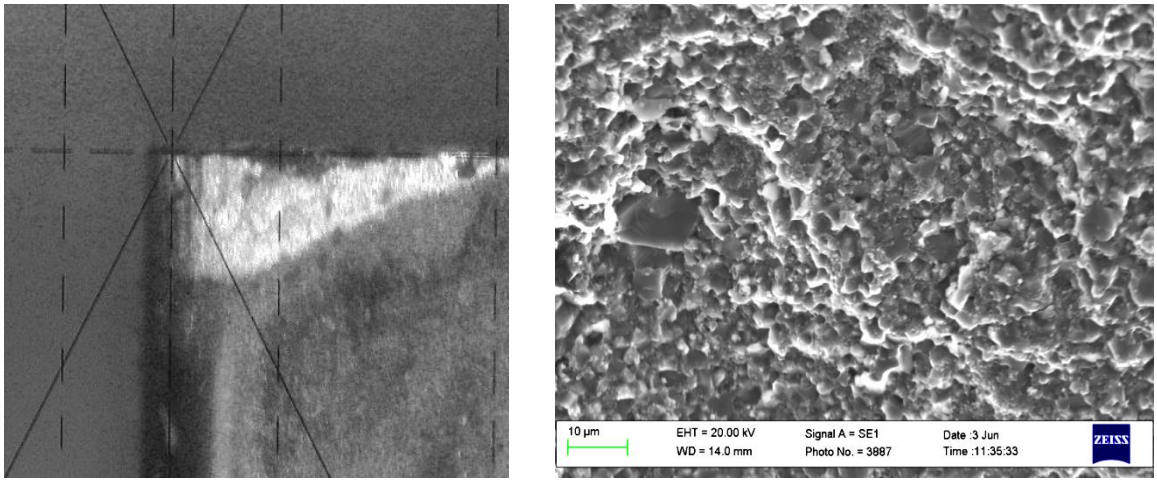

a *b*

Figure 3.18 – Cutting edge (*a*) and fracture pattern (*b*) of the cutting plate of As15-6 composite

After the diamond turning the surface layer of the ceramic is solid up to a depth of 2…5 mkm and without high internal stresses in the volume.

The porosity of As15-6 ceramic does not exceed 1 %; the pores are round-shaped, which also decreases the stress concentration in the volume (fig. 3.19).

The structure analysis for ceramics VO-13, VOK-60, VOK-71 and ONT-20 with electronic microscopy demonstrates that these instrumental materials can be considered as disperse-reinforced materials [146]. According to the ceramic grade its matrix is hardened with particles of oxides and carbides (TiC, TiN, ZrO_2, etc.). The material designed is reinforced with silicon carbide particles. The size of Al_2O_3 particles in ceramic VO-13 exceeds 3 mkm.

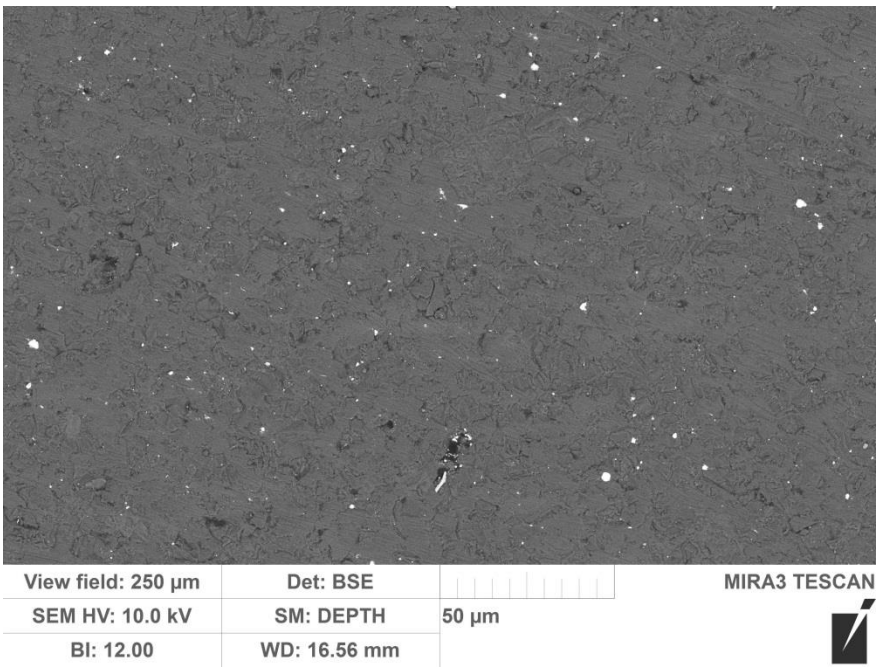

Figure 3.19 – Surface structure of As15-6 composite after diamond turning

In oxide-carbide ceramic the size of Al_2O_3 grains reach 2...5 mkm, and those of TiC reach 0.2…0.7 mkm. The size of strengthening particles in As15-6 is 50…100 nm. The content of strengthening particles (TiC, TiN, SiC) in ceramics is various: for example, in oxide-carbide ceramics VOK-60 it reaches 40 mass %, in material As15-6 – only 15 mass %. The physical and mechanical properties of As15-6 and some cutting materials are given in table 3.3.

Table 3.3 – Physical and mechanical properties of some cutting ceramics

Ceramics grade	Production method	*HRA*	ρ, g/cm^3	σ_{flex}, GPa	K_{IC}, MPa·m$^{1/2}$	λ, W/m/K	Grain size, mkm
CC620	HP	93	3.97	0.48	6.1	–	2
VO-13	Sintering	92	3.95	0.50	3.5	20	3…4
VOK-60	HP	94	4.30	0.60	4.2	22	2…3
ONT-20	HP	90…92	4.39	0.64	4.5	–	2
VOK-71	HP	92…93	4.52	0.65	5.6…6.0	22	2…3
As15-6	HP	94	3.83	0.85	6.5	23	1…2

As known, disperse reinforcement of materials [146] is determined by the morphology and the size of particles in the reinforcing phase, the content and the strength of interphase boundaries. This strength depends on the ratio of the elasticity coefficients of the reinforcing phase and the matrix, their thermal expansion

coefficients, and the solubility level in the reinforcing phase in the matrix. The higher is the ratio of the elasticity coefficients in the matrix and reinforcing phases, the higher is the stress concentration on the interphase boundaries.

Table 3.4 gives a ratio of the elasticity coefficients of the reinforcing phases to the elasticity module in the matrix, and a ratio of the thermal expansion coefficients (TEC).

Table 3.4 – Ratios of elasticity coefficients and thermal expansion coefficients

Ratios of the Young's modulus E and TEC α	$\frac{TiN}{Al_2O_3}$	$\frac{TiC}{Al_2O_3}$	$\frac{SiC}{Al_2O_3}$
E_1/E_2	0.7	1.3	0.9
α_1/α_2	1.2	1.0	2.0

Table 3.4 shows that the oxide matrix silicon carbide forms a higher stress concentration on the interphase boundary than titanium carbide or titanium nitride. Besides, SiC grains are more disperse; therefore they are more coherent with the matrix. Thus, the high wear resistance of As15-6 during the processing of hardened steels can be explained by higher strength of interphase boundaries.

A potential reaction and its types between the material under processing and the structural components of cutting ceramics can be forecast on the basis of calculation of thermodynamic potential.

The research demonstrates that the temperature in the cutting zone in fine surface layers can reach the phase-transition temperature of iron ($Fe_\alpha \rightarrow Fe_\gamma$). High pressures initiate dissociation of iron carbide. Thus, the main elements diffusing into the surface layers of ceramics can be ionized iron and carbon as they are in austenite. However, the calculation demonstrates that for the reaction $Al_2O_3 + 2Fe \rightarrow 2Al + Fe_2O_3$ the thermal dynamic potential is positive in a wide range of temperatures and the reaction is energetically unfavourable.

The reactions with carbon such as $2Al_2O_3 + 9C \rightarrow Al_4C_3 + 6CO$ can run at the temperatures > 1800 °C which is beyond the working temperature of cutting tools. At a temperature of 1100…1300 °C the reaction between Al_2O_3 and silicon, magnesium or calcium (their oxides) containing in steel is possible.

The X-ray analysis does not reveal carbides and pure Fe and Al in chip and materials under processing as the result of potential renovation of their oxides. However the strata of the material under processing on the contact areas contains oxides FeO and Fe_2O_3.

3.7. Forecasting the mechanical properties for Al_2O_3–SiC composite according to the primary consolidation settings

The mathematically processed experimental data on the mechanical properties were used for obtaining the empirical mathematical dependencies of the main strength characteristics, such as the micro-hardness H_V and the crack resistance coefficient K_{IC}:

$$H_V(T,x) = A_0 + \frac{A}{D_T \cdot D_x}, \tag{3.15}$$

where

$$D_T = n + \left(\frac{T - T_C}{W_T}\right)^2 - b_T \cdot \left(\frac{|T - T_C| + T - T_C}{2 \cdot W_T}\right)^2, \tag{3.16}$$

$$D_x = \frac{1}{n} + \left(\frac{x - x_C}{W_x}\right)^2 - b_x \cdot \left(\frac{x - x_C - |x - x_C|}{2 \cdot W_x}\right)^2; \tag{3.17}$$

$$K_{IC}(T,x) = A_0 + \frac{A}{\left[n + \left(\frac{T - T_C}{W_T}\right)^2\right] \cdot \left[\frac{1}{n} + \left(\frac{x - x_C}{W_x}\right)^2\right]}, \tag{3.18}$$

where T – sintering temperature; x – SiC content in the primary mixture in mass %.

Equations (3.15) and (3.18) are three-dimensional variations of the Lorentz function. The coefficients for these equations are given in table 3.5.

Table 3.5 – Coefficients for equations (3.15) and (3.18)

Factor	A_0	A	T_C, °C	W_T	x_c, %	W_x	b_T	b_x	n
for H_V	8.0	16.8	1620	180	15.1	30.0	0.8	0.5	1.3
for K_{IC}	3.5	3.3	1560	120	15.0	0.6	–	–	1

The diagram of the obtained functions in the form of continuous surfaces together with these coefficients is given in fig. 3.20. Fig. 3.20 shows that the optimal amount of SiC additive in the composite under consideration is 15 mass %, and the optimal consolidation temperature for this composition is 1600 °C.

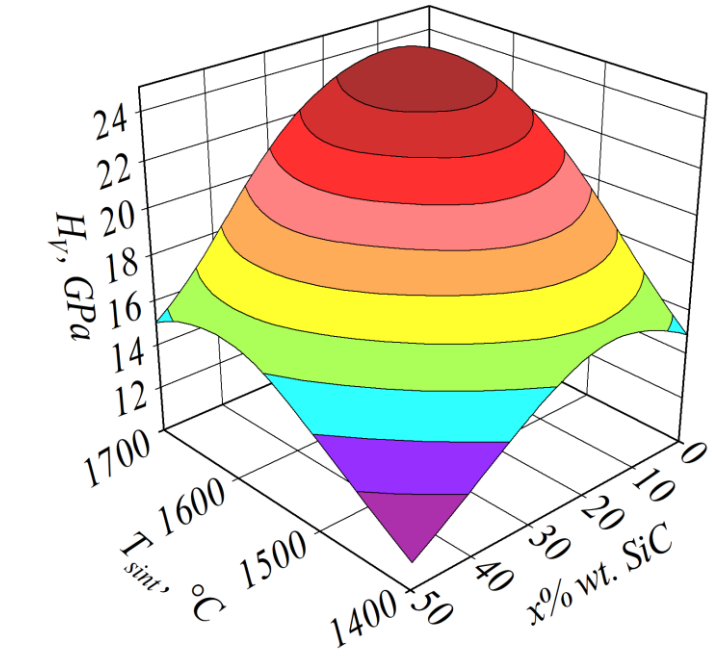

a

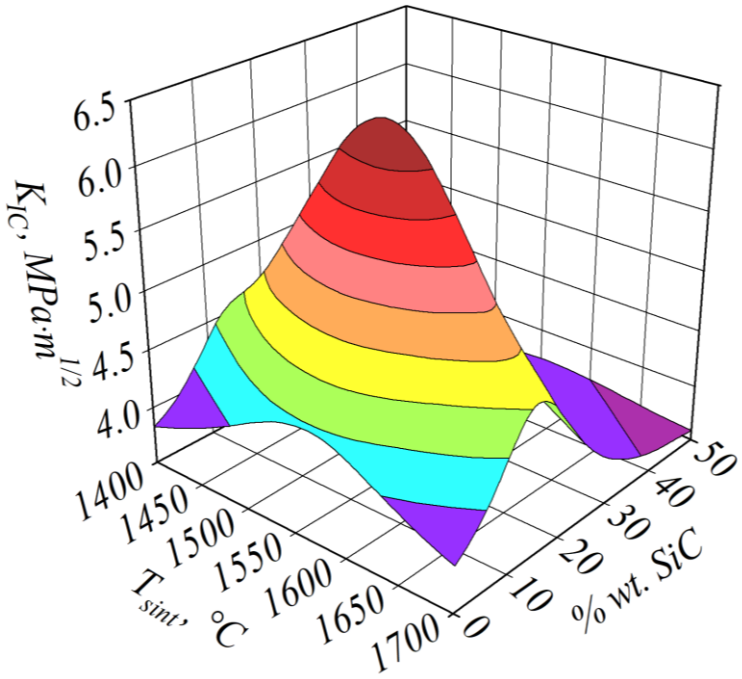

b

Figure 3.20 – Dependency of the micro-hardness H_V (*a*) and the stress intensity coefficient K_{IC} (*b*) on the sintering temperature T_{sint} and SiC content in the Al_2O_3–SiC system

The inclination of planes can be used for estimation of the impact of each primary parameter on the factor-response – H_V and K_{IC}.

REFERENCES

1. Moriarty, P. (2001). Nanostructured materials. *Reports on Progress in Physics*, 64, 3, 297–381.

2. Gusev, A. I., Rempel, A. A. (2001). Nanokristallicheskie materialy. Moskva: Fizmatlit, 224.

3. Leinonen, A., Kivisaari, S. (2005). NanoDictionary. *Nanotechnology Perceptions*, 1, 147–160.

4. Gleiter, H. (1992). Materials with ultrafine microstructures: Retrospectives and perspectives. *Nanostructured Materials*, 1, 1, 1–19.

5. Jeevanandam, J., Barhoum, A., Chan, Y. S., Dufresne, A., Danquah, M. K. (2018). Review on nanoparticles and nanostructured materials: history, sources, toxicity and regulations. *Beilstein Journal of Nanotechnology*, 9, 1050–1074. DOI: 10.3762/bjnano.9.98.

6. Gleiter, H. (2000). Nanostructured materials: basic concepts and microstructure. *Acta Materialia*, 48, 1–29.

7. Valiev, R. Z., Islamgaliev, R. K., Alexandrov, I. V. (2000). Bulk nanostructured materials from severe plastic deformation. *Progress in Materials Science*, 45, 103–189.

8. Lyakishev, N. P. (2003). Nanokristallicheskie struktury – novoe napravlenie razvitiya konstruktsionnykh materialov. *Vestnik RAN*, 73, 5, 422–428.

9. Gevorkyan, E. S., Semchenko, G. D., Timofeeva, L. A., Nerubatskyi, V. P. (2015). New materials and technologies for their production: textbook. Kharkiv: “Disa plyus”, 344.

10. Skorokhod, V. V., Ragulya, A. V. (2003). Nanostrukturnaya keramika i nanokompozity: dostizheniya i perspektivy. *Progressivnye materialy i tekhnologii*, 2, 7–34.

11. Gevorkyan, E. S., Nerubatskyi, V. P. (2009). The question of obtaining finely dispersed structures from aluminum oxide nanopowders. *Collected scientific works of Ukrainian State Academy of Railway Transport*, 111, 151–167.

12. Gevorkyan, E. S., Nerubatskyi, V. P., Gutsalenko, Yu. H., Morozova, O. M. (2020). Some features of ceramic foam filters energy efficient technologies development. *Modern engineering and innovative technologies*, 14, 1, 46–60. DOI: 10.30890/2567-5273.2020-14-01-014.

13. Firstov, S. A. (2003). Osobennosti deformatsii i razrusheniya nanokristallicheskikh materialov. Progressivnye materialy i tekhnologii: U 2-kh t. Kiev: Akademperiodika, 2, 663.

14. Andrievkii, R. A., Glezer, A. M. (1999). Razmernye effekty v nanokristallicheskikh materialakh. I. Osobennosti struktury. Termodinamika. Fazovye ravnovesiya. Kineticheskie yavleniya. *Fizika metallov i metallovedenie*, 88, 1, 50–73.

15. Buffat, Ph., Borel, J.-P. (1976). Size effect on the melting temperature of gold particles. *Phys. Rev.*, 13, 2287–2298.

16. Carlton, C. E., Ferreira, P. J. (2007). What is behind the inverse Hall-Petch effect in nanocrystalline materials? *Acta Materialia*, 55, 3749–3756.

17. Andrievskii, R. A. (1994). Poluchenie i svoistva nanokristallicheskikh tugoplavkikh soedinenii. *Uspekhi khimii*, 63, 5, 431–448.

18. Gusev, A. I. (1998). Nanokristallicheskie materialy – metody polucheniya i svoistva. Ekaterinburg: UrO RAM, 200.

19. Sukhovich, K. P., Ungurs, I. A. (1983). Metody izgotovleniya ul'tradispersnykh poroshkov metallov. *Izv. AN Latv. SSR*, 4 (429), 63–77.

20. Libenson, G. A., Lopatin, V. Yu., Komarnitskii, G. V. (2002). Formovanie i spekanie. T. 2. Moskva: MISIS, 320.

21. Gevorkyan, E., Nerubatskyi, V., Chyshkala, V., Morozova, O. (2021). Revealing specific features of structure formation in composites based on nanopowders of synthesized zirconium dioxide. *Eastern-European Journal of Enterprise Technologies*, 5, 12 (113), 6–19. DOI: 10.15587/1729-4061.2021.242503.

22. Khasanov, O. L., Sokolov, V. M., Dvilis, E. S., Pokholkov, Yu. P. (2002). Ul'trazvukrvaya tekhnologiya izgotovleniya konstruktsionnoi i funktsional'noi nanokeramiki. *Perspektivnye materialy*, 1, 76–83.

23. Gevorkyan, E. S., Timofeeva, L. A., Nerubatskyi, V. P., Melnyk, O. M. (2016). Integrated technologies of materials processing: textbook. Kharkiv: Ukrainian State University of Railway Transport, 238.

24. Chyshkala, V. O., Lytovchenko, S. V., Gevorkyan, E. S., Nerubatskyi, V. P., Mazilin, B. O. (2021). Research of features of consolidation of anti-friction materials based on powder mixture Cu–Pb–C. *Collected scientific works of Ukrainian State University of Railway Transport*, 198, 7–21. DOI: 10.18664/1994-7852.198.2021.256456.

25. Lyakishev, N. P., Alymov, M. I. (2006). Nanomaterialy konstruktsionnogo naznacheniya. *Rossiiskie nanotekhnologii*, 1, 71–81.

26. Chyshkala, V. O., Lytovchenko, S. V., Gevorkyan, E. S., Nerubatskyi, V. P., Morozova, O. M. (2021). Mastering the processes of synthesis of oxide compounds with the use of a powerful source of fast heating of the initial ingredients. *Collected scientific works of Ukrainian State University of Railway Transport*, 196, 118–128. DOI: 10.18664/1994-7852.196.2021.242226.

27. Kear, B. H., Colaizzi, J., Mayo, W. E., Liao, S.-C. (2001). On the processing of nanocrystalline and nanocomposite ceramics. *Scripta Materialia*, 44, 8/9, 2065–2068.

28. Ivzhenko, V. V. (2011). Inzhektsionnoe formovanie izdelii iz nanodispersnykh poroshkov tugoplavkikh soedinenii. *Nanosystems, Nanomaterials, Nanotechnologies,* 9, 3, 651–660.

29. Mukhopadhyay, A., Basu, B. (2007). Consolidation–microstructure–property relationships in bulk nanoceramics and ceramic nanocomposites: a review. *International Materials Reviews*, 52, 5, 257–288.

30. Geguzin, Ya. E. (1984). Fizika spekaniya. 2-e izd., pererab. i dop. Moskva: Nauka, 312.

31. Skorokhod, V. V., Solonin, S. M. (1984). Fiziko-metallurgicheskie osnovy spekaniya poroshkov. Moskva: Metallurgiya, 159.

32. Gevorkyan, E. S., Rucki, M., Nerubatskyi, V. P., Żurowski, W., Siemiątkowski, Z., Morozow, D., Kharatyan, A. G. (2022). Remanufacturing and advanced machining processes for new materials and components. Taylor & Francis, 204. DOI: 10.1201/9781003218654.

33. Gusev, A. I. (2005). Nanomaterialy, nanostruktury, nanotekhnologii. Moskva: Fizmatlit, 416.

34. Andrievskii, R. A. (1991). Poroshkovoe materialovedenie. Moskva: Metallurgiya, 205.

35. Skorokhod, V. V., Uvarova, I. V., Ragulya, A. V. (2001). Fiziko-khimichna kinetika v nanostrukturnikh sistemakh. Kyiv: Akadem-periodika, 180.

36. Groza, J. R. (1999). Powder consolidation. Non-equilibrium processing of materials [Ed. by C. Suryanarayana]. *Pergamon Press*, 345–372.

37. Andrievskii, R. A. (2005). Nanomaterialy na osnove tugoplavkikh karbidov, nitridov i boridov. *Uspekhi khimii,* 12, 1163–1175.

38. Shatt, V. (1983). Poroshkovaya metallurgiya. Spechennye i kompozitsionnye materialy. Moskva: Metallurgiya, 520.

39. Grosa, J. R. (1999). Sintering of nanocristalline powders. *International Journal of Powder Metallurgy*, 35, 7, 59–66.

40. Popil'skii, R. Ya., Pivinskii, Yu. E. (1983). Pressovanie poroshkovykh keramicheskikh mass. Moskva: Metallurgiya, 176.

41. Yanagida, Kh. (1986). Tonkaya tekhnicheskaya keramika. Moskva: Metallurgiya, 279.

42. Bhaduri, S., Bhaduri, S. B. (1998). Recent developments in ceramic nanocomposites. *Journal of Metals*, 50, 1, 44–51.

43. Shevchenko, A. V., Ruban, F. K., Dudnik, E. V. (2000). Vysokotekhnologichnaya keramika na osnove dioksida tsirkoniya. *Ogneupory i tekhnicheskaya keramika*, 9, 2–8.

44. Gevorkyan, E. S., Nerubatskyi, V. P. (2009). Modeling of the AL_2O_3 hot pressing process with direct transmission of an alternating electric current with a frequency of 50 Hz. *Collected scientific works of Ukrainian State Academy of Railway Transport*, 110, 45–52.

45. Raichenko, A. I. (1987). Osnovy protsessa spekaniya poroshkov propuskaniem elektricheskogo toka. Moskva: Metallurgiya, 128.

46. Raichenko, A. I., Istomina, T. I., Troyan, I. A. (2000). Spekanie poroshkov pri nalozhenii elektricheskogo toka i periodicheskikh mekhanicheskikh impul'sov. *Poroshkovaya metallurgiya*, 3–4, 105–109.

47. Anderson, K. R. (1999). Influence electric field on SiC properties during hot pressing. *Mater. Sci. Eng.*, 270, 105–114.

48. Groza, J. R. (1998). Field assisted sintering. *Powder Metallurgy*, 7, 2, 583–589.

49. Tokita, M. (2004). Mechanism of spark plasma sintering. *J. Material Science*, 5, 45, 78–82.

50. Berhard, F., Le gallet, S., Spinassou, N., Paris, S., Gaffet, E., Wilde, J., Munir, Z. (2004). Dense nanostructured materials obtained by spark plasma sintering and field activated pressure assisted synthesis starting from mechanically activated powder mixtures. *Science of Sintering*, 36, 155–164. DOI: 10.2298/SOS0403155B.

51. Harmer, M., Roberts, W. (1979). Rapid sintering of pure and doped alpha–Al_2O_3. *Trans. J. Brit. Ceram. Soc.*, 78, 22–25.

52. Jhonson, D. L. (1989). Ultra-rapid sintering of ceramics. Science of sintering. New directions for material's processing and microstructural control. *Pergamon Press*, 497–506.

53. McCandlish, L. E., Kear, B. H., Kim, B. K. (1992). Sintering WC nanopowders. *Nanostructure Materials*, 1, 119–121.

54. Skorokhod, V. V., Ragulya, A. V. (1994). Spekanie s kontroliruemoi skorost'yu kak metod upravleniya mikrostrukturoi keramiki i podobnykh spechennykh materialov. *Poroshkovaya metallurgiya*, 3–4, 3–10.

55. Bourell, D. L., Groza, J. R. (1998). Consolidation of ultrafine and nanocrystalline powders. *Powder Metallurgy*, 7, 504–515.

56. Dadon, D., Martin, L., Rosen, M. (1996). Electric pulse assisted rapid consolidation of ultrafine grained alumina matrix composites. *Journal of Materials Synthesis and Processing*, 4, 32, 95–103.

57. Hwan-Cheol, K., In-Jin, S., Jin-Kook, Y. (2007). Consolidation of ultrafine WC and WC-Co hard materials by pulsed current actived and its mechanical properties. *International Journal of Refractory Metals and Hard Materials*, 25, 1, 46–52.

58. Mishra, R. S., Mukherjee, A. K. (2000). Electric pulse assisted rapid consolidation of ultrafine grained alumina matrix composites. *Mat. Sci. Eng.*, 28, 178–182.

59. Gevorkyan, E., Rucki, M., Krzysiak, Z., Chishkala, V., Zurowski, W., Kucharczyk, W., Barsamyan, V., Nerubatskyi, V., Mazur, T., Morozow, D., Siemiątkowski, Z., Caban, J. (2021). Analysis of the electroconsolidation process of fine-dispersed structures out of hot pressed Al_2O_3–WC nanopowders. *Materials*, 14, 21, 6503. DOI: 10.3390/ma14216503.

60. Gevorkyan, E. S., Nerubatskyi, V. P., Chyshkala, V. O., Morozova, O. M. (2020). Aluminum oxide nanopowders sintering at hot pressing using direct current. *Modern scientific researches*, 14, 1, 12–18. DOI: 10.30889/2523-4692.2020-14-01-002.

61. Gevorkyan, E. S., Gutsalenko, Yu. G. (2008). Some regularities of hot pressing of tungsten monocarbide nanopowders. *Bulletin of NTU "KhPI": Technologies in mechanical engineering*, 35, 44–48.

62. Gevorkyan, E., Nerubatskyi, V., Gutsalenko, Yu., Melnik, O., Voloshyna, L. (2020). Examination of patterns in obtaining porous structures from submicron aluminum oxide powder and its mixtures. *Eastern-European Journal of Enterprise Technologies*, 6, 6 (108), 41–49. DOI: 10.15587/1729-4061.2020.216733.

63. Namitokov, K. K. (1978). Elektroerozionnye yavleniya. Moskva: Energiya, 456.

64. Bakshin, V. K., Kuz'min, G. P., Minaev, I. M., Rukhadze, A. A., Timofeev, N. B. (2005). Osobennosti skol'zyashchego razryada po granitse razdela dielektrikov s razlichnoi dielektricheskoi pronitsaemost'yu. *Prikladnaya Fizika*, 6, 54–59.

65. Guicciardi, S. (1999). Composition dependence of mechanical and wear properties of electroconductive ceramics. *Powder metallurgy*, 3–4, 32–41.

66. Anderson, K. R., Groza, J. R. (1990). Surface oxide debonding in field assisted powder sintering. *Mater. Sci. Engin.*, 27, 278–282.

67. Gevorkyan, E., Mamalis, A., Vovk, R., Semiatkowski, Z., Morozow, D., Nerubatskyi, V., Morozova, O. (2021). Special features of manufacturing cutting inserts from nanocomposite material Al_2O_3-SiC. *Journal of Instrumentation*, 16, 10, P10015. DOI: 10.1088/1748-0221/16/10/P10015.

68. Gevorkyan, E. S., Nerubatskyi, V. P., Chyshkala, V. O., Morozova, O. M. (2021). Cutting composite material based on nanopowders of aluminum oxide and tungsten monocarbide. *Modern engineering and innovative technologies*, 15, 2, 6–14. DOI: 10.30890/2567-5273.2021-15-02-020.

69. Gevorkyan, E., Rucki, M., Sałaciński, T., Siemiątkowski, Z., Nerubatskyi, V., Kucharczyk, W., Chrzanowski, Ja., Gutsalenko, Yu., Nejman, M. (2021). Feasibility of cobalt-free nanostructured WC cutting inserts for machining of a TiC/Fe composite. *Materials*, 14, 12, 3432. DOI: 10.3390/ma14123432.

70. Hennicke, J., Keesel, H. U. (2004). Field assisted sintering technology ("FAST") for the consolidation of innovative materials. *Ceram Forum Int.*, 81, 14–16.

71. Keramicheskie materialy (1991). Pod red. G. N. Maslennikovoi. Moskva: Stroiizdat, 320.

72. Averback, R. S., Hahn, H., Höfler, H. J. (1989). Interfaces between polymers, metals and ceramics. *Mater. Res. Soc. Symp. Proc.*, 153.

73. Zaionts, R. M., Kordonskaya, R. K. (1966). Keramicheskie khimicheski stoikie izdeliya. Moskva: Stroiizdat, 188.

74. Narayan, R. (2009). Biomedical materials. *Springer*, 550.

75. Bhat, S. V. (2005). Biomaterials. *Alpha Science Intl Ltd*, 279.

76. Barsoum, M. W. (2003). Fundamentals of ceramics. *Institute of Physics, Bristol*, 388.

77. Kuzin, V. V. (2004). Rabotosposobnost' rezhushchikh instrumentov iz nitridnoi keramiki pri obrabotke chugunov. *Vestnik mashinostroeniya*, 5, 39–43.

78. Panov, V. S. (2007). Sovremennaya instrumental'naya keramika. Sostavy i oblasti primeneniya. *Instrumental'nyi mir*, 1 (33), 30–33.

79. Choi, Y., Rhee, S.-W. (1995). Reaction of TiO_2-Al-C in the combustion synthesis of TiC-Al_2O_3 composite. *J. Amer. Ceram. Soc.*, 78, 4, 986–992.

80. Gevorkyan, E., Nerubatskyi, V., Chyshkala, V., Gutsalenko, Y., Morozova, O. (2021). Determining the influence of ultra-dispersed aluminum nitride impurities on the structure and physical-mechanical properties of tool ceramics. *Eastern-European Journal of Enterprise Technologies*, 6, 12 (114), 40–52. DOI: 10.15587/1729-4061.2021.245938.

81. Vasin, S. A., Vereshchaka, A. S., Kushner, V. S. (2001). Rezanie materialov. Termomekhanicheskii podkhod k sisteme vzaimosvyazei pri rezanii. Moskva: Izdatel'stvo MGTU imeni N. E. Baumana, 448.

82. Senthil Kumar, A., Raja Durai, A., Sornakumar, T. (2006). Wear behaviour of alumina based ceramic cutting tools on machining steels. *Tribology International*, 39, 3, 191–197. DOI: 10.1016/j.triboint.2005.01.021.

83. Zhang, X., Zhang, Z., Wang, W., Shan, J., Che, H., Mu, J., Wang, G. (2017). Microstructure and mechanical properties of B_4C–TiB_2–SiC composites toughened by composite structural toughening phases. *Journal of the American Ceramic Society*, 100 (7), 3099–3107. DOI: 10.1111/jace.14815.

84. Boudebane, S. (2002). Influence des additions sur la synthese par combustion auto – propagee de la ceramique TiC–Al_2O_3. The influence of additions on the self propagating high-temperature synthesis of TiC–Al_2O_3 ceramics. *Annales de Chimie Science Des Matériaux,* 27(2), 1–15. DOI: 10.1016/s0151-9107(02)80027-7.

85. Dudzinski, D., Devillez, A., Moufki, A., Larrouquère, D., Zerrouki, V., Vigneau, J. (2004). A review of developments towards dry and high speed machining of Inconel 718 alloy. *International Journal of Machine Tools and Manufacture,* 44 (4), 439–456. DOI: 10.1016/s0890-6955(03)00159-7.

86. Aslan, E., Camuşcu, N., Birgören, B. (2007). Design optimization of cutting parameters when turning hardened AISI 4140 steel (63 HRC) with Al_2O_3+TiCN mixed ceramic tool. *Materials & Design,* 28 (5), 1618–1622. DOI: 10.1016/j.matdes.2006.02.006.

87. Coelho, R. T., Silva, L. R., Braghini, A., Bezerra, A. A. (2004). Some effects of cutting edge preparation and geometric modifications when turning INCONEL 718™ at high cutting speeds. *Journal of Materials Processing Technology*, 148 (1), 147–153. DOI: 10.1016/j.jmatprotec.2004.02.001.

88. Grigor'ev, S. N., Volosova, M. A., Borovskii, V. G. (2005). Tekhnologicheskoe obespechenie kachestva poverkhnostnogo sloya keramicheskogo instrumenta dlya povysheniya ego rabotosposobnosti pri obrabotke zakalennykh stalei. *Stanki i instrument,* 9, 14–19.

89. Zhed', V. P., Borovskii, G. V., Muzykant, A. Ya., Ippolitov, G. M. (1987). Rezhushchie instrumenty, osnashchennye sverkhtverdymi i keramicheskimi materialami, i ikh primenenie: Spravochnik. Moskva: Mashinostroenie, 320.

90. Frantsevich, I. N., Gnesin, G. G., Kurdyumov, A. V. (1980). Sverkhtverdye materialy. Kiev: Naukova dumka, 296.

91. Vovk, R. V., Gevorkyan, E. S., Nerubatskyi, V. P., Prokopiv, M. M., Chyshkala, V. O., Melnyk, O. M. (2018). New ceramic composite materials for instrumental purposes: monograph. Kharkiv: V. N. Karazin Kharkiv National University, 200.

92. Kashcheev, I. D. (2004). Svoistva i primenenie ogneuporov. Spravochnoe izdanie. Moskva: Teplotekhnik, 352.

93. Zeng, J. (1992). High-temperature strength and cavitation threshold of silicon nitride-silica ceramics. *J. Am. Ceram. Soc.*, 75, 195.

94. Chyshkala, V. O., Lytovchenko, S. V., Gevorkyan, E. S., Nerubatskyi, V. P., Morozova, O. M. (2021). Structural phase processes in multicomponent metal ceramic oxide materials based on the system Y–Ti–Zr–O (Y_2O_3–TiO_2–ZrO_2). *SWorldJournal,* 7, 1, 17–32. DOI: 10.30888/2663-5712.2021-07-01-008.

95. Wu, W. H., Li, Y. X., Bai, P. K., Wu, W. P. (2016). Research progress of Ti (C, N)-based cermets composite. *Hot Working Technology,* 45, 12–14.

96. Gao, M. Z., Xiao, S. R., Deng, X. C. (2008). New ceramic tool of research and application. *Coal Mine Machinery,* 29, 83–85.

97. Xia, C. Y. (2006). Ceramic material and application of high-speed machine. *Coal Technology,* 25, 8–10.

98. Tang S.-W., Liu D.-S., Li P.-N., Tang, W.-B., Tang, D. (2014). Preparation and cutting performance of Ti CN-based functionally gradient cermets. *Journal of Functional Materials,* 45 (13), 13126–13130. DOI: 10.3969/j.issn.1001-9731.2014.13.027.

99. El-Wazery, M. S., El-Desouky, A. R. (2015). A review on functionally graded ceramic-metal materials. *Journal of Materials and Environmental Science,* 6, 5, 1369–1376.

100. Garshin, A. P., Gropyanov, V. M., Zaitsev, G. P., Semenov, S. S. (2003). Keramika dlya mashinostroeniya. Moskva: Nauchtekhlitizdat, 384.

101. Boldin, M. S., Sakharov, N. V., Shotin, S. V. (2012). Kompozitsionnye keramiki na osnove oksida alyuminiya, poluchennye metodom elektroimpul'snogo plazmennogo spekaniya dlya tribologicheskikh primenenii. *Vestnik NU imeni N. I. Lobachevskogo*, 6 (1), 32–37.

102. Baranov, G. A., Kryukovskii, V. I., Maronchuk, I. I. (2013). Poluchenie nanoporoshkov titana iz titanovoi gubki i otkhodov titanovoi promyshlennosti s primeneniem metoda bakterial'nogo vyshchelachivaniya. *Visnik NTUU "KPI", Seriya mashinobuduvannya*, 3 (69), 131–135.

103. Trent, E. M. (1980). Rezanie metallov. Moskva: Mashinostroenie, 263.

104. Granovskii, G. I., Granovskii, V. G. (1985). Rezanie metallov. Moskva: Vysshaya shkola, 304.

105. Panov, A. A., Anikin, V. V., Boim, N. G. (2004). Obrabotka metallov rezaniem: Spravochnik tekhnologa. Moskva: Mashinostroenie, 784.

106. Poletika, M. F. (2001). Teoriya rezaniya. Mekhanika protsessa rezaniya. Chast' 1. Tomsk: Izdatel'stvo TPU, 202.

107. Vasin, S. A., Vereshchaka, A. S., Kushner, B. C. (2001). Rezanie materialov: Termomekhanicheskii podkhod k sisteme vzaimosvyazei pri rezanii. Moskva: Izdatel'stvovo MGTU imeni N. E. Baumana, 448.

108. Baranovskii, Yu. V., Brakhman, L. A., Gdalevich, A. I. (1995). Rezhimy rezaniya metallov: Spravochnik. Moskva: NIITavtoprom, 456.

109. Rahaman, M. N. (2007). Sintering of ceramics. *CRC Press,* 388.

110. Rahaman, M. N. (2003). Ceramic processing and sintering. New York: Handcover, 875.

111. Senos, A. M. R., Vieira, J. M. (1993). Pore size distribution and particle rearrangement during sintering. *EuroCeramics,* San Lorenzo: FaenzaEditrice Iberica, 821–826.

112. Jamin, C. C. (2014). Constrained sintering of patterned ceramic films on stiff substrates. Darmstadt: Technischen Universität Darmstadt, 156.

113. German, R. M. (1996). Sintering theory and practice. 1st ed. New York: Willey, 568.

114. Coble, R. L. (1973). Effects of particle-size distribution in initial-stage. *Am Ceram Soc.,* 56, 461–466.

115. Willardson, R. K., Park, Y.-S., Weber, E. R. (1998). SiC materials and devices. *Academic Press,* 420.

116. De Keyser, W. L. (1951). Contribution to the study of sillimanite and mullite by X-rays. *Trans. Brit. Ceram. Soc.,* 50, 349–364.

117. Jerebtsov, D. A., Mikhailov, G. G., Sverdina, S. V. (2000). Phase diagram of the system: Al_2O_3-ZrO_2. *Ceramics International,* 26, 8, 821–823.

118. Ripan, R., Chetyan, I. (1972). Neorganicheskaya khimiya. Khimiya metallov. T. 2. Moskva: Mir, 871.

119. Earnshaw, A., Greenwood, N. (1997). Chemistry of the Elements. *Butterworth-Heinemann,* 297.

120. Griffith, A. A. (1920). The phenomena of rupture and flow in solids. *Phil. Trans. R. Soc. London A,* 221, 163–198.

121. Evans, A. G. (1978). Microfracture from thermal expansion anisotropy. I Single phase systems. *Acta Metall.,* 26, 1845–1853.

122. Sheludyak, Yu. E., Kashporov, L. Ya. (1992). Teplofizicheskie svoistva komponentov goryuchikh sistem. Moskva: NPO Inform TEI, 184.

123. Chirkin, V. S. (1967). Teplofizicheskie svoistva materialov yadernoi tekhniki. Moskva: Atomizdat, 474.

124. Gevorkyan, E. S., Rucki, M., Kagramanyan, A. A., Nerubatskiy, V. P. (2019). Composite material for instrumental applications based on micro powder Al_2O_3

with additives nano-powder SiC. *International Journal of Refractory Metals and Hard Materials*, 82, 336–339. DOI: 10.1016/j.ijrmhm.2019.05.010.

125. Swanson, P. L., Fairbanks, C. J., Lawn, B. R., Yiu, W. M., Hockey, B. J. (1987). Crack-interface grain bridging as a fracture resistance mechanism in ceramics. I: Experimental study on alumina. *J. Am. Ceram. Soc.*, 70, 279–289.

126. Spiridonov, A. A. (1981). Planirovanie eksperimenta pri issledovanii tekhnologicheskikh protsessov. Moskva: Mashinostroenie, 184.

127. Sinogeikin, S. V., Lakshtanov, D. L., Nicholas, J. D., Bass, J. D. (2004). Sound velocity measurements on laser-heated MgO and Al_2O_3. *Physics of the Earth and Planetary Interiors*, 143–144, 575–586.

128. Berman, R. (1979). Thermal Conduction in solids. Moscow: Mir, 286.

129. Oskotskii, V. S., Smirnov, I. A. (1972). Defekty v kristallakh i teploprovodnost'. Leningrad: Nauka, 60.

130. Chyshkala, V. O., Lytovchenko, S. V., Gevorkyan, E. S., Nerubatskyi, V. P., Mazilin, B. O., Morozova, O. M. (2021). Mastering and modernization of physico-chemical processes of synthesis of oxide compounds with structure of pyrochlorine. *Collected scientific works of Ukrainian State University of Railway Transport*, 197, 82–98. DOI: 10.18664/1994-7852.197.2021.248097.

131. Katsev, P. G. (1974). Statisticheskie metody issledovaniya rezhushchego instrumenta. Izdanie 2-e, pererab. i dop. Moskva: Mashinostroenie, 231.

132. Archer, D. G. (1993). Thermodynamic properties of synthetic sapphire (α-Al_2O_3), standard reference material 720 and the effect of temperature-scale differences on thermodynamic properties. *J. Phis. Chem. Ref. Data*, 22, 1441–1453.

133. Zolotorevskii, V. S. (1998). Mekhanicheskie svoistva metallov. Moskva: MISIS, 400.

134. Okhotin, A. S., Borovikova, R. P., Nechaeva, T. V., Pushkarskii, A. S. (1984). Teploprovodnost' tverdykh tel: Spravochnik. Moskva: Energoatomizdat, 321.

135. Zhed,' V. P., Borovskii, G. V., Muzykant, A. Ya., Ippolitov, G. M. (1987). Rezhushchie instrumenty, osnashchennye sverkhtverdymi i keramicheskimi materialami, i ikh primenenie: Spravochnik. Moskva: Mashinostroenie, 320.

136. Isachenko, V. P., Osipova, V. A., Sukomel, A. S. (1975). Teploperedacha. Moskva: Energiya, 483.

137. Wigley, D. (1971). Mechanical properties of materials at low temperatures. *Springer US*, 326.

138. Prutki i polosy iz bystrorezhushchei stali: GOST 19265-73. (1975). Moskva: Izdatel'stvo standartov, 22.

139. Materialy keramicheskie instrumental'nye. Marki: GOST 26630-85. (1985). Moskva: Izdatel'stvo standartov, 4.

140. NTK Cutting tools. (2014). *Cutting tools general catalog*, 4, 533.

141. Muranaka, T., Kikuchi, Y., Yoshizawa, T., Shirakawa, N., Akimitsu, J. (2008). Superconductivity in carrier-doped silicon carbide. *Science and Technology of Advanced Materials*, 9 (4), 044204. DOI: 10.1088/1468-6996/9/4/044204.

142. Andrievsky, R. A., Glezer, A. M. (2000). Dimensional effects in nanocrystalline materials. Mechanical and physical properties. *Fizika metallov i metallovedenie*, 89, 1, 91–112.

143. Ermer, E., Ptak, W., Stobierski, L. (2001). Influence of sintering activators on structure of silicon carbide. *Solid State Ionics*, 141–142, 523–528.

144. Vil'son, A. L. (1987). Vybor instrumenta i rezhima rezaniya, obespechivayushchikh minimal'nye vibratsii pri obrabotke. *Stanki i instrument*, 4, 28–30.

145. Kabaldin, Yu. G. (1986). Strukturno-energeticheskii podkhod k iznashivaniyu tverdykh splavov. *Izvestiya vysshikh uchebnykh zavedenii*, 4, 127–131.

146. Trefilov, V. I., Moiseev, V. F. (1976). Dispersnye chastitsy v tugoplavkikh metallakh. Kiev: Naukova dumka, 239.

Scientific publication

GEVORKYAN Edwin Spartakovych
NERUBATSKYI Volodymyr Pavlovych
KISLITSA Maksym Valeriiovych

COMPOSITE MATERIALS BASED ON ALUMINA AND SILICON CARBIDE

Monograph

Responsible for release Nerubatskyi V. P.

Author's edition

Sent to the printer 07.02.2022. Format 60×84/16.
Type Times New Roman. Offset paper.
Printer’s sheet 6.72. 50 printed copies. Order № 121322. Agreed price.

Publisher LLC “VOSKHOD-PRINT”
61057, Kharkiv, Rymars′ka str., 3/5

Manufacturer Individual person-entrepreneur Machulin L. I.
61057, Kharkiv, Rymars′ka str., 3/5
Certificate ХК № 125 of 24.11.2004